Lattice Dynamics in materials for energy applications

David James Voneshen

Royal Holloway College
University of London

A dissertation submitted to the University of London
for the degree of Doctor of Philosophy

June 2015

Declaration of Authorship

I David James Voneshen hereby declare that this thesis and the work presented in it is entirely my own. Where I have consulted the work of others, this is always clearly stated.

Signed: _____

Date: _____

Abstract

Lattice dynamics are of the utmost importance in understanding many modern materials. They enable us to probe the specific details of a material's chemistry and its ordering, and are vital to understanding many technologically relevant phenomena. Unfortunately for anything more than the simplest system understanding how the dynamics relate back to the properties becomes extremely challenging.

This difficulty can be overcome by combining the latest experimental techniques at international x-ray and neutron scattering facilities with first-principles calculations. The experiments allow us to validate the calculations and the calculations can then be related back to an understanding of the material's properties.

In this thesis two different problems are investigated. The first is a study of the vibrational spectrum of a thermoelectric material Na_xCoO_2. This system has cage-like structures with atoms inside the cage that can rattle. In similar materials this rattling has been postulated to suppress the thermal conductivity by phonon scattering. We find that in fact there is no significant phonon scattering and instead the suppression is due to a reduction in the phonon velocities. The effect of changing the cage-like structures and doping the rattling ion is also investigated.

The second system studied is the alkaline doped iron selenide superconductors. Spectroscopic studies have shown that these exhibit a symmetry breaking phase transition on cooling but its origin is unknown. We show that this arises from a subtle ferrimagnetic transition related to the localisation of charge on certain iron sites. It is this charge localisation which is responsible for the symmetry breaking and by relating these results to the literature the case is put forward that the ferrimagnetism is also related to the origin of superconductivity in this system.

Acknowledgements

I wish to thank my supervisor Professor J.P. Goff for his support and guidance during the PhD. It has been a pleasure discussing both work and football with you boss. I would also like to thank Professor K. Refson for his significant contribution to this thesis and my development. Both Jon and Keith have my particular gratitude for supporting my wish to get involved in DFT calculations despite it not being originally envisaged.

I am indebted to the many instrument scientists I have been privileged to work with. At the ESRF, E. Borissenko, T. Forrest, M. Krisch and A. Bossak. At the ILL, M. Enderle and A. Piovano. At ISIS, J.R. Stewart, R. Bewley, E.A. Goremychkin, M.J. Gutmann and H. Walker.

Dan, thank you for your help with the x-ray machine, RMC, PPMS, neutrons, synchrotron x-rays and tea time. Uthay, thank you for the beautiful samples, cricket discussions and being an all-round excellent officemate. Also, thanks both for occasionally letting me win at badminton.

Thank you to the other PhDs within the group, Manoj, Toby, Eron and Dave it has been a pleasure working with you and I hope my explanations haven't set you back too many months! My many many officemates (I'm not listing you, someone will get forgotten, YOU are included) thank you for putting up with me and being lovely company.

Jim and Connor the video ref, thanks both for teaching me how to be a successful

PhD student as well as being great company. The physics (and guest) footballers, RHUL staff football team, RHUL staff cricket team, Hetairoi CC, RHUL staff and student badminton clubs and the people who have thrashed me at squash, thanks everyone for keeping me healthy and sane! Thanks to my board gamers, pc gamers and James for qualifying in every category apart from cricket but still not managing to be specifically named so far. Further thanks to everyone I have lived with who have had to put up with me at my grumpiest. Regular and irregular 3pm tea time attenders (special thanks to Dan and Chris for creating this vital ~~15 mins~~, ~~30 mins~~, oh who am I kidding, hour) thanks for listening to me discuss neutrons.

Finally, I should like to acknowledge the tremendous contribution that my parents have made. Thanks for being there when everything was really horrible as well as really great, bankrolling me, and proofreading this thesis despite it being entirely in "science"!

Contents

List of Figures

List of Tables

Chapter 1

Introduction

Modern civilisation requires vast amounts of energy. A great deal of this energy however, is wasted. For example, the transmission of electric power within the UK results in losses of around 8% [7] while 1/6 of the energy used by UK industry is potentially recoverable[8]. These represent considerable contributions to individual bills, company overheads as well as contributing to CO_2 emissions.

There is unlikely to be a single killer material which can solve all of these problems, instead many different materials with properties tailor made to their specific application will be used. Superconductors could be used in power lines to reduce transmission losses but the superconducting transition temperature is still very much within the cryogenic region preventing large scale deployment. Other materials, known as thermoelectrics, are capable of turning waste heat back into useful power, but their efficiency is low and production costs high, and this has limited them to very specific applications.

The dynamics of materials are vital to building up a comprehensive understanding of their physical properties. In the case of thermoelectrics the lattice dynamics are of direct technological relevance as the lattice thermal conductivity limits device efficiency. In the case of superconductors, while some are phonon mediated most

high temperature superconductors are not, but the lattice dynamics place very tight constraints upon the underlying state which must be known before a proper theory of unconventional superconductivity can be developed.

1.1 Thermoelectrics

There are now a vast range of thermoelectric materials [9] but all of them share a common design aim. A large voltage for a given temperature gradient is required while keeping the electrical conductivity high (as it must go into an electric circuit) and the thermal conductivity low (so that a large temperature gradient can be used). This presents a real design challenge.

1.1.1 The figure of merit

With the proliferation of different thermoelectric materials it becomes necessary to have a single figure of merit by which they can be compared. This is stated as

$$zT = S^2 T \frac{\sigma}{\kappa}.$$

S is the Seebeck co-efficient (or voltage for a given temperature gradient), σ the resistivity and κ the thermal conductivity. The additional T term arises from the fact that at higher temperatures a greater electrostatic repulsion can be overcome allowing larger voltages to be obtained. The best thermoelectrics now have a $zT > 2$ [10].

These parameters are all interdependent. Within the parabolic band, energy-independent scattering approximation [11]

$$S = \frac{8\pi^2 k_B^2}{3eh^2} m^* T \left(\frac{\pi}{3n}\right)^{2/3},$$

where m^* is the effective mass of the carrier (either electrons or holes) and n the carrier concentration. This shows that in general S will improve as the system's metallic properties decrease, this will of course also reduce the electrical conductivity (σ). The picture is further complicated by the thermal conductivity κ. This has two components, the electronic κ_e and lattice κ_l. A reduction in the electronic conductivity will also reduce κ_e but potentially not κ_l. Any changes in the electronic nature to improve S or σ will likely change κ_l as the chemical bonding is fundamentally related to the behaviour of the electrons. However, it is not obvious for many systems how they are coupled. Indeed, it may be possible to dope in such a way as to improve S, σ and κ_l. It is thus important to develop a methodology for understanding and ideally predicting, κ_l as a guide to the development of the next generation of materials.

1.1.2 The lattice thermal conductivity

κ is the rate at which heat flows from a hotter region to a cooler one, and for a system with cubic or isotropic symmetry it relates the heat flux (q) to the temperature gradient $^{\partial T}/_{\partial x}$ such that

$$q = -\kappa \frac{\partial T}{\partial x}.$$

In this work the focus will be on the lattice thermal conductivity as outlined above, the lattice contribution is given by the summation over all possible vibrations within the system such that

$$\kappa_l = \sum_{\vec{k}} \sum_{s=1}^{3N} c_{\vec{k},s} v_{\vec{k},s}^2 \tau_{\vec{k},s},$$

where $\vec{k}$ is a wavevector (all must be considered), s is the polarization index (of which there are 3 corresponding to x, y and z for every unique atom), v is the group

velocity and τ the lifetime. c is the thermal capacity which is given by

$$c_{\vec{k},s} = \frac{k_B}{V}\left(\frac{h\omega_{\vec{k},s}}{k_B T}\right)^2 \frac{e^{\frac{h\omega_{\vec{k},s}}{k_B T}}}{\left(e^{\frac{h\omega_{\vec{k},s}}{k_B T}} - 1\right)^2}$$

with ω the frequency of vibration and V the volume [12].

A widely used simplification is that of the Debye model for heat capacity. In this case only the vibrations which correspond to propagation of sound are considered, as they tend to dominate the vibrational spectrum at low energies, and as the non-acoustic vibrations typically have small propagation velocities, also the thermal transport. This still leaves the problem of determining the lifetimes. There are a number of complicated computational approaches [12] but in the crudest approximation it can be determined experimentally by fitting the measured thermal conductivity.

1.2 Novel Superconductors

Superconductivity was first observed in solid Hg in 1911 [13]. It was another 40 years before a theory was developed which could explain the elemental superconductors. This is known as the BCS (for Bardeen, Cooper and Schrieffer) theory of superconductivity [14] in which pairs of electrons form a composite boson which can then undergo Bose-Einstein condensation at low temperatures [13]. In the BCS theory, electrons become paired via an interaction with the lattice dynamics. This is neatly evidenced by the "isotope effect" in which the superconducting transition temperature (T_c) is related to the mass of the atoms which make up the crystal lattice. According to BCS theory

$$T_c \propto M^{-\alpha},$$

where M is the isotope mass and α is 0.5. A number of elements (such as Zn, Pb and Hg) agree with this theory well. However other elements do not, for example in Ru $\alpha = 0.0$, and this different behaviour has been attributed to strong coupling effects [13]. Of the systems which seem to be mediated by the conventional BCS theory the maximum T_c is found in that of MgB_2 at 39 K [15]. This is far too cold to be useful for widespread technological applications as the cooling costs would be too large (although MgB_2 is finding some small scale applications in cryogen free MRI scanners).

There is, however, a growing class of materials known as "unconventional" superconductors which do not follow BCS theory. These materials still lack a comprehensive theoretical description but have been known about since 1979 [16]. There are several key classes of unconventional superconductors and, as with the unconventional superfluid ^{3}He, there may well be more than one pairing mechanism at work [16]. The first unconventional superconductor was $CeCu_2Si_2$, joined quickly by UPt_3 and UBe_{13}. These materials are examples of heavy-fermion systems where the electrons have an effective mass of several hundred times the bare electron mass [17], furthermore they are magnetic which should be inconsistent with superconductivity. When tuned (by doping or pressure), however, the magnetism is suppressed and at the point at which the magnetism should be completely destroyed a superconducting dome appears, as shown in figure 1.1.

In the unconventional materials generally superconductivity and magnetism appear closely related. The class of materials which is currently most promising for commercial application is the cuprates (as T_c is above 77 K [18] where N_2 liquefies reducing cooling costs considerably), and here again the superconductivity appears close to the destruction of antiferromagnetic (AFM) order. The cuprates are layered materials with the Cu sandwiched between oxygen leading to quasi-two-dimensional physics in the copper layer. There are strong electron-electron correlations and these

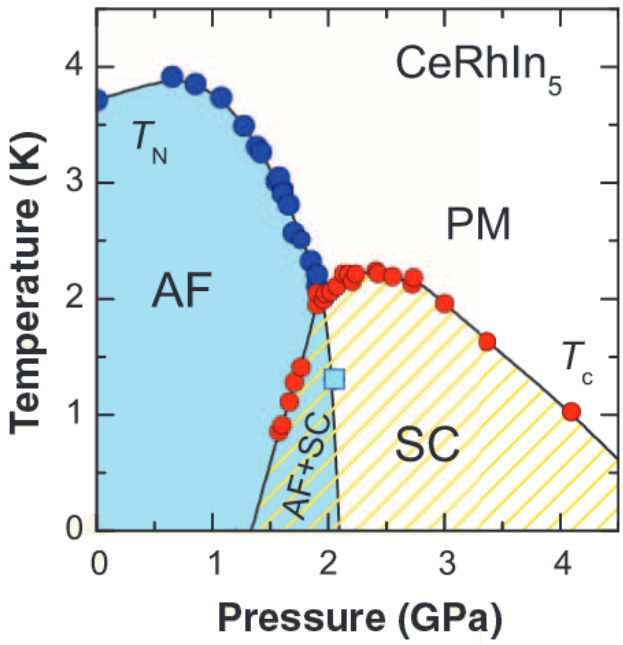

Figure 1.1: The phase diagram of the heavy fermion material $CeRhIn_5$ reproduced from Ref. [16]. Note that as the antiferromagnetic order (AF) is destroyed the superconducting dome (SC) appears. Above T_c the system is paramagnetic (PM).

lead to a Mott insulating state in the antiferromagnetic region [16]. Cuprate physics is now an extremely large field but there is some consensus that magnetic dynamics rather than lattice dynamics are important to the emergence of superconductivity [19].

Fairly recently a new class of superconductors based around Fe bonded to either As, P, S or Se have emerged [20]. These materials have a similar phase diagram as shown in figure 1.2 but with weaker correlations [16]. Many of these materials are metals rather than Mott insulators because of the weaker correlations but again the magnetic fluctuations are believed to be important [21].

Thus it is important to determine the magnetic ground state in these materials. There is strong magneto-elastic coupling which makes the lattice dynamics an extremely sensitive probe of the magnetic order [22, 20]. Thus a model which correctly

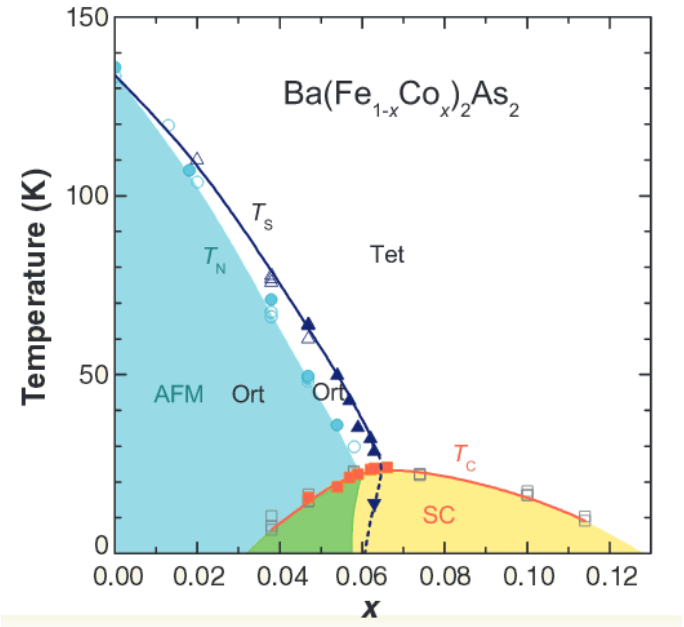

Figure 1.2: The phase diagram of the Fe superconductor $Ba(Fe_{1-x}Co_x)_2As_2$ reproduced from Ref. [16]. As with the heavy fermionic systems and cuprates AFM is suppressed continuously but the point at which it is destroyed is masked by the superconducting dome. This Fe superconductor also has a structural phase transition associated with the formation of the AFM state.

describes the lattice dynamics in the Fe superconductors should also describe the magnetism correctly. This could be used to determine the exact ground state (and indeed the structural excitations), an important step in devising a model for these systems. Such a model might make it possible to design materials with improved superconducting properties.

1.3 Synopsis

In this thesis two main materials are studied. The lattice contributions to the thermal conductivity of the thermoelectric Na_xCoO_2 and the lattice dynamics of the unconventional superconductor based on FeSe layers. Although initially these two compounds appear very different, they have key physical properties in common.

For example, when water is intercalated in Na_xCoO_2 it becomes an unconventional superconductor [23]. FeSe with K intercalated between the layers exhibits a very large positive and negative Seebeck coefficient at room temperature depending on the K concentration [24]. Beyond these comparisons both materials form superstructures which play a pivotal role in controlling both the thermoelectricity [25] and unconventional superconductivity [26].

The experimental and computational tools used to investigate these materials are discussed (chapters 2 and 3) before beginning with the investigation of κ_l in $Na_{0.8}CoO_2$ in chapter 4. In chapter 5 the role of doping and changing superstructures and their influence on κ_l in Na_xCoO_2 is probed. The FeSe superconductors are discussed in chapter 6 with a focus on their superstructure ordering energetics and the lattice dynamics across a symmetry breaking phase transition. Finally in chapter 7 the work is summarised and some future outlooks given.

Chapter 2

Experimental probes

The experimental components of this thesis mostly use inelastic scattering from x-rays and neutrons to probe the lattice dynamics of crystalline systems, as the wavevectors of typical lattice excitations are well matched to both forms of radiation. Furthermore neutrons have similar energy scales making it relatively easy to perform energy and momentum resolved measurements with them. Thanks to advances in x-ray techniques it is now also possible to do this with x-ray scattering as well.

In this chapter we will start with elastic scattering from an ordered solid to explain the basic principles of scattering and will then look at how symmetry applies to crystalline systems which will be particularly important when we consider the theory of lattice dynamics later on. There is then a discussion of neutron and x-ray production and how the different sources are exploited to build "simple" instruments. These principles are then generalised to describe inelastic scattering and inelastic instruments. Finally the way in which samples are prepared and initially characterised are briefly touched upon.

2.1 Elastic scattering

2.1.1 Scattering from an atom

The most obvious place to start when considering how atoms will scatter radiation is with a single fixed atom. Consider a constant stream of particles of wavelength λ travelling along a direction x. This can be described by the complex plane wave

$$\Psi = \Psi_0 e^{ikx}$$

with $|\Psi_0|^2$ the incident particle flux and $k = {}^{2\pi}/_{\lambda}$ the wavevector. If we place our atom at the origin so that any scattered particle will have the final wavevector $\vec{k_f}$ parallel to a displacement vector $\vec{r}$ then our scattered particle's wavefunction will have the form

$$\Psi_f = \Psi_0 f(\lambda, \theta) \frac{e^{i\vec{k_f}\cdot\vec{r}}}{r} = \Psi_0 f(\lambda, \theta) \frac{e^{i|\vec{k_f}||\vec{r}|}}{r},$$

where θ is half the angle between $\vec{r}$ and x and $f(\lambda, \theta)$ is the probability of our wave being scattered in a particular direction. This value depends greatly on the relative size of the wavelength compared to the atomic size.

2.1.2 Angular dependence of the scattered intensity

It is worth considering for a moment the form that $f(\lambda, \theta)$ will have for different values of λ and θ. First consider the case where λ is comparable to the size of our atom. Our wave can be scattered by any part of the atom. For small values of θ this will have no effect as as all possible path lengths will be similar. As θ increases however the path length from the front and back of our atom to $\vec{r}$ is no longer the same. This leads to an interference effect which suppresses the scattered intensity reaching a minimum at $\theta = \pi$. If however our wavelength is much larger than our

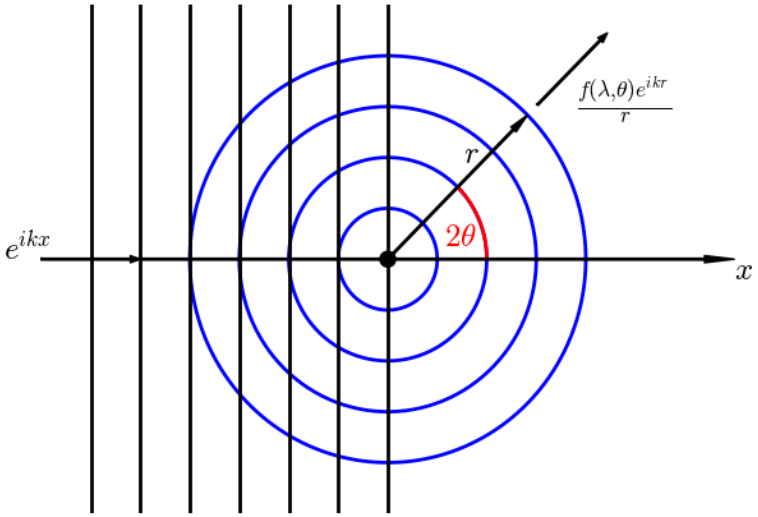

Figure 2.1: The geometry of a steady stream of particles being scattered by a single atom

scattering site then $f(\lambda, \theta)$ is entirely independent of θ. The first of these cases would be true if our atom is irradiated by x-rays. Here the x-rays interact with the cloud of electrons which is comparable in size to a typical x-ray wavelength, this is known as the x-ray form factor. If however our atom is exposed to a beam of neutrons of the same wavelength the second case will apply. This is because the neutrons interact via the strong-nuclear force and the nucleus is much smaller than the typical Angstrom wavelength of a neutron [27].

2.1.3 Scattering from many atoms

We can now extend this to consider scattering from a number of atoms. Now our incident beam is a complex plane wave with wavevector $\vec{k}_i = (K, 0, 0)$. An atom j

sitting at $\vec{R}_j$ will scatter the incident beam according to

$$\Psi_{f,j} = \Psi_0 e^{i\vec{k}_i \cdot \vec{R}_j} f_j(\lambda, \theta) \frac{e^{i\vec{k}_f \cdot (\vec{r} - \vec{R}_j)}}{|\vec{r} - \vec{R}_j|},$$

here $\vec{r}$ corresponds to our point of observation. We can easily now consider all atoms in the system by summing over j. This leads to our final scattered wave having the form

$$\Psi_f = \Psi_0 e^{i\vec{k}_f \cdot \vec{r}} \sum_{j=1}^{N} f_j(\lambda, \theta) \frac{e^{i(\vec{k}_i - \vec{k}_f) \cdot \vec{R}_j}}{|\vec{r} - \vec{R}_j|},$$

where N is the total number of atoms in our system. Henceforth the wavevector transfer $\vec{k}_i - \vec{k}_f$ will be defined as $\vec{Q}$. This setup makes the implicit assumption that each scattering process has a negligible effect on the incident beam and that a scattered beam will interact with nothing else. Generally this is a reasonable assumption as the interaction strength for both neutrons and x-rays is small. However when dealing with large samples multiple scattering can become an important consideration.

Generally our detector sits a relatively large distance from the sample (many times the actual sample size). This enables us to make the approximation that $\vec{r} - \vec{R}_j = \vec{r}$ or that $|\vec{r} - \vec{R}_j| = r$. Furthermore, the actual probability of observing a scattered particle in our detector is the modulus squared of our wavefunction. Taking the modulus squared and noting that , $\left| e^{i\vec{k}_f \cdot \vec{r}} \right|^2 = 1$ we obtain

$$|\Psi_f|^2 = \left| \frac{\Psi_0}{r} \sum_{j=1}^{N} f_j(\lambda, \theta) e^{i\vec{Q} \cdot \vec{R}_j} \right|^2 .$$

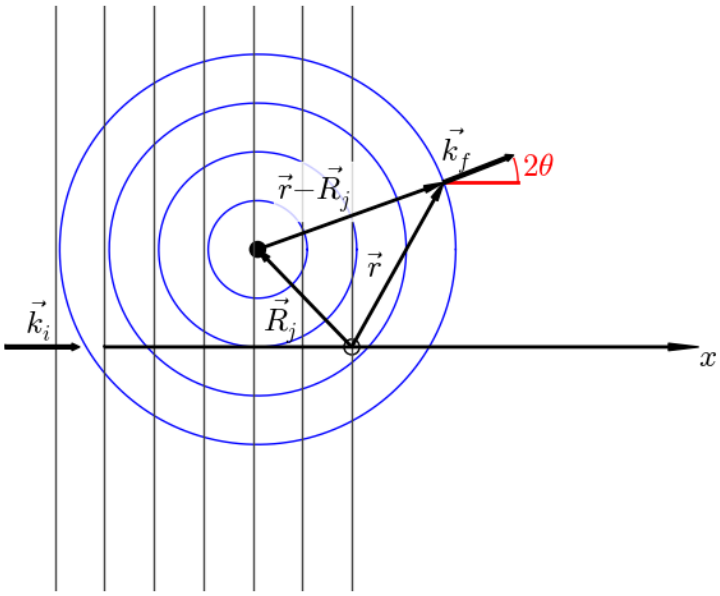

Figure 2.2: The geometry of scattering from an atom at a point relative to an arbitrary origin. Summing over these contributions allows the description of the collective scattering from an assembly of atoms.

2.1.4 The Crystal Lattice

We now have the mathematical foundations to calculate the elastic scattering from any arrangement of atoms. Unfortunately the number of atoms in most samples is of the order of 10^{23} (this can be several orders of magnitude in either direction). This would require several years to compute the intensity of a single $\vec{Q}$ on even the most powerful computers. We can greatly simplify this problem by considering a highly repetitive structure. In such a case we can factorize out the repetition and just consider a summation over a small number of atoms. We can express this periodicity mathematically as

$$\beta(\vec{r}) = \beta(\vec{r} + n_1\vec{a} + n_2\vec{b} + n_3\vec{c})$$

for any set of integers n_1, n_2 and n_3. The parallelepiped which is defined by $\vec{a}$, $\vec{b}$ and $\vec{c}$ is the smallest section that we can consider and is called the unit cell. The angles between these vectors are known as α (between $\vec{b}$ and $\vec{c}$), β (between $\vec{a}$ and $\vec{c}$) and γ(between $\vec{a}$ and $\vec{b}$).

This enables us to rewrite our intensity in terms of two summations, the first over all the atoms within the unit cell and the second over all the cells such that

$$|\Psi_f|^2 = \left| \frac{\Psi_0}{r} \sum_{k=1}^{cells} \sum_{j=1}^{n} f_j(\lambda, \theta) e^{i\vec{Q}\cdot(\vec{R}_k + x_j\vec{a} + y_j\vec{b} + z_j\vec{b})} \right|^2 .$$

Now $\vec{R}_k$ is the position of the cell we are considering and u, v and w are the fractional co-ordinates of the j^{th} atom within the cell. However, we can note that

$$\left| \sum_{k=1}^{cells} e^{i\vec{Q}\cdot\vec{R}_k} \right|^2 = N_{cells}^2,$$

so that,

$$|\Psi_f|^2 = \frac{\Psi_0^2 N_{cells}^2}{r^2} \left| \sum_{j=1}^{n} f_j(\lambda, \theta) e^{i\vec{Q}\cdot(x_j\vec{a} + y_j\vec{b} + z_j\vec{b})} \right|^2 .$$

The simplification is only valid for $\vec{Q} \cdot (x_j\vec{a} + y_j\vec{b} + z_j\vec{c}) = 2\pi n$ where n is a integer. If we lack this periodicity then the summation over all cells will interfere destructively resulting in no intensity. If we consider a possible solution for $\vec{Q}$ of the form

$$\vec{Q} = h\vec{a^*} + k\vec{b^*} + l\vec{c^*},$$

with h, k and l as integers and

$$\vec{a^*} = \frac{2\pi\vec{b}\times\vec{c}}{\vec{a}\cdot(\vec{b}\times\vec{c})},\ \vec{b^*} = \frac{2\pi\vec{c}\times\vec{a}}{\vec{a}\cdot(\vec{b}\times\vec{c})},\ \vec{c^*} = \frac{2\pi\vec{a}\times\vec{b}}{\vec{a}\cdot(\vec{b}\times\vec{c})}.$$

from scalar triple products (using $\vec{a^*}$ as an example)

$$\vec{a}\cdot\vec{a^*} = 2\pi,$$

while

$$\vec{a}\cdot\vec{b^*} = \vec{a}\cdot\vec{c^*} = 0.$$

This is important because it tells us that when $\vec{Q}$ corresponds to an integer hkl our intensity will be at a maximum for a given uvw. Away from integer values of hkl the scattering from each ion will have a different phase and very quickly the intensity will decay to zero. This implies that there are special points in $\vec{Q}$ where elastic scattering is allowed. These points are known as the reciprocal lattice and they are defined by $\vec{a^*}$, $\vec{b^*}$ and $\vec{c^*}$ the reciprocal lattice vectors.

2.1.5 Bragg's Law

It is on occasion useful to consider another construction for calculating where scattering will occur. We have already seen a periodic system can be defined in terms of the vectors $\vec{a}$, $\vec{b}$ and $\vec{c}$. Any three non-collinear vectors will define a plane, thus we can define different planes of atoms using these vectors multiplied by integer values. For us to observe scattering the waves which interact with each of these planes need to add coherently. Thus at a given 2θ the path difference must be an integer multiple of the wavelength. This set-up is shown in figure 2.3 and thus we

can see that the change in path length (for a given planar space d) is given by

$$\Delta L = 2d \sin\theta$$

and that

$$N\lambda = 2d \sin\theta.$$

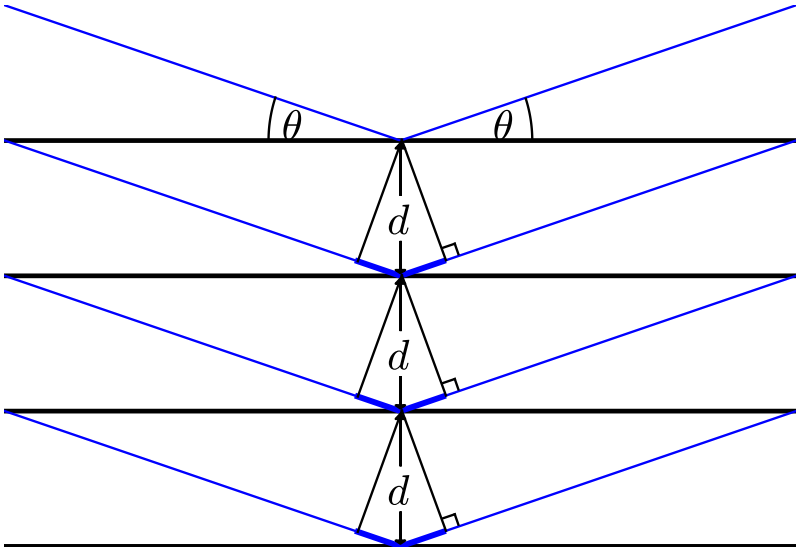

Figure 2.3: The set-up of Bragg's law. $\vec{Q}$ is perpendicular to the planes.

This result is known as Bragg's law and it is one of the best known in scattering theory. It is useful to relate this to the wavevector $\vec{Q}$ we encountered earlier. Since our incoming waves are reflected away at the same angle as they are incident on the plane, $\vec{Q}$ must be normal to the plane. By drawing the triangle of scattering defined by $\vec{k_i}$, $\vec{k_f}$ and $\vec{Q}$ it is clear that

$$\frac{|\vec{Q}|}{2} = |\vec{k_i}| \sin\theta = \frac{2\pi}{\lambda} \sin\theta$$

or

$$|\vec{Q}| = \frac{4\pi \sin\theta}{\lambda},$$

therefore

$$|\vec{Q}| = \frac{2\pi}{d}.$$

This implies that the integer values hkl that were encountered earlier are in fact related to the inter-planar spacing.

2.1.6 Symmetry

The problem has now been simplified to a summation over a relatively small number of atoms. However we can go further and use symmetries to further reduce the complexity of our problem. There are a number of different symmetries which can be exploited to describe our crystal structure. Here they are only listed with a more detailed discussion in appendix A. A proper discussion is also given in the International Tables of Crystallography Volume A and A1 [28, 29]. The complete list of symmetries are mirror planes, rotation axes, inversion symmetry, rotoinversions, glide planes and screw axes.

2.1.7 Short range order

We have thus far completely ignored the possibility of vacancies or dopants which could break the translational symmetry we have relied upon to simplify our problem. Let us consider vacancies which have no correlations between them. We can take account of this for the Bragg diffraction by reducing $f(\lambda, \theta)$ (i.e. if we have 10% vacancies $f_{vac}(\lambda, \theta) = 0.9f(\lambda, \theta)$). Uncorrelated dopants can be treated in much the same way, where extra ions are added to a particular site with their own $f_{dopant}(\lambda, \theta)$.

While these remain uncorrelated and there is no response from the neighbouring atoms then the main change will be the intensity of our Bragg peaks (there will also

be an increased flat background). However other atoms will normally move relative to the vacancy. In the case of a dopant it will almost certainly have a different ionic radius (and may have a different charge state too) and this will disturb the nearest neighbours. These motions are normally fairly small and have a correspondingly small effect on the intensities of the Bragg peaks. We now have two different types of sites, the original sites and a perturbed site. These two kinds of site will lead to interference effects between them causing scattering away from our main peaks. The positions of this scattering will depend on the displacement from the original positions. If the motions are at all asymmetric or other ions move in response to them the scattering can very quickly become complicated in $\vec{Q}$ and an analysis of this "diffuse" scattering can be a powerful tool in the study of disordered vacancies [30].

In many systems dopants (and indeed vacancies) will cluster together [31]. This clustering will also give diffuse scattering with the cluster size being inversely proportional to the width of this diffuse scattering.

2.1.8 Superlattices

In some cases the interactions between vacancies are strong enough that rather than simply clustering they actually adopt a long-range-ordered pattern which sits on top of the underlying unit cell. In such a case the scattering will be made up of two components. The first will be the principal Bragg reflections from the underlying unit cell, the second will be much weaker (a system with 10% vacancies might have extra reflections a few percent of the strength of the main peaks) but still sharp in $\vec{Q}$ with the periodicity reflecting the larger cell.

These can be given their own set of lattice parameters which can be expressed in terms of the unit cell lattice parameters. Where the symmetry of the supercell is lower than the unit cell then multiple domains with different orientations relative

to each other will form. Each will give scattering at different points in $\vec{Q}$ away from the principal Bragg reflections, but they will all contribute to the main Bragg reflections.

In some systems the correlations are not strong enough to adopt this long-range order in all directions. This is easiest to imagine in a layered compound where the correlations within a plane may be very different from those between them. In such a situation the scattering from the superlattice will be sharp in two directions but diffuse along the third.

2.1.9 Incoherent scattering

Here we have implicitly assumed that the scattering from our sample is entirely coherent. This is not necessarily the case. For example, neutrons have both a coherent and incoherent interaction with atomic nuclei. The incoherent in this case has two different origins, the nuclear spin and isotopic incoherence. The origin of incoherent scattering is in deviations from the mean scattering length of the system. Since a neutron has spin $\pm 1/2$ and the nucleus spin does not have to be zero there can be different interaction probabilities for spin up and spin down neutrons. This leads to two different cross sections and if they are not ordered (which would only occur at extremely low temperatures), incoherent scattering. Isotopic incoherence arises from the fact that the neutron scattering cross section is based on the strong nuclear force. A change in the number of neutrons in the nucleus will change the strong force interaction and again lead to different scattering cross sections. The exact weighting of isotopes will change the incoherent cross section (with the maximum being a 50-50 split assuming only two nucleons) [32]. Here we have not exploited the incoherent cross section although it can be used to probe non localised ionic motion (such as diffusive processes) and it simply contributes a flat background [33].

2.2 Sources and elastic instruments

2.2.1 Lab Sources

While the first neutron sources were lab based, [34] they do not produce enough neutrons to be useful to us in a scattering experiment. For this reason the only lab based source of radiation used in this thesis is the Xcalibur x-ray diffractometer. In this system x-rays are produced by knocking an electron out of the inner state of a molybdenum atom. When an electron falls back into this state an x-ray of the energy corresponding to this transition is emitted. The actual layout of a simple x-ray source is shown in figure 2.4. Here electrons are produced by a heated filament and accelerated across a potential difference where they collide with the molybdenum target, producing x-rays in two ways. The first is that described above which produces a narrow band of x-ray energies, there are other variants of this transition which correspond to excitations to a higher energy level and they will also produce x-rays of this characteristic energy. The second kind of x-ray emission is caused by the electrons slowing as they interact with the target. This deceleration causes emission over a wide range of energies up to a maximum corresponding to the voltage applied to the electrons. This continuous spectrum is known as bremsstrahlung radiation (from the German to break). The maximum x-ray intensity here is limited by the ability to cool the target. This beam is normally monochromated with the chosen x-ray energy corresponding to the K_α line (a transition from $2p \rightarrow 1s$) as this is the most likely transition and thus most intense. The Xcalibur instrument is monochromated however Agilent Technologies (the manufacturer) do not release the details of this monochromator.

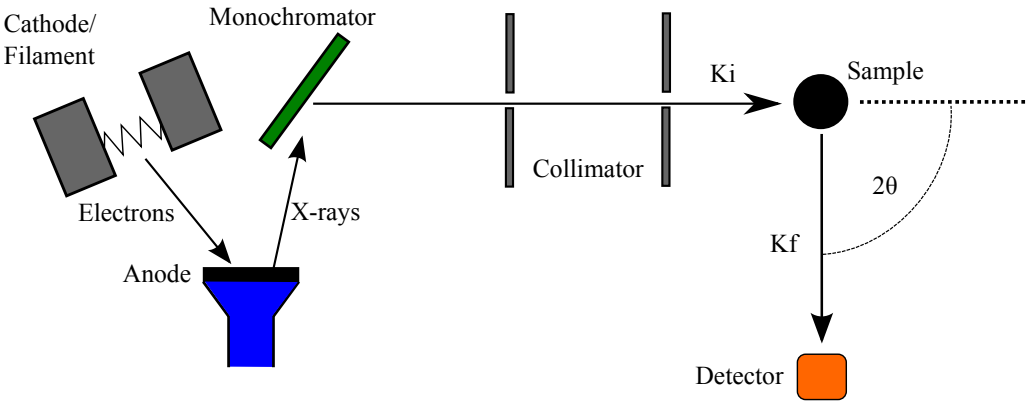

Figure 2.4: A simplistic view of a monochromated lab diffractometer. Electrons produced at the cathode are accelerated across the potential difference to the anode which is made of Mo. This bombardment produces x-rays which are then monochromated. The relatively small size of such a set-up even constrains the maximum possible resolution due to beam divergence.

2.2.2 Synchrotron X-Rays

The level of x-ray intensity from a tube source is sufficient for a standard x-ray crystallography experiment, however, often we require higher resolution, shorter counting times or other more complicated techniques one of which will be covered later. In this case much higher incident x-ray brilliance (defined as photons /s /mrad^2 /mm^2/ 0.1%bandwidth) is required. As discussed with the bremsstrahlung radiation an accelerating charged particle will emit radiation with spectral characteristics depending on the acceleration applied. This can happen in a synchrotron when the particles are bent around a corner via a magnet. This process is of great inconvenience to particle physicists as it limits the maximum attainable particle energy (it is for this reason that the tunnel in which the LHC sits has a 27 Km circumference). The first x-ray experiments using synchrotron radiation were parasitic, in that they were attached to either currently operating or recently decommissioned particle physics experiments. However, this seriously limited the possible intensity as the beam characteristics were designed (understandably) for the particle physics

experiments not the optimal operation of the x-ray experiments. This led in 1981 to the opening of the first synchrotron dedicated to x-ray research at the Daresbury laboratory.

These second generation sources still used bending magnets but achieve a brilliance around 5 orders of magnitude higher than the best lab sources. This is still not enough for a variety of x-ray techniques, particularly where the highest resolution is required as this involves discarding most of the photons produced. To meet these demands third generation sources were constructed beginning with the European Synchrotron Radiation Source (ESRF) in Grenoble. In addition to the bending magnets of the earlier sources, here special"insertion devices" increase the brilliance by another 5-6 orders of magnitude over bending magnets. These insertion devices come in two distinct types, undulators and wigglers. The undulator has a number of closely spaced permanent magnets placed neighbouring each other such that the electrons oscillate as they pass along the undulator. The cones of x-rays emitted at each bend in the electrons' path are coherent, allowing a constructive interference effect resulting in several peaks narrow in energy. This beam is highly collimated in both the horizontal and vertical directions. By physically changing the gap between top and bottom magnets the field strength and consequently the energies of the x-ray peaks can be adjusted. The wiggler is very similar to the undulator in its principle of operation however it uses larger fields with fewer sets of magnets. This means that the beam is not coherent leading to a larger flux in a continuous spectrum with a larger beam divergence.

Although the beam produced by an undulator has naturally favourable characteristics, x-ray optics can further reduce the beam divergence and improve the monochromation. The design and operating principles of x-ray optics are complicated and not relevant to this thesis, therefore, the interested reader is directed to the x-ray data booklet [35] for a discussion of this. Typical x-ray beamline optical

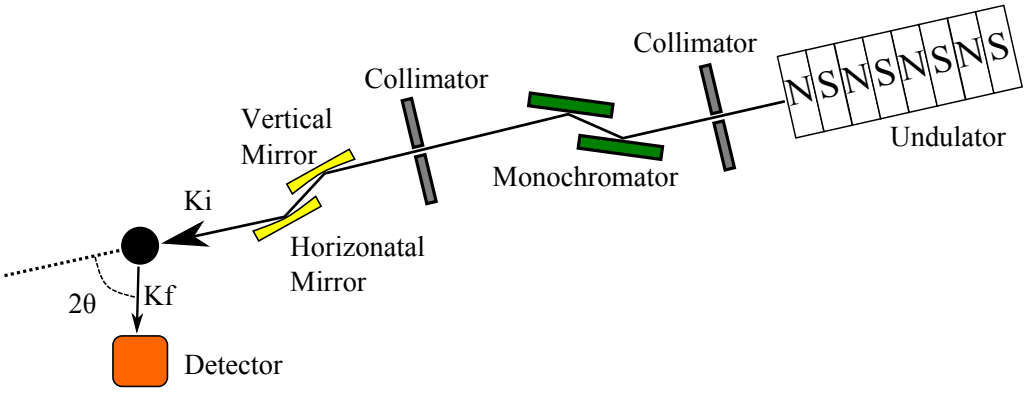

Figure 2.5: A schematic diagram of a synchrotron diffractometer. Relativistic electrons are passed through the undulator producing an intense beam of somewhat monochromatic x-rays. A complicated set of optics is used to produce the required beam characteristics. A double bounce monochromator is used because these beamlines are quite long (maybe 40m or more) and there can be space for 30 undulators around a typical synchrotron. Thus by keeping the beamline tangential to the synchrotron they do not overlap.

components are slits (to improve the collimation), a monochromating crystal (which uses Bragg's law to pick a particular wavelength) and mirrors to focus the beam. Thus a typical x-ray beamline for diffraction may look something like that shown in figure 2.5. As the monochromation is done via a crystal exploiting Bragg's law there can be higher order contamination $n = 2, 3....$ of the beam. Typically this is suppressed by several orders of magnitude with mirrors (exploiting the wavelength dependence of reflection). In both lab and synchrotron x-ray sources a single fixed detector will cover only a single point in $\vec{Q}$. For this reason all simple diffraction instruments use a"four-circle" set-up. In this the four angles are 2θ which moves the detector, θ which moves the whole sample assembly about z (where the direct beam defines x and y is parallel to the floor), κ which rotates the sample about y when $\theta = 0$ and ϕ which rotates only the sample about z (when $\theta = \kappa = 0$). This enables any point in $\vec{Q}$ to be reached by a single detector.

2.2.3 Reactor Neutrons

As we have mentioned in addition to x-rays, neutrons with energies of the order 10 to 100 meV also have wavelengths comparable to the interatomic spacing of materials and are very well suited to a scattering experiment. Furthermore they have a magnetic moment which makes it possible to carry out a magnetic scattering experiment analogous to the structural example above. Neutrons however are very challenging to produce at a level where the neutron flux is useful. One possible source of neutrons which has been available since the 1940s is a nuclear reactor.

The minimum requirement for a reactor is a fissionable material (typically uranium, thorium or plutonium), a moderator and control rods. All reactors also have biological shielding to protect the operators. The reactor at the Institut Laue-Langevin (ILL) which has been used in this thesis is fuelled by ^{235}U and it is that which we shall consider here. When a ^{235}U nucleus splits on average 2.7 neutrons are released with an energy of the order of 1 MeV. When another ^{235}U nucleus captures one of these neutrons it undergoes a fission event of its own and a chain reaction can begin. Due to their wavelike properties the neutron capture cross section is limited by their wavelength and not the target nucleus size. Neutrons with longer wavelengths have a greater capture cross section and it is for this reason that the moderator is present. Typically this moderator is a light element either ^{12}C or ^{2}H and the recoil of these nuclei following a collision allows the neutron to rapidly lose energy. ^{1}H was not used in early reactors because it has a relatively large neutron cross section and without a high ratio of ^{235}U to ^{238}U it is very challenging to maintain a critical reaction [36]. The control rods are typically made of a neutron absorber such as cadmium or boron and used to keep the reactor exactly critical (where exactly 1 neutron is absorbed by a ^{235}U atom per fission process).

Since an excess of neutrons is produced per fission it should be possible to utilise

the 1.7 neutrons not required to maintain the reaction. At ILL the core is a single fuel element consisting of very highly enriched uranium (93% ^{235}U) surrounded by a heavy water moderator. The principal moderation of the core however is performed by the light water coolant. The heavy water moderator around the core reflects neutrons back towards it and this causes a peak in the neutron flux just outside the reactor core. It is here that the beam pipes are situated to carry the neutrons away towards the instruments. These tubes do not point directly at the core as this would lead to a large background from gamma rays and fast (unmoderated) neutrons. Several of the beam tubes point at small areas made of moderators at different temperatures. There is one hot source, a graphite block at 2400 K and two cold sources which are liquid hydrogen at 25 K. These sources and the thermal heavy water moderator produce neutrons with Maxwellian distributions peaked at energies corresponding to their respective temperatures.

Thus at a particular instrument we have a continuous beam of neutrons with a Maxwellian distribution of wavelengths. While this can be used in a Laue experiment in this thesis we are mostly concerned with monochromatic beams, so just as in the case of an x-ray experiment a monochromating crystal is used. $\lambda/2$ contamination is also a problem, this unwanted component can be removed with filters.

There are two kinds of filter, the first works by scattering the shorter wavelength components out of the beam, the second by absorbing them. A scattering filter relies on the fact that there is a maximum wavelength which can be Bragg scattered equivalent to twice the largest d-spacing. If a polycrystal is used then regardless of how the filter is set up wavelengths larger than this limit will pass unaffected while those which can satisfy Bragg's law will be scattered. For example beryllium will not scatter neutrons above 3.9 Å and graphite above 6.7 Å. However for thermal neutrons these wavelengths are far too large to be useful. In this case pyrolytic graphite crystals can be used. They are placed in the beam with the ordered $\vec{c}$

lattice direction parallel to the beam. Scattering still takes place, picking out narrow bands which satisfy Bragg's law in this geometry. However, as shorter wavelengths are considered these bands begin to overlap drastically reducing the transmitted beam at that wavelength. An absorption filter relies on the excitation of nuclear resonances. Many materials exhibit this resonance in the eV to KeV range however there are some materials with a resonance at hundreds of meV and they can be used to remove higher order contamination. Generally this technique is used for high energy spectroscopy not used in this thesis however the interested reader will find a full discussion in reference [37].

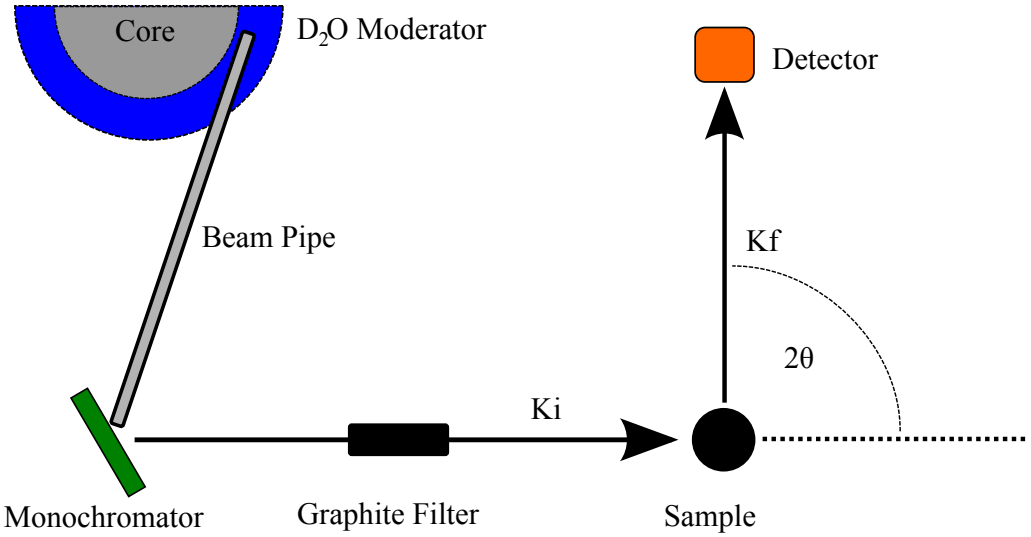

Figure 2.6: A schematic view of a reactor diffractometer. Collimation can also be added to this instrument to reduce $\Delta\theta$. It is also important to observe that the set up shown here will give a poor resolution as the outgoing beam is anti-parallel to the beam incident on the monochromator.

Thus a simple reactor diffractometer using thermal neutrons could be laid out as shown in figure 2.6. In this set-up, as with an x-ray diffractometer, the detector can measure only a single point in $\vec{Q}$ unless able to move. Due to the comparatively low flux of neutron instruments many modern designs make use of a bank of detectors to reduce counting times. The resolution of a crystal monochromator instrument is

non-trivial and a proper discussion is given in reference [38]. Here we shall consider the simplified treatment of reference [37]. Our monochromator (assuming a perfect crystal, $\Delta d = 0$) will produce a neutron beam of wavelength λ_M however our neutron beam has some divergence $\Delta\theta$ which we can see by differentiating Bragg's law leads to a spread of wavelengths

$$\Delta\lambda = \lambda_M \cot\theta \cdot \Delta\theta.$$

If this beam then interacts with a sample satisfying the Bragg condition with the final scattering parallel to the original beam then the neutrons will interact with the sample in the same way as the monochromator (i.e. neutrons with a larger Bragg angle at the monochromator will have a larger Bragg angle at the sample). In this case the divergence of the final beam is minimised, however if the final scattering is antiparallel then the divergence is maximised. The final form of the resolution is such that the peak FWHM passes through a minimum at

$$\tan\theta = \tan\theta_M \frac{\alpha_2^2(\alpha_1^2 + 2\beta^2)}{\alpha_1^2\alpha_2^2 + \alpha_1^2\beta^2 + \alpha_2^2\beta^2}$$

where α_1 is the beam divergence between source and monochromator, α_2 is the beam divergence between monochromator and sample and β is the mosaic spread of the monochromator (a term for the divergence between sample and detector is required to work out what the FWHM actually is but it has no effect on where the minimum occurs) [37]. Thus we can pick where we want the minimum in resolution to be. Normally this is at large 2θ where peaks are much more closely spaced.

2.2.4 Spallation Neutrons

While reactor sources remain the most intense neutron sources available their advancement is limited by the difficulty of removing heat from the core. This has led

to the consideration of pulsed sources where the pulse length is much shorter than the gap between pulses. This allows heat within the source to be removed before the next pulse. If the whole neutron spectrum is used then it is the peak neutron flux which determines the data collection rate not the time averaged flux which is often lower than a reactor based source. There are a number of such sources around the world (SNS in the USA and J-PARC in Japan are the most recent examples) however here we will focus on the ISIS facility as this is the only spallation neutron source which has been used in this thesis.

Spallation is a process which occurs when a nucleus is bombarded with high energy particles. This bombardment causes the target nuclei to become greatly excited. Initially there is a cascade process within the target where many high energy particles including neutrons are produced. There is then a second process by which almost all (approx. 97%) of the useful neutrons are produced where the excited nuclei sweat neutrons to cool down.

At ISIS the incident particles are protons with a typical energy of 800 MeV bunched together with a rep-rate of 50 Hz. These protons are initially accelerated by a synchrotron to their operating energy before being directed to one of two targets (4 out of every 5 bunches are sent to the first target). This target is made of tungsten clad in tantalum (tungsten is slightly soluble in water and an unclad target would lead to radioactive contamination of the coolant). While a fissile material target would produce more neutrons it would also have a large background from continuous fission events which would hamper the operation of the instruments.

After production the neutrons enter a moderator similar to those used for producing reactor neutrons. A beryllium reflector is used to get the greatest possible neutron flux into the moderator while absorbing material (such as cadmium or boron) is used to prevent neutrons which have been moderated by the reflector contributing to the background. The neutrons which leave the moderator have the same

characteristics as those from a reactor but importantly are well separated between pulses as their creation time is very short relative to the pulse length.

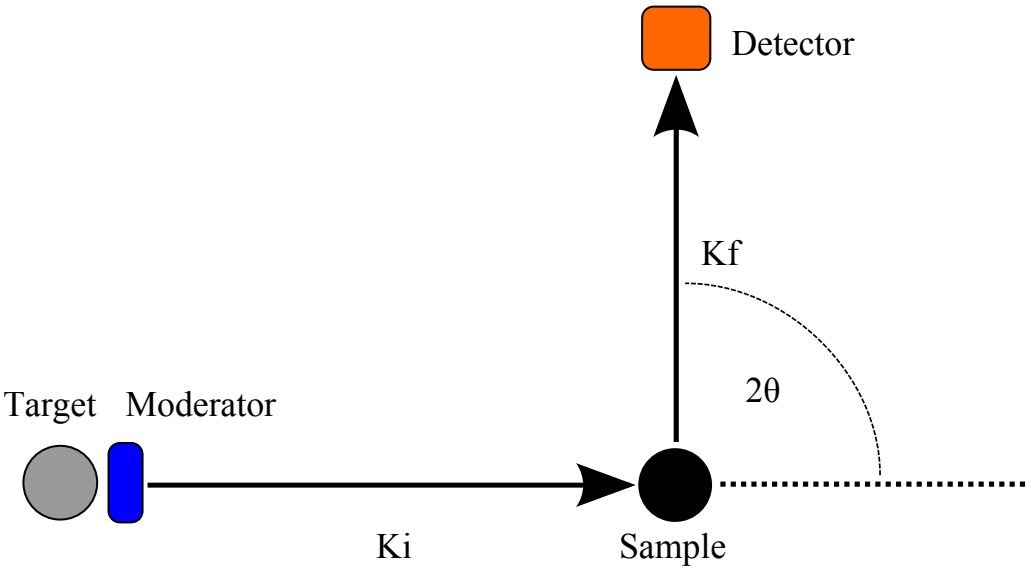

Figure 2.7: A time-of-flight diffractometer. Its fundamental layout is extremely simple as the calculation of λ is performed entirely from the time-of-flight doing away with the need of monochromators.

A simple TOF diffractometer could be laid out as in figure 2.7. In such a set-up a single detector will map out a radial line in $\vec{Q}$. The resolution of our fixed detector is limited by the length of the flightpath and it is for this reason that the high resolution powder diffraction beamline at ISIS (HRPD) is built almost 100m away from the target compared to around 10m for a standard diffractometer. We can understand why it is flight length that limits the resolution by considering the three main sources of error. The first is an uncertainty in our flight length as our moderator is of finite size (the final moderating event can happen anywhere within it). The second is an uncertainty in our time of flight as we do not know how many moderating events will happen. Finally there is an uncertainty in our scattering angle as the neutrons leaving the moderator will have some divergence. By defining Bragg's law in terms of a TOF instrument's characteristics (t, flight time, L, flight

length, θ, detector angle) we get

$$Q = \frac{4\pi m_n}{h} \cdot \frac{L \sin\theta}{t}.$$

Differentiating to calculate the individual error terms and then combining gives a total instrumental error of

$$\left(\frac{\Delta Q}{Q}\right)^2 = \left(\frac{\Delta L}{L}\right)^2 + \left(\frac{\Delta t}{t}\right)^2 + (\cot(\theta)\Delta\theta)^2.$$

Thus as we increase the flight path $^{\Delta L}/_{L}$ will decrease as it is the moderator size which defines ΔL. For a given neutron speed a longer flight path will lead to a larger t while Δt remains constant. Finally, for a given detector layout our resolution is defined by the position of the detector in θ. However there is a gain from $\Delta\theta$ as this will drop with longer flightpath as more divergent neutrons will miss the sample entirely (this is not actually the case on many neutron instruments including HRPD as neutron guides are used which reflect neutrons that would escape to increase the flux). Realistically in most TOF diffractometers the maximum resolution is limited by the gap between pulses as a very long flightpath will lead to the fast neutrons from one pulse catching up with the slow neutrons from a previous pulse.

2.3 Inelastic scattering

2.3.1 Formalism

So far we have considered only atoms which are fixed in place and have no variation with time. For a thesis with 'dynamics' in the title this may appear a small oversight and thus we now turn our attention to the consideration of atomic motion. Generally this section will follow the theoretical construction used in reference [39] before

moving on to a discussion of the instruments which can be used to measure these phenomena. Rather than reproduce the whole of the derivation contained within Ref. [39], key results which help to explain the origin of final terms will be pointed out with the reader directed towards [39] for the details.

Lattice vibrations and the harmonic approximation

In this thesis we are concerned with materials in the solid state and will also disregard the ability of ions to hop through the crystal lattice. In this set-up atoms will have an equilibrium position and if they are perturbed a restoring force will drive them back towards it. Let the vector $\vec{u}_{j,\alpha}$ represent a displacement along one of the Cartesian axes (which one is denoted by α) of atom j. We can then write the energy as a Taylor expansion such that

$$E = E_0 + \frac{1}{2}\sum_{\substack{j,j' \\ \alpha,\alpha'}} \frac{\partial^2 E}{\partial u_{\alpha,j}\partial u_{\alpha',j'}} u_{\alpha,j}u_{\alpha',j'} + \dots .$$

Here E_0 is the total energy of the lattice at equilibrium. The first order term in this expansion is zero because at equilibrium the forces must be zero. The second order term is called the harmonic energy and all higher order terms the anharmonic energy. In this chapter we will assume that the anharmonic terms are negligible and work purely within the harmonic approximation. The advantage of this approach is that it can be solved exactly (the introduction of higher order terms precludes this [39]) and gives us a framework which we can then use to recover the physics described by the anharmonic terms.

We must now consider how our atomic positions will evolve with time. The simplest possible case is to consider a one-dimensional chain of atoms along the x-axis with the equilibrium interatomic distance a. Here within the harmonic approximation and considering only nearest neighbour interactions

$$E = E_0 + \frac{1}{2}\frac{\partial^2 E}{\partial u^2}\sum_{n=1}^{N}(u_n - u_{n+1})^2.$$

We have taken the differential out of the summation as all the atoms are the same and thus it will take on a constant value (we shall call it J). E_0 in this case corresponds to the energy of the interatomic bonds times the total number of bonds $(N-1)$. Let us now consider atom n. Its energy will be

$$E_n = \frac{1}{2}J(u_{n+1} - u_n)^2 + \frac{1}{2}J(u_n - u_{n-1})^2$$

and the force (the negative first differential of the energy)

$$F_n = -\frac{\partial E_n}{\partial u_n} = J(u_{n+1} + u_{n-1} - 2u_n) = m\frac{\partial^2 u_n}{\partial t^2}.$$

If we consider a solution of the form

$$u_n = Ae^{-i(kna-\omega t)}$$

and substitute in

$$(i\omega)^2 mAe^{i(kx_n-\omega t)} = AJ(e^{i(k(n+1)a-\omega t)} + e^{i(k(n-1)a-\omega t)} - 2e^{i(kna-\omega t)})$$

using the trigonometric relations

$$\omega = \pm\left(\frac{4J}{m}\right)^{1/2}\sin\left(\frac{ka}{2}\right).$$

A negative frequency makes no physical sense and thus we consider only the modulus

$$\omega = \left(\frac{4J}{m}\right)^{1/2}\left|\sin\left(\frac{ka}{2}\right)\right|.$$

This shows that there exists a solution to the atomic motion which is a travelling wave and depends purely on the spring constant J, atomic mass m and the wavevector k. This solution has considered motion only in the direction of the chain (it is longitudinal), there will also be a set of solutions for vibrations along y and z (transverse motion) which will have a different spring constant but a similar form. Systems with more than one atom in the cell allow modes which do not go to zero at multiples of $k = {}^{2\pi}/_{a}$ but retain the periodic nature. We will return to these more complicated systems and the manner of calculating their behaviours in the next chapter. For now all that matters is that our atomic motions are expressible in the form of travelling waves (which henceforth we will refer to as phonons).

There is only one other point to be made at this juncture. We have performed this derivation without temperature which implies that the allowed values do not change with temperature. Within the harmonic approximation this is true, however, the actual displacement of an atom does depend on temperature. This is because as we increase the temperature more phonons will exist within the system perturbing our atom further from equilibrium. The total contribution to an atom's displacement is given in reference [39] as

$$u(\vec{j}) = \frac{1}{\sqrt{Nm_j}} \sum_{\vec{k},\nu} \vec{e}(j,\vec{k},\nu) e^{i\vec{k}\cdot\vec{r_j}} Q(\vec{k},\nu),$$

where ν is the label of the phonon, m_j is the mass of the j^{th} atom, $\vec{r_j}$ its position and $\vec{e}$ is known as the eigenvector of this atom for this phonon. We will discuss the calculation of $\vec{e}$ in the next chapter but for now we will simply remark that it gives information on the direction of atomic motion. The value $Q(\vec{k},\nu)$ is called the normal mode co-ordinate and has taken on both the time dependence of the phonon and its temperature contribution. A detailed discussion of this parameter is given in references [39, 40].

One phonon scattering

As highlighted above we have until now considered terms with no dependence on time. Now if we consider the scattering from two atoms, one of which we call k and the other j then there will be terms within our scattering equation of the form

$$f_j(\lambda,\theta)f_k(\lambda,\theta)e^{i\vec{Q}\cdot(\vec{R_j}(t)-\vec{R_k}(0))}.$$

Unfortunately our answer now depends on the time that at which we perform the measurement. Thankfully since in reality even a short counting time (a few seconds would be very quick) is very much larger than the typical frequency of a lattice vibration ($\sim$ THz) we can integrate over all times. Scattering from atoms at different times however still complicates the picture and a proper derivation requires rebuilding our scattering functions from a fundamentally different (quantum mechanical) perspective. Instead we shall note the fundamental similarity between our elastic scattering equations and a Fourier transform. This is no coincidence as our scattering from the real space lattice is described in reciprocal space ($\vec{Q}$) and a convenient way to move between the two is in the form of a Fourier transform. When we Fourier transform our new time dependant term we will obtain a frequency which for our incident waves will also correspond to an energy. Quoting the classical form of our scattered intensity [39] allows us to write

$$I(\vec{Q},E)=\sum_j\sum_k f_j(\lambda,\theta)f_k(\lambda,\theta)\int\left\langle e^{i\vec{Q}\cdot(\vec{R_j}(t)-\vec{R_k}(0))}\right\rangle e^{-i\omega t}dt.$$

If $\vec{R_j}(t)=\vec{r_j}+\vec{u_j}(t)$ where $\vec{r_j}$ is the equilibrium position and $\vec{u_j}(t)$ the displacement relative to this position. Then

$$I(\vec{Q},E)=\sum_j\sum_k f_j(\lambda,\theta)f_k(\lambda,\theta)e^{i\vec{Q}\cdot(\vec{R}_j-\vec{R}_k)}\times\int\left\langle e^{i\vec{Q}\cdot(\vec{u_j}(t)-\vec{u_k}(0))}\right\rangle e^{-i\omega t}dt.$$

If we exploit the properties of harmonic distributions we will obtain two exponential terms which depend upon the mean squared displacement of j and k respectively and $\vec{Q}^2$. This is called the Debye-Waller factor (or temperature factor) and applies to both elastic and inelastic scattering. Henceforth it will be referred to as $T_j(\vec{Q})$. The time dependence is then confined to a third term which when expanded as a power series (and taking only the second term as the first is simply elastic scattering and the higher multiphonon processes). We now have

$$I(\vec{Q},E)=\sum_j\sum_k f_j(\lambda,\theta)f_k(\lambda,\theta)e^{i\vec{Q}\cdot(\vec{R}_j-\vec{R}_k)}T_i(\vec{Q})T_j(\vec{Q})\times\int\left\langle(\vec{Q}\cdot\vec{u_j}(t))(\vec{u_k}(0))\right\rangle e^{-i\omega t}dt$$

We already have an expression for $\vec{u_j}(t)$ and by summing over all values of the wavevector $\vec{k}$ and applying the effect of the crystal lattice periodicity as we did in the elastic case we can write the scattering intensity as

$$\begin{aligned}I(\vec{Q},E)=N\sum_{j,k}^{n}\frac{f_j(\lambda,\theta)f_k(\lambda,\theta)}{\sqrt{m_jm_k}}e^{i\vec{Q}\cdot(\vec{R}_j-\vec{R}_k)}T_i(\vec{Q})T_j(\vec{Q})\\ \times\int\sum_\nu\left(\vec{Q}\cdot\vec{e_j}(\vec{Q},\nu)\right)\left(\vec{Q}\cdot\vec{e_k}(-\vec{Q},\nu)\right)\left\langle Q(\vec{Q},\nu,t)Q(-\vec{Q},\nu,0)\right\rangle e^{i\omega t}dt.\quad(2.1)\end{aligned}$$

The correlation function of $\left\langle Q(\vec{Q},\nu,t)Q(-\vec{Q},\nu,0)\right\rangle$ can be rewritten in the form $\left\langle Q(\vec{Q},\nu)Q(-\vec{Q},\nu)\right\rangle\cos\left(\omega(\vec{Q},\nu)t\right)$. The new correlation function has a standard solution in the high temperature limit (which as we are purely classical we can use)

of the form $\left\langle Q(\vec{Q},\nu)Q(-\vec{Q},\nu)\right\rangle = \frac{k_BT}{\omega^2(\vec{k},\nu)}$. Finally we observe that we are taking the Fourier transform of our new cosine term which will be a Dirac delta function. This gives the final classical solution as

$$I(\vec{Q},E) = Nk_bT\sum_{j,k}^{n}\frac{f_j(\lambda,\theta)f_k(\lambda,\theta)}{\sqrt{m_jm_k}}e^{i\vec{Q}\cdot(\vec{R_j}-\vec{R_k})}T_i(\vec{Q})T_j(\vec{Q}) \times\sum_{\nu}\frac{\left(\vec{Q}\cdot\vec{e_j}(\vec{Q},\nu)\right)\left(\vec{Q}\cdot\vec{e_k}(-\vec{Q},\nu)\right)\delta(E\pm\hbar\omega(\vec{Q},\nu))}{\omega^2(\vec{Q},\nu)}. \quad (2.2)$$

This compares to the full quantum mechanical solution which can be quoted as

$$I(\vec{Q},E) = \frac{N\hbar}{2}\sum_{\nu}\frac{1}{\omega(\vec{Q},\nu)}\left|\sum_j\frac{f_j(\lambda,\theta)}{m_j^{1/2}}[\vec{Q}\cdot\vec{e_j}(\vec{k},\nu)]e^{i\vec{Q}\cdot\vec{R}_j}T_j(\vec{Q})\right|^2 \times([n(\omega(\vec{Q},\nu),T)+1]\delta(E+\hbar\omega(\vec{Q},\nu))+n(\omega(\vec{Q},\nu),T)\delta(E-\hbar\omega(\vec{Q},\nu))), \quad (2.3)$$

here all of the terms are as described above but the additional n is the Bose factor. It is a weighting factor that relates to the number of phonons within the system at any one time.

A detailed derivation of this is given in [32]. It is worth pausing here to both explain the new terms involved and their physical origin (at least within a semi-classical picture). The δ function tells us that we will see phonon scattering only at sharp positions corresponding to transitions between the ground state and a single excitation. $n(\omega(\vec{Q},\nu),T)$ is known as the Bose factor and describes the phonon population at this energy. As phonons are bosons, they are described by Bose-Einstein statistics. Here E corresponds to the energy of the sample, positive $\hbar\omega(\vec{Q},\nu)$ means that our particle gives energy to the sample. This is the origin of the $+1$ on the

sample energy gain side. The Bose weighting accounts for scattering from a phonon which already exists in the sample, the +1 accounts for the sample energy gain allowing a phonon to be created by the incident radiation. We can think about phonon scattering in terms of a Doppler shift of the the incident energy. This is illustrated in figure 2.8 for the two extremes. When $\vec{Q}$ is parallel or antiparallel to $\vec{e}$ (the direction of atomic motion) the Doppler shift for $\vec{k_i}$ and $\vec{k_f}$ add constructively. If $\vec{Q}$ is perpendicular then (for example) $\vec{k_i}$ will be shortened and $\vec{k_f}$ elongated leading to no net effect. This is represented by the dot product $\vec{Q} \cdot \vec{e_j}(\vec{k}, \nu)$. Technically $\vec{e_j}$ is a complex number and only completely real at Brillouin zone centres.

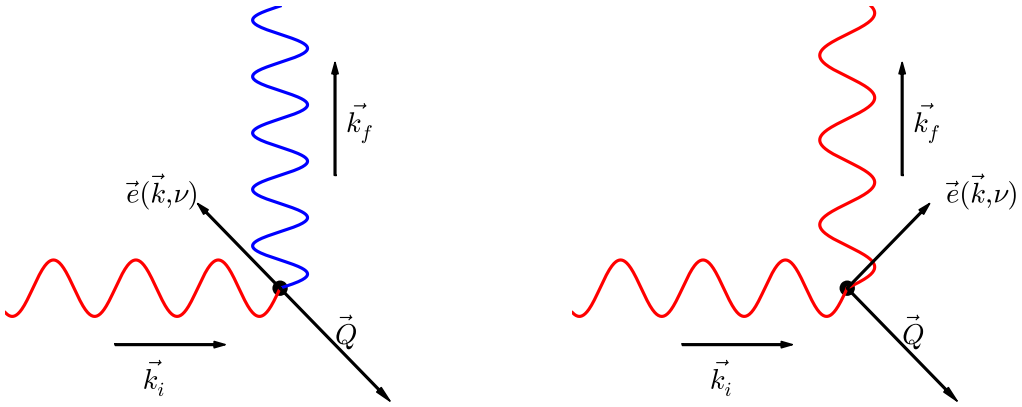

(a) (b)

Figure 2.8: The Doppler shift of an incident wave on a particle vibrating along $\vec{e}$. With k_i along x and k_f along y. (a) When the particle vibrates along a [-1,1] direction both k_i and k_f appear to have a shorter wavelength. (b) With a [1,1] vibration k_i is elongated k_f is shortened leading to no net effect.

2.3.2 The triple-axis spectrometer

Now that we have an expression for the scattering from phonons within our system we will turn our attention to their measurement. Fundamentally the problem is one of detecting a change in energy at a particular $\vec{Q}$. The first instrument layout we shall consider is the Nobel prize-winning triple-axis spectrometer [41]. We have already seen how a diffractometer on a reactor source can make use of a monochromating crystal to produce an incident beam of known energy. Use of a second monochromating crystal after the sample position to select the energy of the outgoing beam is the basic principle of operation of the triple-axis spectrometer. Our 3 axes refer to the selection of incoming energy, $\vec{Q}$ and outgoing energy. The basic layout of a triple-axis spectrometer is shown in figure 2.9. The accessible regions in our now 4D space ($\vec{Q}$ and E) are defined by the scattering triangle. If we cannot close this triangle (due to the geometry of the instrument for example) at a particular point in 4D space then it is inaccessible. An example of this triangle is shown in figure 2.10. If we use only a single detector then we can measure only a single point in 4D space at a time. Although triple axis instruments typically have the greatest flux of any reactor instrument, the weak signal of inelastic scattering tends to restrict the regions that can be measured during any one experiment.

We have already explored the resolution properties of a monochromator set-up. The same basic principles apply to the triple-axis instrument in that the best resolution will be obtained when the beam incident on the monochromator and leaving the sample are parallel. We must also consider the effect of the analyser on our resolution. In this case only the scattering angle is important and thus the analyser should be as close to backscattering as possible. Typically this dictates that it is antiparallel to the beam incident on the monochromator. The instrument will consequently look somewhat like a “W” or “M”. The actual resolution that we now

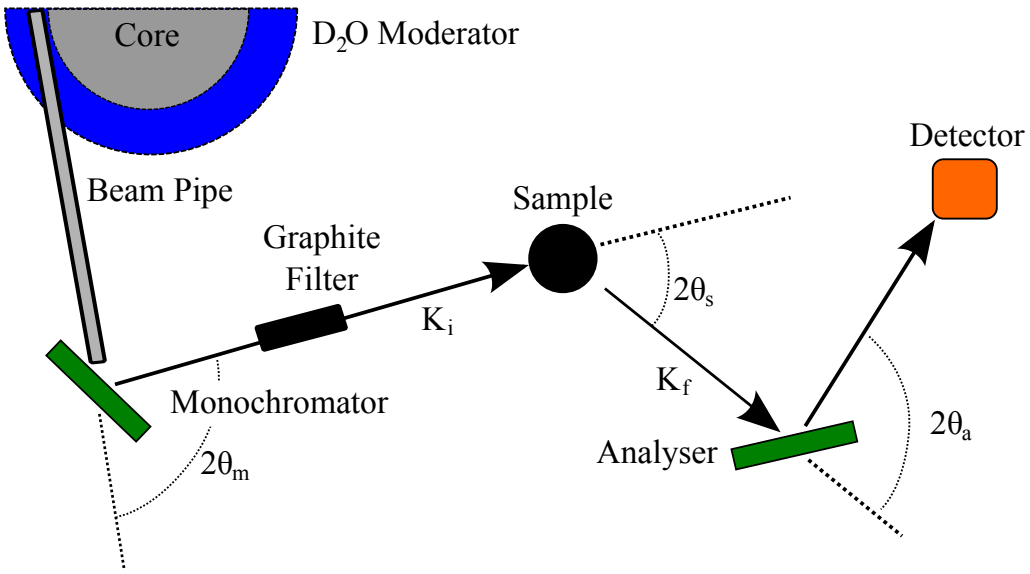

Figure 2.9: A triple-axis spectrometer such as IN8 at the ILL. The shielding has been omitted to simplify the picture but normally heavy shielding is required to minimise the background.

obtain is rather complicated and is typically ellipsoidal in $\vec{Q}$ and E. It will be tilted in the 4D parameter space with the sign of the tilt changing depending on exactly how it is set up. This resolution function is shown in figure 4.7. It is clear from this that the resolution will be much better when the gradient of the ellipsoid matches the gradient of the dispersion. For this reason when measuring highly dispersive modes care must be taken to measure on the correct side of the dispersion. Figuring out which is the "correct" side is not entirely trivial, one can either use a resolution calculation program such as McStas [42] or it can be determined experimentally moving slightly off a Bragg peak in $\vec{Q}$ and performing an energy scan through the elastic position. Due to the tilting of the resolution function the Bragg peak will appear shifted to either slightly negative or positive energy transfers and thus the optimal measurement side can be determined.

The set-up of a triple-axis spectrometer also allows you to optimise for either flux, resolution or a combination of the two. The highest resolution option involves

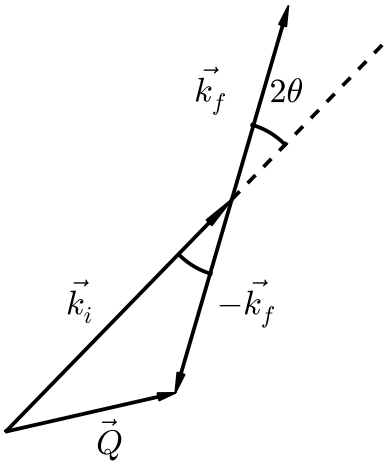

Figure 2.10: The inelastic scattering triangle where $|\vec{k_i}| \neq |\vec{k_f}|$. The magnitudes are related to each other by the cosine rule $Q^2 = k_i^2 + k_f^2 - 2k_i k_f \cos(2\theta)$ and $\Delta E = \frac{\hbar^2}{2m}(k_i^2 - k_f^2)$ in the notation used throughout this thesis.

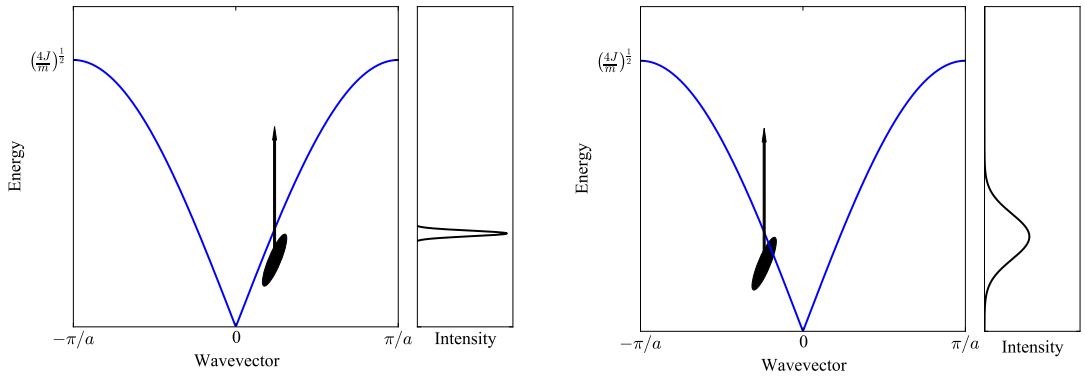

Figure 2.11: A triple-axis energy scan measuring on the correct (a) and incorrect (b) sides of the dispersion. The resolution ellipsoid (shown in black) is approximately the full width at half maximum.

placing collimators between the monochromator and sample and sample and analyser to reduce $\Delta\theta$. This has the disadvantage that it will drastically reduce the flux (obviously the finer the collimation the worse the flux). Conversely as the monochromator is normally made up of many co-aligned single crystals it is possible to bend the monochromator to focus the beam onto the sample, increasing $\Delta\theta$ and improving the incident intensity.

2.3.3 Time-of-Flight

Elastic scattering can be identified by its large signal. In this case $|k_i| = |k_f|$ can be determined from the time of flight. However, for the case of inelastic scattering, since we now allow $|k_i| \neq |k_f|$, we need a way of gathering additional information about either $|k_i|$ or $|k_f|$ as once we know one we can use the time-of-flight (TOF) to calculate the other. We will mostly focus on instruments that define $|k_i|$ (direct geometry) but a brief discussion of $|k_f|$ (indirect geometry) instruments will also be given. In a direct geometry instrument an extra piece of equipment called a chopper is placed into the incident beam. These (as the name implies) chop up the incident beam into packets. There are three kinds, helical velocity selectors, Fermi choppers and disk choppers. All are made of a neutron absorber with some form of hole, which when aligned with the beam allows neutrons to pass. By setting the delay between the opening of the chopper and the pulse from the target an incident wavelength can be selected. This will then interact with the sample and neutrons which gain energy will be detected first while those which lose energy will be detected later. A single detector will in this case map out an arc through 4D space with time of flight as $\vec{Q}$ also changes continuously with flight duration. A simple TOF spectrometer with a Fermi chopper is shown in figure 2.12.

The three different choppers are used on slightly different kinds of instruments. The velocity selector is used at reactor sources to provide a coarse monochromation

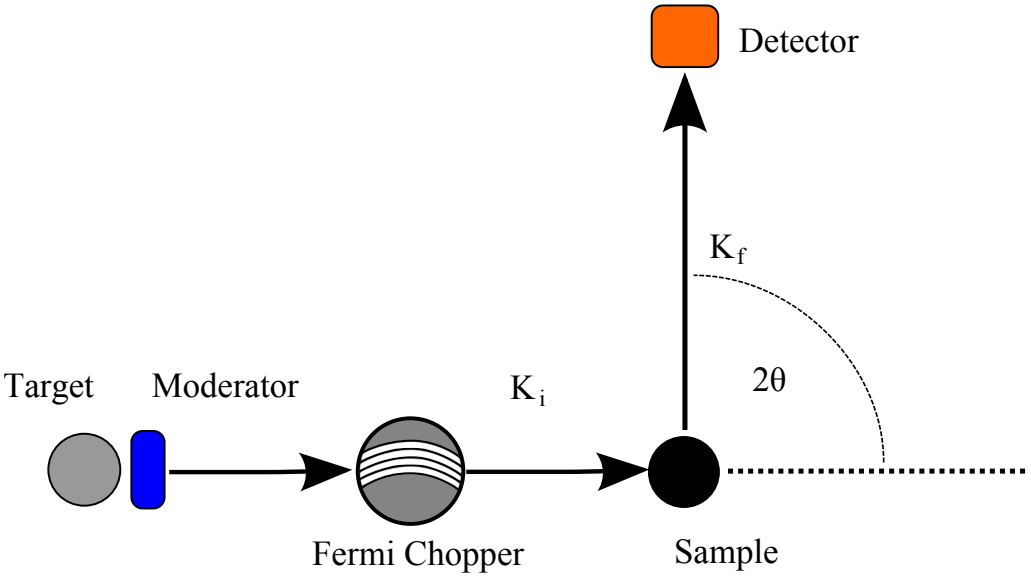

Figure 2.12: A very simple TOF spectrometer with a Fermi chopper. In this case the chopper must rotate anticlockwise to allow neutrons to pass.

of the incident beam and is effectively a cylinder with a curved groove cut into it. The curvature of the groove and the speed at which it is rotated selects the energy and its resolution. A single disk chopper can be used to produce a polychromatic pulse from a reactor source similar to that produced by a spallation source. Disk choppers on their own cannot be rotated fast enough to produce a monochromated beam from a spallation source, however, multiple disk choppers operating out of phase with each each other can. The instrument LET at ISIS uses 7 disk choppers to produce several monochromated beams per pulse allowing several different incident energies to be collected simultaneously [43]. Finally Fermi choppers consist of a cylindrical drum with curved slots running across its diameter. The cylinder is rotated perpendicular to the incident beam placing a large volume of neutron absorber between the sample and source when closed giving a very low background. Typically Fermi choppers are more compact than disk choppers allowing them to be spun faster and thus achieve higher resolution. This is the type of chopper used on the MERLIN spectrometer at ISIS which is optimised for measurements in the thermal region [44]. In general

a chopper spectrometer has much lower flux than a triple-axis spectrometer at a reactor source. For this reason it is normal to use huge detector arrays (on MERLIN they cover 180° in the horizontal plane and ±30° vertically). For a system with reduced dimensionality in its physics this allows all of the region of interest to be captured in a single shot however for three dimensional systems it is necessary to rotate the crystal in small increments to build up coverage over a larger region of $\vec{Q}$.

Finally we will briefly mention indirect spectrometers. In this case a white beam illuminates the sample and then a monochromating crystal is used to backscatter the neutrons to detectors near the sample position. In this system neutrons which lose the most energy arrive in the detector first as the final energy is fixed. These instruments can have very narrow resolution due to the backscattering geometry (IN16b at the ILL has a nominal resolution of 1 μeV [45]) but typically have a higher background than the direct geometry instruments.

2.3.4 Inelastic X-ray Scattering

Inelastic x-ray scattering is a technique which has only really been available since the late 1990s with the advent of third generation x-ray sources. The problem can be simply explained as we have a sample whose excitations are of the order of a few 10s of meV. Our incident beam energy in the x-ray region is however around 10 keV and ideally we would like an instrumental resolution of just 1 meV or less. This requires $^{\Delta E}/_{E} = 10^{-7}$ compared to neutrons which have $^{\Delta E}/_{E} = 10^{-2}$. This is technologically extremely difficult and the few instruments around the world where this technique is used are remarkable feats of engineering. Key advantages to using x-rays over neutrons are that we will never have a problem closing the triangle (as our energy transfer is negligible compared to the incident energy), the beam from a synchrotron has many orders of magnitude more flux allowing much smaller samples

and finally hard x-rays usually have a negligible magnetic cross section compared to the structural scattering so that we do not have to worry about magnetic signals. In this thesis the beamline ID28 at the ESRF has been used and it is this instrument that we will look at in more detail here, although the principles of operation are the same for other beamlines. The layout of ID28 is shown in figure 2.13.

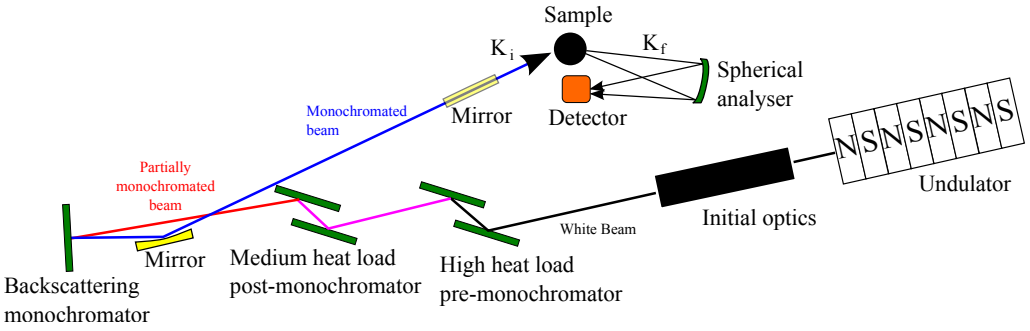

Figure 2.13: The layout of the beamline ID28 at ESRF. Much of the complicated x-ray optics has either been subsumed into the initial optics or left off entirely for clarity as, unlike a neutron instrument, there is no 'simple' layout for an inelastic x-ray beamline. On ID28 there are actually 9 detectors in the horizontal plane allowing for the simultaneous collection at different $\vec{Q}$.

The basic principle is the same as that of the triple-axis spectrometer. The incident beam is monochromated, interacts with the sample and is then monochromated again by the analyser into the detector. The main difference here is that the very intense x-rays from the undulator dump so much heat into the monochromator that it distorts, limiting the resolution obtainable with a single monochromator. For this reason ID28 has 3 monochromators all made from silicon. The first is held at $\sim$ 100 K where silicon has a maximum in its thermal conductivity and a minimum in the thermal expansion co-efficient [46], this gives a $^{\Delta E}/_{E} \sim 10^{-4}$. The second monochromator further reduces the heat load leaving the beam at $^{\Delta E}/_{E} \sim 10^{-5}$. The final monochromator is set-up in backscattering ($\theta_m = 89.98°$) for the best possible resolution. In this system the monochromator is not rotated (as we have seen for reactor neutron this changes the instrumental resolution), but is instead

heated or cooled causing a change in d-spacing and thus a change in the scattered wavelength at a constant θ_m. For the highest resolution this requires temperature control to within 0.5 mK. The analysers are made up of many small silicon crystals with focusing to match the overall beam divergence and thus maximise the overall intensity. They are held at a constant temperature so that it is only the temperature of the backscattering monochromator which defines the energy transfer being measured. For both the backscattering monochromator and analyser it is always a reflection of the kind (n,n,n) which is used (typically (9,9,9) or (11,11,11)) as for Si these are the most intense Bragg reflections [47]. There is one final important difference to note between IXS and INS. Due to the properties of x-ray optics the resolution function from IXS is Lorentzian in nature (on a neutron instrument they are normally Gaussian). This can make extracting phonon widths (which are also Lorentzian in nature) rather challenging.

2.4 Other techniques

None of the techniques contained within this section have been used by the author, however it is important to recap several key points to aid the interpretation of data later on and put other results in a broader context.

2.4.1 Crystal Growth

While powders can be studied with inelastic techniques the most complete information is obtained by measuring single crystals. Thus you can probe all of $\vec{Q}$ rather than just $|Q|$. The samples measured in this thesis have been grown by the "optical floating zone" method. In this system a powder of the sample is prepared and then compressed into a long thin cylinder. The cylinder is then placed in a controlled atmosphere and light from 4 halogen lamps focussed onto a narrow zone.

Over many hours the melt is moved up the sample while the two components are counter-rotated to improve homogeneity. In an ideal situation the entire melt would emerge as a single crystal though this is very uncommon, so single crystals need to be cleaved out from the growth [48].

2.4.2 Physical Properties

Physical properties discussed in this thesis which have not been obtained from the literature were taken on a Quantum Design Physical Properties Measurement System (PPMS). The PPMS is a highly flexible piece of kit able to take resistivity, magnetometry, heat capacity and thermal transport (seebeck, resistivity and thermal conductivity are obtainable on the same set-up). The PPMS at Royal Holloway is equipped with a 9 T magnet and can cover the temperature range from 2-300 K. It is theoretically possible to go to 400 K however the system behaves very poorly above 350 K.

The thermal transport option is the most relevant here. A typical measurement set-up is shown in figure 2.14. For a measurement of the thermal conductivity the heater is turned on for a short (user defined) period and then after being turned off the evolution of temperature at the two thermometers is measured. The software fits a known line-shape to this and from these fit parameters the thermal conductivity can be discerned (once the user has supplied the sample dimensions). Corrections can be applied for heat loss due to radiation. Seebeck measurements are very similar only here it is the voltage generated by the temperature differential which is of interest.

2.4.3 Raman Scattering

In the previous section we saw that although it is possible to use electromagnetic radiation to measure momentum-resolved dispersions, in the case of x-rays, the

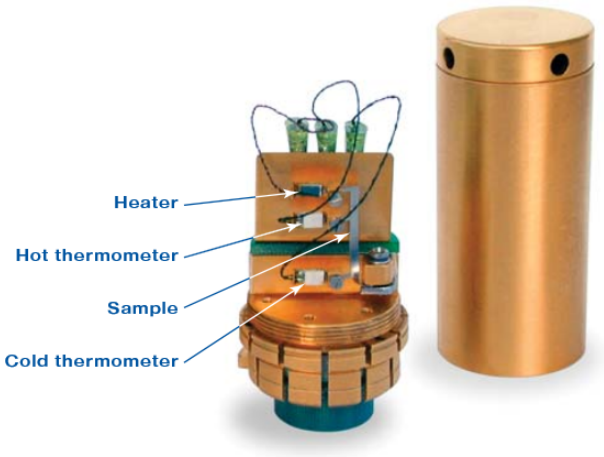

Figure 2.14: The PPMS thermal transport option with a standard sample mounted. Image reproduced from reference [49].

energy scale is very mismatched. We could instead use light of a much lower energy, more comparable to the phonon energy, but here the wavelength of the light is very mismatched and for a typical excitation the accessible wavevector is essentially only $\vec{Q} = 0$. This is often perfectly reasonable for an initial study of the vibrations within a structure (and is much cheaper than a neutron or inelastic x-ray measurement) and the technique is known as Raman scattering.

Only a subset of phonons will be able to scatter light inelastically and to understand why, it is useful to consider elastic (or Rayleigh) scattering. Here, an incident photon excites the electron cloud by polarising it and when the cloud de-excites the photon is remitted in an arbitrary direction [36]. The light has to polarise the electron cloud to interact with it and thus for a photon to scatter inelastically from a phonon, the phonon must cause a change in the polarisation of the material. Modes which can scatter light inelastically are known as "Raman active" and the active modes are defined by the symmetries of the system [39]. A general (if imprecise) picture is that, if a mode causes a significant change in the overall bond lengths it will be Raman active (as the polarisability of the system is related to the bond

lengths) and if not it is Raman inactive. Such a case could occur when a vibration has one atom elongating a bond and another shortening it by the same amount.

Chapter 3

Density Functional Theory

In the previous chapter a very simple ball and spring model was used to show the nature of phonons in a monoatomic chain. This model could conceivably be generalised and used in 3 dimensions. We would like, however, to consider systems which have large complicated cells. For such a system the simple ball and spring approach becomes impractical. Furthermore, to make predictions about the dynamics of a system the force constants of the springs must be known and they can only be guessed with the tools introduced so far.

It should be possible to calculate the properties of a system from the Schrödinger equation. The Hamiltonian for a real system consisting of N_n nuclei (which can of course be different species) and N_e electrons is

$$\hat{H} = -\frac{\hbar^2}{2m_e}\sum_i^{Ne}\nabla_i^2 + \frac{e^2}{4\pi\epsilon_0}\Bigg(-\sum_i^{N_e}\sum_k^{N_n}\frac{Z_k}{|\vec{r_i}-\vec{r_k}|}+ \\ +\frac{1}{2}\sum_i^{N_e}\sum_{j\neq i}^{N_e}\frac{1}{|\vec{r_i}-\vec{r_j}|}+\frac{1}{2}\sum_k^{N_n}\sum_{l\neq k}^{N_n}\frac{Z_kZ_l}{|\vec{r_k}-\vec{r_l}|}\Bigg),$$

where Z is the nuclear charge and $\vec{r}$ is the position vector of the particle. It is unfortunate that the complexity of this problem grows combinatorially with the

number of particles and in practice the problem quickly becomes intractable.

Rather than trying to solve the whole system simultaneously the problem could be broken down into manageable chunks which when taken together will approximate the true behaviour. There are two different principle methods by which this is attempted. The first was developed by Hartree and collaborators in the late 1920s [36]. This approach begins by assuming that the complex many-body wavefunction (Φ) can be obtained from

$$\Phi(\vec{r_1}, \vec{r_2}, ..., \vec{r_{N_e}}) = \prod_{i=1}^{N_e} \varphi_i(\vec{r_i}),$$

where φ is the one-electron orbital [50]. These one-electron orbitals are still subject to the various potentials of the Hamiltonian which remains a horribly complicated problem. Instead of considering the contribution of each electron a mean-field approach could be employed where a single effective potential is used to describe all the complex electron-electron and electron-nuclear interactions. Finding such a potential would be a great step forward, but to generate the effective potential the one-electron orbitals must be known and to find the one-electron orbitals, the effective potential is required. This can be resolved by seeking a "self-consistent" solution where the one-electron orbitals generated from an external potential will yield an almost identical, new external potential.

The procedure for finding the self-consistent solution is that initially the electronic contribution to the effective potential $V(\vec{r})$ is guessed (we do not need to guess the nuclear component as it is static). For electron i, $V(\vec{r})$ will take the form

$$V(\vec{r}) = V_{\text{ext}}(\vec{r}) + \int \frac{\sum_{j\neq i}^{N_e} |\varphi_j(\vec{r'})|^2}{|\vec{r} - \vec{r'}|},$$

where V_{ext} is a potential external to that of the electrons (here that from the nucleus

but it could also include a static external field) with the second term representing the Coulombic interaction between electrons [50]. φ_i is found for this $V(\vec{r})$ (by exploiting the variational principle) and used to generate one-particle Schrödinger equations from which a new $V(r)$ can be calculated. This procedure can be repeated until the difference between old and new $V(\vec{r})$ or $\Phi(\vec{r})$ has dropped below some pre-specified convergence criterion. In the above the electron spin has not been included, a shortcoming in the original approach of Hartree. The absence of spin means that the Pauli exclusion principle (which states that a system of several electrons must be antisymmetric with regards to particle exchange) cannot be enforced with anything other than $\Phi = 0$ leading to an incomplete description. The antisymmetry constraint was added by Fock who showed that it is satisfied with a many-electron wavefunction in the form of a Slater determinant [50]. These two elements combined give rise to the Hartree-Fock method which has been successfully applied to many systems.

Parallel to Hartree, Thomas and Fermi proposed that the solution to the many body problem lay in reformulating the problem in terms of the electron density. It is from this that the second approach called Density Functional Theory (DFT) has been developed. In this thesis DFT has been used to approximate the Schrödinger equation and calculate the vibrational properties of materials. Thomas-Fermi theory proposes that an inhomogeneous electron system can use the kinetic, exchange and correlation contributions from a homogeneous electron gas to calculate its total electronic energy (by assuming that the electronic density changes slowly and that at any point it is locally homogeneous) [51, 52]. The energy of this system ultimately depends upon only the electronic density and is thus termed a functional of the density. By looking for a density which minimises the total energy the ground state can be found. Although postulated in the 1930s DFT was initially much less developed than Hartree-Fock Theory as it lacked a proof.

3.1 The fundamentals of DFT

In 1964 Hohenburg and Kohn were able to show that an external potential can be determined entirely by the electron density (ρ) plus a trivial constant [53] proving the validity of DFT. This enables an expression for the energy to be written as

$$E[\rho] = T[\rho] + V_{ee}[\rho] + V_{ne}[\rho],$$

where $T[\rho]$ is the kintetic energy, $V_{ee}[\rho]$ describes the electron-electron interactions and $V_{ne}[\rho]$ is the external potential (which could be written more fully as $\int v(\vec{r})\rho(\vec{r})d\vec{r}$ where $v(\vec{r})$ is a potential defined by, for example, an atomic nucleus) [54]. Consequently they were able to show the existence of an electron density which will minimise the total energy and as demonstrated in Ref. [54] this leads to an expression of the form

$$\frac{\delta E[\rho]}{\delta \rho(\vec{r})} = v(\vec{r}) + \frac{\delta(T[\rho] + V_{ee}[\rho])}{\delta \rho(\vec{r})}.$$

Since $T[\rho]$ and $V_{ee}[\rho]$ do not explicitly depend upon $v(\vec{r})$ an expression for them would enable the ground state density to be determined. Interacting electrons must, however, be correlated preventing a simple description of the kinetic energy in terms of the electron density. A solution was proposed by Kohn and Sham [55] to replace the interacting electrons with a system of non-interacting particles. The Schrödinger equation for these non-interacting particles can be written as

$$\left(-\frac{\hbar^2}{2m} + V_{eff}(\vec{r})\right)\varphi_i(\vec{r}) = \epsilon_i \varphi_i(\vec{r}),$$

where m is the mass of the non-interacting particle, φ is the one particle orbital and V_{eff} is an effective external potential. This formulation is known as the Kohn-Sham

equation. The kinetic energy of the system can now be easily obtained as

$$T = -\frac{-\hbar^2}{2m}\sum_{i=1}^{\infty} f_i \langle\varphi_i|\nabla^2|\varphi_i\rangle,$$

with f_i the occupation of that orbital.

If a non-interacting particle density can be found which is the same as that of the interacting particle density then the kinetic energy contribution to the total energy can be calculated. This is not the kinetic energy of the interacting system as the electron-electron correlations have been lost but it allows another large component of the energy to be obtained. These correlations could be regained by a modification to V_{ee}. Thus the elements of $V_{ee}[\rho]$ can be written out and the electron contributions to the energy become

$$T[\rho] + V_{ee}[\rho] = T_S[\rho] + J[\rho] + E_{xc}[\rho],$$

with $T_S[\rho]$ the non-interacting kinetic energy, $J[\rho]$ a purely classical electronic repulsion term (known as the Hartree Energy) and $E_{xc}[\rho]$ containing the "difficult" exchange and correlation terms. It is thus known as the exchange and correlation energy. With this

$$\frac{\delta E[\rho]}{\delta\rho(\vec{r})} = v(\vec{r}) + \frac{\delta(T_S[\rho] + J[\rho] + E_{xc}[\rho])}{\delta\rho(\vec{r})},$$

$$\frac{\delta E[\rho]}{\delta\rho(\vec{r})} = v(\vec{r}) + \frac{\delta(T_S[\rho])}{\delta\rho(\vec{r})} + \frac{\delta(J[\rho])}{\delta\rho(\vec{r})} + \frac{\delta(E_{xc}[\rho])}{\delta\rho(\vec{r})}.$$

The one particle orbitals can now be used to calculate the density and consequently the kinetic energy. The Hartree energy takes the form

$$J[\rho] = \frac{1}{2}\int\int \frac{\rho(\vec{r})\rho(\vec{r'})}{|\vec{r} - \vec{r'}|} d\vec{r} d\vec{r'},$$

with

$$\rho(\vec{r}) = \sum_i f_i |\varphi_i|^2,$$

and again can be calculated exactly from the one particle orbital densities and the unknowns are confined to the exchange and correlation term which is energetically the least significant [50]. If the form of the exchange and correlation is known then the above equation can be minimised by varying the one particle orbitals.

3.1.1 Exchange and correlation

Unfortunately the exact form of the exchange and correlation term is not known but a great many approaches have been developed to approximate it. Here they are discussed at a general level in order of increasing complexity. This is known as the "ladder of functionals" [56]. The work in this thesis does not go beyond the second rung of this ladder and consequently the higher rungs will only be briefly mentioned.

The first rung - the Local Density Approximation

Using the homogeneous electron gas to approximate the properties of an inhomogeneous material was one of the key elements in the original Thomas-Fermi theory. We could use this within the formulation of modern DFT and make the assumption that the electron density at any point is is locally homogeneous. This assumption would enable the unknown exchange and correlation energy to be obtained from the homogeneous electron gas results. An approach of this form is known as the local density approximation (LDA) and gives the energy as

$$E_{xc}^{LDA}[\rho] = \int \rho(\vec{r}) \epsilon_{xc}(\rho) d\vec{r},$$

and potential

$$\frac{\delta(E_{xc}^{\mathrm{LDA}}[\rho])}{\delta\rho(\vec{r})} = \epsilon_{xc}(\rho(\vec{r})) + \rho(\vec{r})\frac{\partial\epsilon_{xc}(\rho)}{\partial\rho},$$

with $\epsilon_{xc}(\rho)$ the exchange and correlation energy per electron in a uniform electron gas of density ρ [54]. $\epsilon_{xc}(\rho)$ can be obtained by a fit to Monte Carlo calculations of the homogeneous electron gas (normally those of Ceperly and Alder [57]).

Calculations performed using the LDA tend towards more homogeneous solutions than the real system [50]. This in turn leads to an over binding which for metallic, ionic or covalent systems still allows for a reasonable calculation of properties. In these tightly bound systems common errors include slightly shorter bond lengths, an overestimate of the cohesive energy and a slight tendency to underestimate elastic constants as well as phonon frquencies [58, 50] . In the case of weakly bound systems (such as hydrogen bonds) this over binding is a significant source of error.

LDA also has a problem with self interaction in the Hartree term. The self interaction error is caused by one part of the electron density repelling a different part of the same electron's density. In alternative methods such as Hartree-Fock there is also a self interaction component but it is exactly cancelled by an equivalent term in the exchange interaction. Within the LDA the self interaction error in E_{xc} is not equivalent to the error in the Hartree term and this incomplete cancellation of self interaction energy gives rise to an energy penalty for highly localised states erroneously favouring delocalised states. LDA also has issues with bandgaps in semiconductors and strongly correlated systems (such as V_2O_3). In semiconductors the LDA typically underestimates the band gap by around 40% [50] while in strongly correlated systems it typically predicts insulating systems to be metallic. The band gap issues have different origins which are discussed in detail in Ref. [50]. The first step in trying to improve the LDA might be to try and introduce semi-locally, inhomogeneities in the density.

The second rung - the Generalised Gradient Approximation

Rather than assuming a constant density we could consider an expansion of the density to include its gradient or even higher order terms. This expansion has been performed for as many as 6 terms in some theories [59]. However beyond the second order term there is a deal of uncertainty about the values of coefficients and thus in general the expansion is truncated at the second order term. This expansion is known as the Generalised Gradient Approximation (GGA). A great deal of care needs to be taken in the determination of the GGA's additional parameters as they can be obtained in many ways which can introduce errors in either the exchange or correlation. Within the GGA the exchange and correlation energy becomes

$$E_{xc}^{\mathrm{GGA}}[\rho] = \int A_{xc}[\rho]\rho(\vec{r})^{4/3}d\vec{r} + \int \frac{C_{xc}[\rho]|\nabla\rho(\vec{r})|^2}{\rho(\vec{r})^{4/3}},$$

where A_{xc} and C_{xc} are parameters to be determined.

There are two main groups of GGA, either parameter free where A_{xc} and C_{xc} are determined from exact theoretical conditions or empirical where these are determined by fitting experimental data or calculated properties [60]. The most common parameter free GGAs are those of Perdew-Wang from 1991 (PW91) [61] and Perdew, Burke and Ernzerhof (PBE) [62]. A common empirical GGA is that of Becke, Lee, Parr and Yang (BLYP)[63].

GGAs introduce a degree of non-locality and in general greatly improve the behaviour of weakly bonded systems leading to a marked increase in the accuracy of calculated cohesive energies over the LDA. A more detailed discussion of the improvement in cohesive energies is given in reference [58]. The GGA however retains several issues. Firstly, though an improvement over the LDA they do not fully deal with the non-locality of exchange. Secondly, in common with the LDA the self interaction error is not cancelled exactly [50].

The higher rungs

Several higher rungs exist, including Meta-GGA (third rung), Hyper-GGA (fourth) and the Generalized random phase approximation (fifth). These can use much more complicated functions of the density, the Hartree-Fock exchange term and more sophisticated ways of dealing with correlation the details of which are not relevant here [60].

3.1.2 Spin density functional theory

Within the LDA and GGA only a single electron density has been considered, implicitly assuming that the system is not spin-polarised. This is restrictive as many systems are spin polarised (for example ferromagnets), however, considering such a system turns out to be relatively simple. The details are described in Ref. [50] but in brief, two densities are used, one corresponding to spin up and the other spin down. A small modification to the exchange-correlation term is then included to describe this, whose magnitude depends on the magnetisation density.

3.1.3 DFT in practice

The elements to compute the total energy of a system are now all in place. Once a choice for the approach to exchange and correlation has been made the problem becomes one of finding one-particle wavefunctions that minimise the total energy. Finding these wavefunctions requires two decisions to be made. First a way to represent them must be chosen and second, will all of the electrons within the system be modelled?

This second question may be surprising but very often a significant fraction of the electrons within a system are irrelevant for the properties being investigated. After all, in many atoms the innermost electrons are not involved in the chemical bonding

and increase the cost of the calculation for no real increase in the overall accuracy. Depending on the problem being considered either all-electron or pseudopotentials can be used.

To model the one-particle orbitals a choice of basis set must be made. There are four broad categories of basis set. These are extended (the basis set covers all space, typically useful for condensed systems), localised (the basis set is centred somewhere perhaps at an atomic position, these are often used for molecular systems), mixed (a combination of the previous two) and augmented (the basis set includes atomic like wavefuctions around the nucleus, typically highly accurate but also highly complicated) [50].

In this thesis the CASTEP [64] DFT package has been used. This uses a plane-wave pseudopotential approach with plane-waves as an extended basis set and using pseudopotentials rather than considering all electrons.

3.2 The plane-wave pseudopotential approach as implemented in CASTEP

3.2.1 Bloch's theorem, reciprocal space and Brillouin zone sampling

A periodic lattice was introduced in the experimental section to facilitate calculations of a scattering experiment. Bloch's theorem states that an electron in an external periodic potential has the same probability of being found at a point $\vec{r}$ in any unit cell within the system [65] implying that a similar construction could be of use here. The crystal lattice in real space has a related lattice in reciprocal space with the reciprocal lattice vectors $\vec{a^*}$, $\vec{b^*}$ and $\vec{c^*}$. These three reciprocal lattice vectors define a volume in reciprocal space known as the first Brillouin zone (BZ).

A set of non-interacting particles in a one dimensional box of length a have wavefunctions which are solutions of the Kohn-Sham equation of the form $\phi_k(x) = e^{ikx}$, with the eigenvalues $\epsilon(k) = \hbar^2k^2/2m$. This parabolic relationship shows how the energy of a particle varies with wavevector. Each neighbouring BZ also contributes a parabola, but Bloch's theorem means only the components within the first BZ are needed to describe the total system. This is shown in figure 3.1. If an external potential is applied (which could be the effective potential containing the electron interaction terms of DFT) the main effect is to open energy gaps within the dispersion. These will occur only at particular points within the BZ depending on the nature of the external potential.

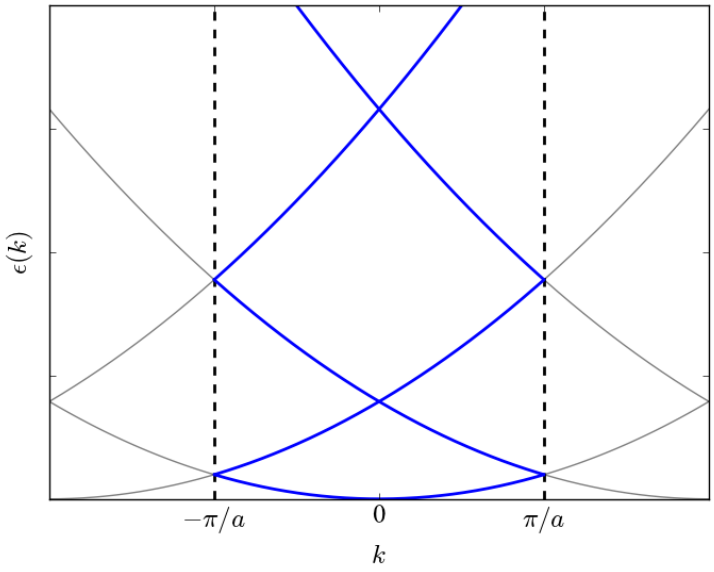

Figure 3.1: The energy bands of a non-interacting particle within a periodic crystal. Following Bloch's theorem only the first BZ is required to describe the behaviour of the whole system.

Since the wavefunction is periodic it could be represented as a Fourier series.

$$\phi_{\vec{k}}(\vec{r}) = e^{i\vec{k}\cdot\vec{r}} \sum_{\vec{G}} C_{\vec{k},\vec{G}} e^{i\vec{G}\cdot\vec{r}},$$

where $\vec{G}$ is a reciprocal lattice vector (which it must be to satisfy the periodic boundary conditions) and the summation is performed over all reciprocal lattice vectors, $C_{\vec{k},\vec{G}}$ is the coefficient of the Fourier series. Formally the density is obtained by integrating over all $\vec{k}$ within the first BZ but as nearby k-points carry similar information this can be approximated by a summation over a discrete set of $\vec{k}$ [50]

$$\rho(\vec{r}) = \int |\Psi_{\vec{k}}(\vec{r})|^2 d\vec{k} \approx \sum_{\vec{k}} A_{\vec{k}} |\Psi_{\vec{k}}(\vec{r})|^2,$$

where $A_{\vec{k}}$ is the weighting of that point such that $\sum_{\vec{k}} A_{\vec{k}} = 1$.

This concept of BZ sampling is very powerful and the points that are sampled are known as k-points. In general the sampling formalism of Monkhorst and Pack [66] is used to select the k-points. This uses a regularly spaced grid and by increasing the density of points within the grid the accuracy of the calculation will be increased. It is also worth noting that as the size of the real space cell increases the reciprocal lattice shrinks. Functionally this means that a cell twice the size (with no other changes) will need only half the number of k-points as the first BZ is shrunk. The symmetry of the system can also be used to reduce the total computational cost. In a system with 4-fold symmetry, one quadrant of the first BZ contains all the information required as the rotational symmetry can be used to generate the rest of the BZ. The symmetry reduced BZ is known as the irreducible wedge.

3.2.2 Plane-wave basis sets

Above, we introduced the concept of representing the one-particle orbitals as a Fourier series of plane-waves, independent at each k-point. To build up a complete description, all the Fourier coefficients (of which there are an infinite number) would need to be considered [67]. The Fourier coefficients, however, decrease with increasing $|\vec{G}|$ [67] and thus the summation can be truncated once enough terms have been

included to accurately describe the property being investigated. This truncation is related to the smallest possible spatial variation which can be sampled in real space of the one particle orbitals (a larger basis set allows smaller features to be represented). Since each system will have a different sized BZ it is not convenient to specify this in terms of actual G-vectors. Instead the cut-off is normally defined in terms of an energy (E_{cut}) such that

$$\frac{\hbar^2}{2m}|\vec{k}+\vec{G}|^2 < E_{\text{cut}}.$$

Once the coefficients $C_{\vec{G}}$ have been determined for each k-point and orbital, the ground state density is defined.

It has already been stated that by using pseudopotentials the total number of orbitals that need to be solved can be reduced. Another reason for wanting to replace the true nuclear potential is that at the nucleus the potential diverges. Plane waves are computationally efficient away from the nucleus where the external potential is relatively flat. Close to the nucleus the number of plane waves required grows rapidly, raising the cost of the calculation beyond practical limits for all but the simplest systems. For this reason it is beneficial to replace the nuclear potential with a smoother one.

3.2.3 Pseudopotentials

Modifications to atomic potentials to make them easier to describe with plane waves have existed since the 1930s [68]. In 1959 modern pseudopotential theory emerged [69] based on the separation of the atomic and electronic potential into two components. The first is an effective core, which has a number of electrons subsumed into it and the valence electrons which must behave exactly as they would in the all electron atom. Once the pseudopotential has been created, the core is the same every

time it is used, regardless of the chemical environment (this is known as the "frozen core" approximation [50]). The design, construction and testing of pseudopotentials is non-trivial, but one of the main decisions is which electrons will belong to the core and which to the valence states. In general the more states (working from the outside towards the centre) that are included, the more chemical environments the pseudopotential will be valid for, but it will also increase the cost. No pseudopotentials have been devised by the author and thus no more details about the construction of pseudopotentials are given. Instead, only a general overview of the differences between several common classes follows.

Most pseudopotentials are designed with transferability in mind. By this it is meant that a pseudopotential used in one chemical environment will give equivalently good results in another unrelated environment. For this reason pseudopotentials are not designed by fitting to experimental results (although early ones were [70]). While there are many specific varieties of pseudopotential (which are discussed in Ref. [50]) the two broad categories that we will consider for use with CASTEP are norm-conserving or ultrasoft. An example of these two constructions is shown in figure 3.2.

Norm-conserving pseudopotentials require that

$$\int_0^{r_c} |r\tilde{R}_{PS}(r)|^2 dr = \int_0^{r_c} |rR_{AE}(r)|^2 dr,$$

where R is the wavefunction (PS and AE denoting pseudo and all-electron respectively), r the radius from the nucleus and r_c the distance from the nucleus above which both wavefunctions must be the same [50].

With ultrasoft pseudopotentials this constraint is lifted allowing, in general, a smoother wavefunction reducing the cost of the calculation. This makes ultrasoft the pseudopotential of choice for a plane-wave calculation subject to certain important

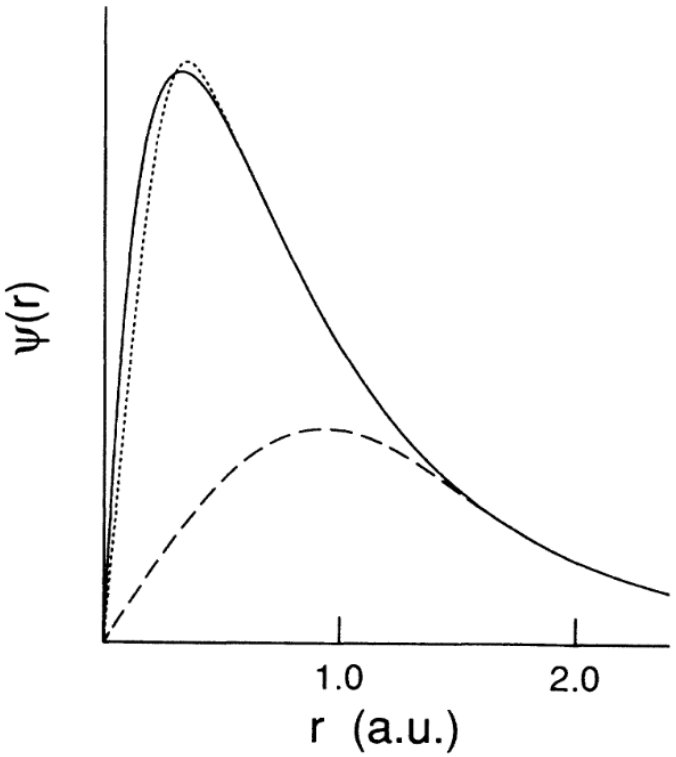

Figure 3.2: The oxygen $2p$ radial wavefunction reproduced from reference [71]. The true wave-function is shown as the solid line, with a norm-conserving pseudopotential as the dotted line and ultrasoft the dashed line. Note that above 1.5 a.u. the wavefunctions are the same.

limitations. The formalism for ultrasoft is much more complicated and for many properties calculations the problem becomes essentially intractable. To reduce the computational cost of the superstructures considered in this thesis only ultrasoft pseudopotentials have been used.

3.2.4 Electronic self-consistency

We are now in a position to attempt to find a density which minimises the total energy. The idea of electronic self-consistency was originally encountered while discussing the Hartree method and here again it can be used to obtain the ground

state density. Initially, the nuclear potential is specified, this could be used as the first guess for the total potential. However, a better approach is to use the potentials ($V_{ee} + V_{ne}$) of isolated atoms arranged according to the nuclear positions of the system. This defines the initial potential and the Kohn-Sham equation from which the initial φ_i is found (as a Fourier series) by minimising the total energy [67]. A new outgoing density is calculated and this becomes the new input density from which V_{eff} can be calculated. This procedure is repeated until the total energy changes are small enough for the answer to be considered self consistent.

There are various ways that this calculation can be influenced to reach the ground state more quickly. It is easy to imagine a case where the density oscillates between two distributions converging slowly towards an answer which is somewhere between them. A way around this is so-called density-mixing where a fraction of the old density is combined with the new. Density-mixing can be refined in several ways, the exact mixing ratio, how many steps back the density should be sampled at, as well as the specific mixing scheme the details of which are beyond the remit of this chapter. Density mixing has been used to improve the rate of convergence presented in the results chapters. As it simply improves the efficiency and is not important for the final result no details of the specific methods will be mentioned. Instead of mixing it is also possible to use Ensemble Density-Functional Theory (EDFT) to find the minimum [50, 72]. This is often slower than density-mixing but will always find a minimum and in very challenging systems it can provide a speed increase.

Metallic systems, which are characterised by bands crossing the Fermi level and small energy scales for excitations into nearby states, present particular challenges to achieving self-consistency. Here relatively small changes in the electronic bands crossing to the Fermi level can lead to quite large changes in the total energy of the system. For this reason rather than using a sharp cut-off at the Fermi level it is normal to broaden the electron distribution by smearing the density according to

an artificial temperature. This smearing can take many forms with some common types being Gaussian or a Fermi-Dirac type distribution. Once smeared the system is much less sensitive to small changes in the Fermi level which can greatly improve the speed with which a self-consistent solution can be found. The smearing width should, however, be carefully checked as it can introduce changes in the calculated properties [60].

3.2.5 DFT+U

The LDA and GGA give good agreement with a great many different systems and properties and are consequently widely used. Despite this there are some systems where the lack of cancellation of the self interaction error gives a completely incorrect ground state. The exact size of this error depends upon the specifics of the system being considered but it is a particular problem for systems with strong electron correlations, such as transition metals and rare earth elements. A prime example of this problem is the case of Mott insulators such as NiO where LDA and GGA (which are mean-field type approaches) give the same electronic charge on each Ni ion and a metallic ground state whereas experimentally there are two different Ni sites with different electronic charge states and an insulating ground state.

There are complicated approaches which attempt to improve on this self interaction error such as DFT+ Dynamical Mean Field Theory but they are computationally much more expensive than the traditional DFT approach [73]. Another computationally easier approach is to supplement DFT with a model Hamiltonian. In DFT+U this makes use of a correction inspired by the Hubbard model.

DFT+U begins by treating the entire system within the standard formalism of either GGA or LDA, then a subset of states which at the beginning of the calculation have been associated with a d or f orbital (normally) have the Hubbard-like correction applied to them. At this point we have double counted the uncorrected

energies and need to subtract out their original uncorrected values. This can be expressed mathematically as

$$E_{\mathrm{DFT+U}}[\rho(r)] = E_{\mathrm{DFT}}[\rho(r)] + E_{\mathrm{U}}[\rho_{d,f}(r)] - E_{\mathrm{dc}}[\rho_{d,f}(r)],$$

where E_{DFT} is the original LDA or GGA energy, E_{U} is the energy modified by the Hubbard type Hamiltonian and E_{dc} is the original LDA or GGA energy of the orbitals. The formal definition of E_{U} requires a summation over the different angular momentum operators and spin state and consequently a DFT+U calculation must always be spin polarised. Identification of the orbitals corresponding to d or f states is performed through a projection of the orbitals onto a localised basis set [73]. The parameter of note for these calculations is the Hubbard U which is defined in the Hubbard Hamiltonian as

$$\hat{H} = -t \sum_{\langle ij \rangle} a^{+}_{i\sigma} a_{j\sigma} + U \sum_{i \neq j} \hat{n}_{i\uparrow} \hat{n}_{j\downarrow}.$$

$-t \sum_{\langle ij \rangle} a^{+}_{i\sigma} a_{j\sigma}$ corresponds to $E_{\mathrm{DFT}}[\rho(r)]$. The value for U must be specified by the user as an energy but this means that the problem is no longer fully ab-initio. Typically U will be between 2 and 5 eV depending on how severe the self-interaction error is in the system under consideration and there is no universal value for a particular element. U can be calculated using a package such as Quantum Espresso [74] or where this has already been done for the system under consideration it can be taken from the literature. Great care must be taken with the use of DFT+U because, as already mentioned, it is no longer an ab-initio technique and the results must be checked to prove they are robust. When used correctly DFT+U can allow for the self-interaction error to be corrected for a comparatively small computational cost.

3.3 Calculation of Properties

3.3.1 Single-point energy and convergence

Before a material's properties can be calculated choices for the k-points and plane-wave cut-off as described above must be made. The general procedure for choosing these parameters is to converge them. By this it is meant that a series of calculations are performed where each parameter is varied systematically to ascertain the computationally cheapest setting that will still allow for reliable conclusions to be made about the property of interest.

The total energy of the system is variational with respect to plane-wave cut-off (i.e. the total energy will drop as the cut-off is increased). This variational behaviour is occasionally violated in certain complicated magnetic systems when the higher frequency terms change the stability of the magnetic structure. This is rare but was seen in one of the FeSe systems discussed in this thesis. If a system behaves variationally then it is possible to fit a standard curve to this (which has a logarithmic dependence on E_{cut}) and extrapolate to infinity thus correcting for the finite size of the basis set.

BZ sampling is not variational. Instead as the density of sampling within the BZ is increased, the total energy will oscillate about its true value with the total size of the oscillations decaying as the sampling density is increased. This sampling density should be converged along each non-symmetric direction (i.e. in a cubic system a grid of $n \times n \times n$ could be used while an orthorhombic system would use $n \times m \times l$). If the system is metallic the smearing width should also be converged as it can affect the final result.

The one-particle orbitals are, as already discussed, computed in reciprocal space but quantities such as the Hartree energy are defined in real space. This necessitates

converting between real and reciprocal space which can be done by means of a Fourier transform with the real space electron density represented on a grid. However, as previously mentioned the size of features probed is related to the plane-wave cut-off and thus the size of the real space grid is defined in terms of the largest $|\vec{G}|$. It is not simply a 1 to 1 conversion though, as $G_{\max}$ is related to the one particle orbitals not the electron density and due to the properties of Fourier transforms this makes the real space grid twice the size that would be expected from just $G_{\max}$. In reality it is often possible to use a grid scale smaller than 2 (by default CASTEP uses 1.75) as the errors introduced will for many properties not be large but it is important to check this. A grid scale greater than two will, however, only increase the memory requirements of the calculation and not the accuracy.

There is one particular case where a grid scale greater than two is required. When using ultrasoft pseudopotentials an additional static electron density is added to the core region to represent the density lost in softening the wavefunctions. This "augmentation charge" would require a much larger $|G_{\max}|$ to describe (this was, of course, the point in the ultrasoft formalism) but we do not want to use a finer grid everywhere as outside of the core it will add no information. For this reason CASTEP also has a fine grid which by default is the same as the standard grid but which can be increased independently and its value will depend on the pseudopotential used. This enables the augmentation charge to be accurately included regardless of the pseudopotentials specific position relative to the standard grid preventing spurious forces or jumps in energy if the pseudopotential moves in real space as part of a properties calculation. The fine grid especially requires convergence testing.

Once all these parameters have been specified and checked, a total energy calculation could be performed with a known level of uncertainty. This can be useful if the energetics of different structures are to be compared but very often more than just the total energy of the system is required. A calculation of the total energy is

often just the first step towards the calculation of a material's properties.

3.3.2 Band Structures

Once the self-consistent solution has been found the electronic density is completely specified. The electronic band structure below the Fermi level can then be obtained from the Kohn-Sham equation as for each orbital at a given k-point its corresponding energy is simply the eigenstate ϵ. Above the Fermi level the Kohn-Sham orbitals are often a reasonable first approximation for the electronic excitations although formally they are have no meaning within Kohn-Sham theory. Bands above the Fermi level also suffer from the previously mentioned band-gap problem and issues in strongly-correlated systems.

From the self consistent density the one-particle orbitals can be obtained at arbitrary $\vec{k}$ within the BZ. It is important to note that these are not self-consistent solutions as, while the density has been obtained self-consistently, at other points this self consistent procedure is not repeated. However, if a suitably accurate set of initial sampling points has been used this answer will not deviate from a self-consistent solution significantly.

3.3.3 Geometry Optimisation

The force acting upon a particle is related to the negative first differential of its energy with respect to position. The force on an atom could be calculated by displacing the nucleus a small amount, then recalculating the total energy and calculating the gradient. This would be moderately expensive and can be entirely avoided by implementing the Hellmann-Feynman theorem [75, 76]. This theorem states that

$$\frac{\partial E}{\partial a} = \frac{\partial}{\partial a} \int d\vec{r} \psi^* \hat{H} \psi = \int d\vec{r} \psi^* \frac{\partial \hat{H}}{\partial a} \psi,$$

where a is an infinitesimal displacement. This shows that once the electron density is obtained it is comparatively trivial to compute the forces. Thus for any single point energy calculation it is possible to calculate the forces on the atoms in the cell as a post-processing step. Once the force has been calculated, an attempt at minimising it can be made by displacing the atomic nuclei based on the forces acting upon them. This is the core principle of a geometry optimisation where a quasi-Newtonian method is used to find the minimum energy geometry [77] (this is named after Broyden-Fletcher-Goldfarb-Shannon and henceforth referred to as the BFGS method). Each step consists of a displacement whose size depends on an estimation of the bonding between atoms (expressed in terms of an average phonon frequency) and the magnitude of the force. The direction of the displacement is defined by the direction of the force subject to any applied symmetry constraints. The electronic ground state for this new structure is computed using the previous electron density as the starting configuration to reduce costs (as hopefully each step is a small change). The forces are then re-analysed and if the force remains in the same direction but is still non-zero a second step is made assuming a linear dependence. If the new force points antiparallel to the original force, the second step will lie between the start and first point (again assuming a linear dependence). If the new force is not parallel or antiparallel then the process will begin anew. This continues until the force drops below some user defined tolerance.

It is also possible to calculate the stress on a cell and thus optimise the cell parameters at any external pressure desired by the user. This is discussed in more detail in Ref. [67]. There are several considerations to be aware of if a variable cell type calculation is performed. The most important is that if the size of the cell is varying then so will the size of the reciprocal lattice and thus the number of plane waves in the calculation. This change in the number of plane waves introduces fictitious stresses called Pulay stresses [50]. These can be compensated by correcting

for the finite size of the basis set. This correction can be calculated at the beginning of a run by varying the plane-wave cut-off and fitting a logarithmic curve to the total energy. The curve does not need to be recalculated at each step. Both forces and stresses should be converged with respect to all the parameters previously described. When a geometry optimisation is performed it is important that the initial convergence tests look at the forces and stresses rather than simply the ground state energy.

3.3.4 Lattice dynamics

The generalised form

We have already calculated the expected excitation spectrum for a 1D monatomic chain. To allow the investigation of more complicated systems (preferably 3D with many atoms in the cell) within DFT, a generalised method is required. Here the methodology and notation of Ref. [39] is followed. As before the energy of the j^{th} atom is

$$E_j = \frac{1}{2}\sum_{n,j'} J_{j,j',n}(u_{j,0} - u_{j',n})^2,$$

where j is an atom in a reference unit cell, j' is all atoms in the cell n ($n = 0$ being the reference cell which is included in the summation). The force is thus

$$F_j = -\frac{\partial E_j}{\partial u_{j,0}} = -\sum_{n,j'} J_{j,j',n}(u_{j,0} - u_{j',n}) = m_j \frac{\partial^2 u_{j,0}}{\partial t^2},$$

where m_j is the mass of the j^{th} atom.

All the possible modes must be considered in any solution. For every atom in the cell there are 3 possible modes corresponding to displacements along x, y and

z. A solution to this is of the form

$$u_{j,n} = \sum_{\nu} A_\nu m_j^{-1/2} e_{j,\nu} e^{i(\vec{k}\cdot\vec{r}-\omega_\nu t)},$$

where ν is the mode label, A_ν is a scaling parameter and $e_{j,\nu}$ contains information about the relative atomic displacements and is normalised such that $\sum_j |e_{j,\nu}|^2 = 1$. Substituting this into the force equation would enable its solution to be found. This new equation would, however, get cumbersome quite quickly and it is better expressed in matrix notation such that

$$\mathbf{e}_\nu \omega_\nu^2 = \mathbf{D} \times \mathbf{e},$$

with $\mathbf{e}_\nu$ a vector containing all $e_{j,\nu}$ at a particular ν. $\mathbf{e}$ is the individual $\mathbf{e}_\nu$ matrices packed together into a square matrix and $\mathbf{D}$ is the dynamical matrix with the elements

$$D_{j,j'} = m_j m_{j'}^{-1/2} \sum_n J_{j,j',n} \left(\delta_{j,j'} - e^{(i\vec{k}\cdot\vec{R_n})}\right).$$

We could specify another matrix Ω which has the components $\Omega_{\nu,\nu'} = \omega_\nu^2 \delta_{\nu,\nu'}$ which would allow

$$\Omega = \mathbf{e}^{-1} \times \mathbf{D} \times \mathbf{e}.$$

This is now an eigenproblem with Ω the eigenvalues and $\mathbf{e}$ the eigenvectors of $\mathbf{D}$. Now only the force constants $J_{j,j',n}$ must be specified and then Ω and $\mathbf{e}$ can be found.

Calculating the force constants

To build up the force constants (which we can represent as a matrix and thus as defined above will be referred to as J) more than just the single point forces are

required. The response of every atom within the system to every other atom's displacement must be known. Due to the translational symmetry of the system only the displacements within a unit cell should be considered and furthermore the symmetry operators can be used to reduce the number of displacements required. This is still problematic as formally the response of every other atom within the system is needed. However, J decays quite quickly with $|\vec{r}|$ and practically can be considered zero for distances greater than $\sim 5-6$ Å.

Within a plane-wave code a periodic cell must be used, but the displacements required to build up J will also be repeated in the neighbouring cell which can lead to a problem of self-interaction. Consequently cells of at least 10-12 Åin x, y and z must be used. Each unique atom is then displaced a small amount in positive and negative x (then y and z) and the forces induced on the other atoms computed. The assumption is made that all the forces are harmonic which, while not true is generally a reasonable assumption and makes the calculation much cheaper. Thus $\mathbf{D}$ for the supercell at $\vec{k}=0$ is built up as (for the x component only)

$$D_{j,j',x} = \frac{F_{j'}^{+} - F_{j'}^{-}}{2\Delta x},$$

where atom j has been displaced by Δx along the Cartesian x direction and F denotes the resultant force on atom j' for a displacement along either $+$ or $-$ x. It is important to point out at this juncture that this procedure only works if every displacement results in an excited state which requires an accurate geometry optimisation to be carried out before the phonon calculation is run.

We are also interested in the elements of $\mathbf{D}$ at $\vec{k} \neq 0$. So long as the cell used is large enough that interactions with periodic repetitions can be considered to be zero then the expression for $D_{j,j'}$ in terms of J can be used to calculate Ω and $\mathbf{e}$ at any arbitrary $\vec{k}$. These calculations at arbitrary $\vec{k}$ are inexpensive as the force constants

calculated for the supercell completely define the problem. Indeed we can even make simple mass substitutions as a post processing step to evaluate the effect that doping might have. This general methodology is known as the finite-displacement supercell method [78, 79].

Chapter 4

Rattling modes in sodium cobaltate

4.1 Background

As was discussed in the introduction the thermal conductivity of a thermoelectric is of key technological relevance. While nothing can be done to reduce the electronic thermal conductivity without similarly reducing the electrical conductivity much attention has been given to the reduction of the lattice thermal conductivity. Most work has focussed on reducing this by increasing phonon scattering rates. Structural disorder has been used successfully to this end. Nano-crystalline powders (with particle sizes of the order of 10 nm) [80] have been seen to reduce the lattice thermal conductivity by around 50% and lead to a corresponding increase in ZT. Nano-crystalline effects have also been seen in $AgSbTe_2$ where the system adopts a nanoscale superstructure (with significant disorder manifesting as diffuse scattering in neutron diffraction) [81] which leads to massive phonon scattering [82]. The problem is that structural disorder would also be expected to reduce the electronic conductivity as can be seen in impurity scattering in simple metals [65] (that this

is not seen in reference [80] is most interesting). This has led to a great deal of interest in anharmonic phonons and their interactions as this should lead to phonon scattering without reducing the electrical conductivity.

PbTe is a prime example of this. It has a relatively simple rock salt structure but a very low κ_{latt} which has been attributed to anharmonic coupling between the acoustic phonons and an optic mode associated with the development of ferroelectricity [83]. In complicated crystal systems with cage-like structures loosely bound guest atoms have been observed to reduce the thermal conductivity. This has been postulated to be due to anharmonic vibrations of the guest atom leading to the scattering of other phonon modes (particularly the acoustic modes) [84]. This concept has been refered to as the Phonon Glass Electron Crystal (PGEC) and has been tremendously successful in motivating the reduction the lattice thermal conductivity [85]. This chapter is concerned with the study of this PGEC.

4.1.1 The Phonon Glass Electron Crystal

The PGEC has been widely studied and we will now recap some of the key findings, both experimental and theoretical. This is a very large field with a great many results and only a brief overview can be offered here. More comprehensive overviews of the PGEC and indeed thermoelectrics in general can be found in the many review articles on the subject [11, 9, 86].

After the very earliest work which suggested that rattling guests could suppress thermal conductivity [84] in the skutterudites a more systematic study was made which showed that rather than κ being driven to a minimum at full occupation some vacancies would lower the thermal conductivity further [87]. This was attributed to the structural disorder scattering a larger spectrum of phonons. Early experimental work on the Ge clathrates found a remarkably low κ of less than 1 W/mK at room temperature for a range of guest ions approaching the so-called minimum thermal

conductivity (κ_{min}) for Eu and Sr guests [88]. The minimum thermal conductivity is computed by assuming acoustic phonon mean free paths the size of the interatomic spacing [89]. This system had fully occupied guest sites and thus introducing structural disorder should not be able to reduce the lattice thermal conductivity further in contradiction to the work on the skutterudites.

Molecular dynamics calculations with empirical potentials were used to further investigate the Ge clathrates. They found an order of magnitude decrease in κ from the introduction of cages and then another order of magnitude decrease when Sr guests were added. They attributed the first drop to the increased complexity of the cells and the second to resonant scattering by the guest atoms [90]. Nuclear resonant inelastic x-ray scattering (NRIXS) in the clathrate hydrides (with Kr as the guest) confirmed the existence of guest modes in this structure but did not make a systematic study of the phonon lifetimes [91]. Other NRIXS measurements on the skutterudites have found that the Eu guest atoms' vibrations are focussed at low energy [92] but that the cage dynamics were also important for reducing the thermal conductivity [93].

First principles calculations of the guest dynamics in the skutterudites found that there was a rattling type motion but that it was not significantly anharmonic [94]. This was confirmed by powder INS which found well defined phonon modes with no indication of the resonant scattering predicted by the PGEC. They also argued against the concept of a rattling guest as the guest vibrational intensities observed were modulated in $\vec{Q}$. This interpretation is rather strict however as only in the case of the guest being completely decoupled from the lattice would its intensity have no modulation with $\vec{Q}$.

In the skutterudite $CeRu_4Sb_{12}$ [95] and clathrate $Ba_8Ga_{16}Ge_{30}$ [96] the presence of a rattler was inferred from the presence of an avoided crossing. The avoided crossing is not a reliable indicator of a rattling type mode as it is not always ob-

served [97]. The INS measurements again failed to observe any significant phonon scattering. Instead it was suggested that the low propagation velocities of the guest vibrations reduced the thermal conductivity [95].

While there is no question that the concept of introducing guest atoms into cage-like structures has been hugely successful for reducing κ the actual mechanism does not seem to be supported by the body of the literature. While individually both momentum resolved spectroscopy and first-principles calculations are powerful each has limitations exploring these systems. Due to the complexity of the cells a proper understanding of the features observed with spectroscopy is challenging and first principles calculations remain to be properly validated [86]. Furthermore relations to experimental values of κ are often based around a Debye model which only considers the acoustic phonons, inadequate for complex systems [98] where the full dispersion must be considered.

Another material which has been suggested to have rattling type motion is $Na_{0.8}CoO_2$ [25]. This material has the advantage that $NaCoO_2$ is a reference system since it removes the possible rattling sites and cages while preserving the underlying layered structure allowing a proper investigation of the role of the rattling modes and their cages (if they can be shown to exist).

4.1.2 The structure of $Na_{0.8}CoO_2$

Sodium cobaltate has attracted much interest over the years for a variety of physical reasons. Its physical properties are controlled by the sodium concentration [1] and an early proposed phase diagram is shown in figure 4.1. The superconductivity at low concentrations when hydrated generated great excitement due to similarities to the cuprate superconductors [23] although with much lower superconducting transition temperatures. It was shown to have a moderate Seebeck co-efficient at around half filling [99]. This increases as more sodium is added to the system until it eventually

becomes insulating at full filling [100]. Much of the interest in the Seebeck co-efficient stemmed from its seeming origin in magnetic entropy [101, 102].

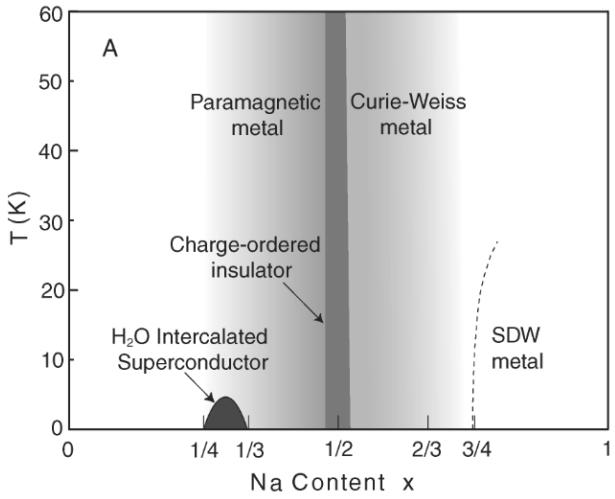

Figure 4.1: The phase diagram of Na_xCoO_2 reproduced from Ref [1].

Na_xCoO_2 has the space group $P6_3/mmc$ (Wyckoff:194) [23] and is made up of layers of Co with O octahedrally co-ordinated around them such that a single CoO_2 layer has ABC type stacking. Ignoring the positions of the Na ions momentarily the cell has two of these CoO_2 layers which stack in the order CABBAC (O-Co-O O-Co-O) as shown in figure 4.2. The Na layers sit between the two O layers. They cannot sit directly on top of the oxygen sites and will sit in either the vacant C site or in the slightly higher energy A sites (taking the oxygen B sites as the example). The convention used in this thesis is that $a = b = 2.85$ Åand $c = 10.8\mathring{A}$ (the lattice constants depend on sodium concentration, more details can be found in reference [3]) and $\alpha = \beta = 90°$ with $\gamma = 120°$. It should be noted that $NaCoO_2$ undergoes a structural phase transition to $R\bar{3}m$ which has 3 layers per cell but retains the same structure within a CoO_2 layer [100, 103].

These two different sodium sites correspond to the Wyckoff 2b (for the higher

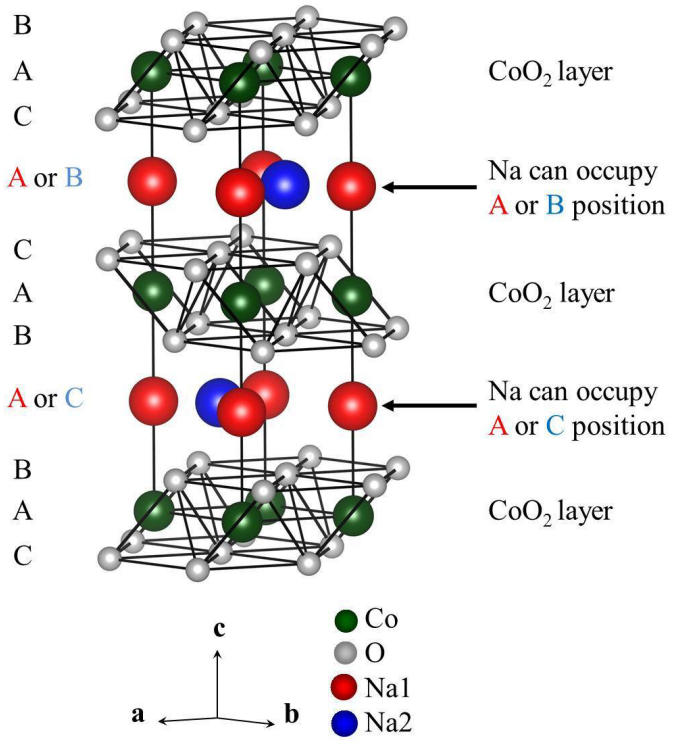

Figure 4.2: The crystal structure of $NaCoO_2$ with each crystallographic site labelled. Figure reproduced from the thesis of Dr D.G. Porter [2].

Atom	Fractional co-ordinates	Site
Co	(0,0,0)	2a
O	(1/3,2/3,0.098)	4f
Na1	(0,0,1/4)	2b
Na2	(2/3,1/3,1/4)	2d

Table 4.1: The Wyckoff positions of Na_xCoO_2.

energy site) and 2d crystallographic sites (the full list of Wyckoff positions are given in table 4.1). They are also referred to as the Na1 and Na2 sites respectively and this is the notation that will be used throughout this chapter. We might expect only the Na2 sites to be occupied as they are the lower energy positions however, experimentally a fraction of the Na1 sites are occupied [104]. This is interesting as the neighbouring Na1 and Na2 sites cannot both be occupied at the same time as

the inter-site distance is smaller than the Na^+ diameter [25]. In fact a kaleidoscope of different sodium superstructures has been predicted [25, 5] and observed [25, 105, 104, 106, 107, 108] across the entire sodium concentration range. A more detailed description of all of these different superstructures can be found in the thesis of M. Pandiyan [3].

The origin of the superlattices and partial occupation of Na1 sites lies in a consideration of vacancy energetics. This was considered by M. Roger. *et. al.* [25] with a Coulombic model. If the vacancies are considered as single negative charges then we would expect them to move as far apart as possible as shown in figure 4.3a. When two vacancies are neighbours we could also promote an Na2 into an Na1. While there is an energy cost to pay for doing this, there is a large gain from moving further away from the neighbouring Na2 sites. This turns out to be energetically more favourable for most levels of vacancy concentrations. This single Na1 site is known as a divacancy cluster. As the sodium concentration increases other types of multivacancy cluster become competitive. This is shown in figure 4.3b. The trivacancy cluster is the one which we shall further focus on for this chapter as it is the superstructure with the best thermoelectric properties (the quadrivacancy cluster has never been observed).

Roger. M. *et al.* showed that for $Na_{0.8}CoO_2$ the most favourable configuration was based around trivacancies arranged in an almost square pattern ($\gamma = 87°$) which for obvious reasons has become known as the square phase [25]. This phase has propagation vectors

$$\vec{a'} = \vec{a} + 3\vec{b}$$

$$\vec{b'} = 4\vec{a} - 3\vec{b}.$$

The structure of the square phase (minus the oxygen atoms) is shown in figure 4.4. The displacement in the Co layer is due to electrostatic repulsion of the Na1

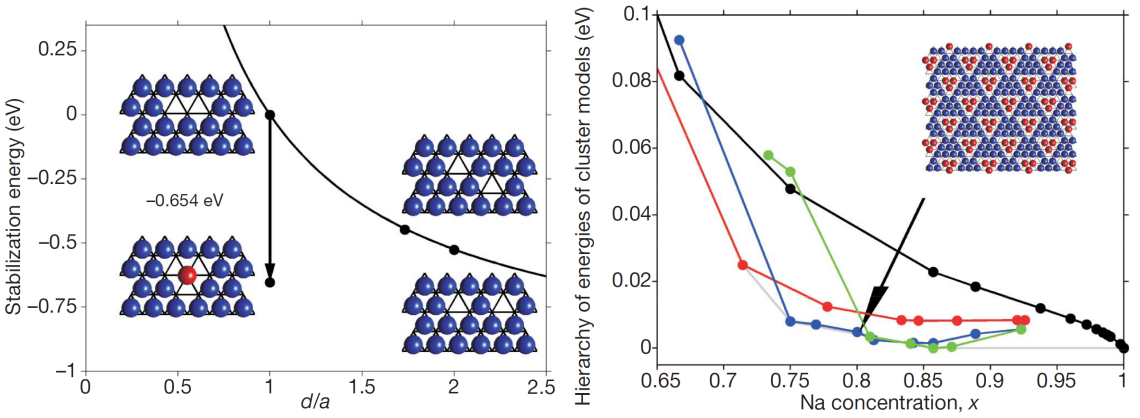

(a) (b)

Figure 4.3: Vacancy energetics in sodium cobaltate from reference [25]. (a) The energy of two vacancies for various distances. (b) The energetics of different multivacancy clusters with composition (red divacancy, blue trivacancy, green, quadrivacancy and black monovacancies). The inset shows the square phase superstructure.

sites which cannot deviate from the $z = 0.25$ positions by symmetry. This phase undergoes a structural phase transition at 283 K on heating (it is slightly hysteretic) into a partially disordered phase still consisting of trivacancies but now arranged in stripes. These trivacancies are perfectly ordered within the stripe but there is no correlation of the position of the trivacancy clusters between stripes. On cooling, this disordered stripe phase can either go into the square phase or (particularly if cooled quickly) enter into an ordered stripe phase where correlations between the stripes develop [105]. This ordered stripe phase has propagation vectors

$$\vec{a'} = 5\vec{a} + \vec{b}$$

$$\vec{b'} = 3\vec{b}.$$

Finally on heating further beyond 400 K the trivacancy clusters break down into a disordered array of multivacancy clusters [3]. These structures are shown in figure 4.5. There are many more superlattice peaks in the data than would be expected

with the stated superlattice vectors. The reason for this is that the superlattices break the underlying $P6_3/mmc$ symmetry. Thus differently oriented domains will form throughout the crystal (which can be obtained by applying the symmetry operators to the propagation vectors listed here) and all of these must be included to reproduce the total scattering.

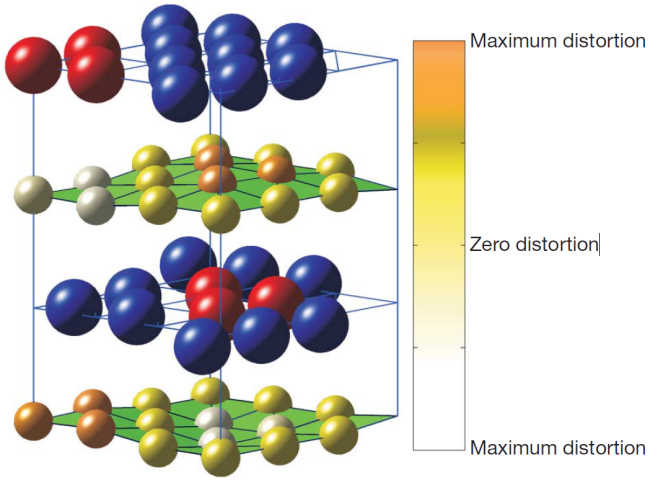

Figure 4.4: The square supercell with oxygen not plotted from reference [25]. The Co displacements have been vastly exaggerated so that they are visible.

Finally it is worth noting that at slightly lower concentrations ($Na_{0.77}CoO_2$) sodium cobaltate also forms a superstructure based on trivacancies which can be indexed on a $^1/_{13}$ grid. This system has a very large and complicated superstructure with 392 atoms in the supercell and partial disorder between the planes making it impractical to treat theoretically. Most samples of $Na_{0.8}CoO_2$ have some fraction of this present as a contaminant phase.

4.1.3 Previous Studies of the Lattice Dynamics of Na_xCoO_2

There have been several previous studies of the lattice dynamics in sodium cobaltate, however, most have chosen to focus on the electron-phonon coupling between the hydrated superconductor and the unhydrated system. Raman measurements at

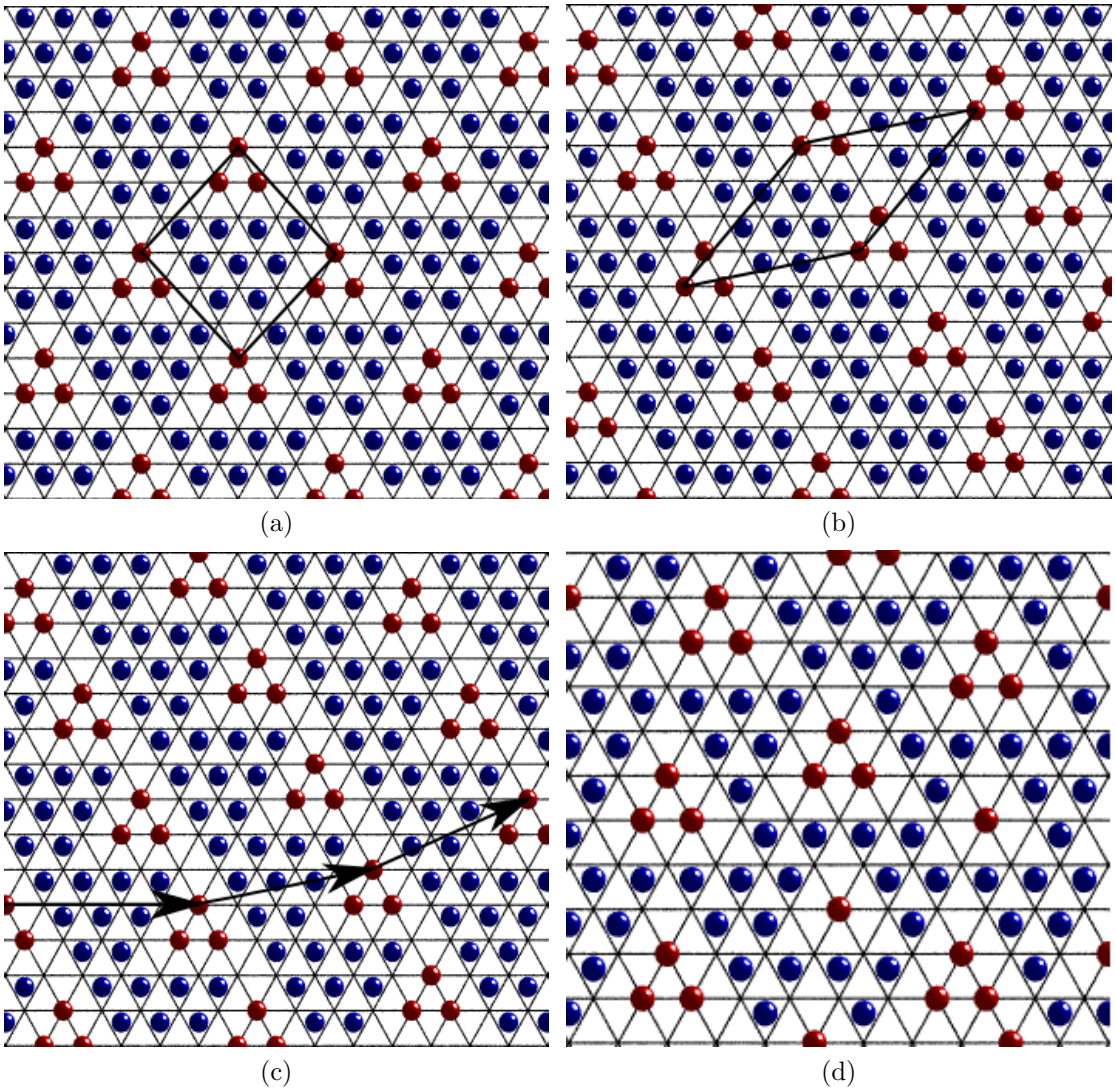

Figure 4.5: The in-plane structure of $Na_{0.8}CoO_2$. (a) The square phase, stable below 285 K. (b) The ordered stripe phase, meta stable below 285 K. (c) The disordered stripe phase which exists between 285 K and 370 K. (d) Disordered multivacancy clusters which are observed above 370 K.

higher x concentrations have identified up to 5 Raman active phonon modes for systems around $Na_{0.75}CoO_2$ [109] with the highest energy excitations at 83 meV. Other authors have found that care must be taken with these measurements as the sample surface rapidly degrades [110] or that this highest energy mode may be

from Co_3O_4 [111]. The authors of Ref [111] found that in hydrated samples the highest energy mode was at 70 meV, however, it is worth noting that $\vec{c}$ expands on H_2O intercalation [112] and that these high energy modes have been identified as O modes with vibrations perpendicular to the plane in first principles calculations [113]. The highest energy mode observed with infra-red was at 72 meV. In all these measurements little information can be extracted at low energies due to a lack of intensity and high background. This is the region where the Na vibrations dominate as shown by the changes observed in first principles lattice dynamics calculations when the Na1 site is occupied instead of the Na2 [100] which mostly occur below 30 meV. Another Raman study showed that anhydrous $Na_{0.7}CoO_2$ samples had much broader excitations than their superconducting counterparts, attributed to Na disorder or sublattices forming [114]. Again this could only be observed between 55 and 75 meV [114] where O vibrations dominate.

There have been some momentum-resolved spectroscopy studies of the dynamics in $Na_{0.75}CoO_2$. Boothroyd *et. al.* principally studied the magnetic dynamics with single crystal INS however they were able to observe some scattering from optic phonons at 20 meV [115]. Powder INS measurements were performed on $Na_{0.3}CoO_2$ but did not extend below 25 meV in energy transfer and thus cannot be compared to the other calculations or measurements [112]. The most extensive study of the lower energy dynamics was an IXS study in which the dispersions were mapped out along Γ-M. Clear modes were measured up to 75 meV with significant intensity in the region 10-30 meV in all scans not predicted by their first principles calculations [116].

4.2 Experimental procedure

To investigate these properties a number of experimental studies have been performed. Mostly these are inelastic but there have been a small number of elastic measurements to characterise samples.

4.2.1 X-Ray Measurements on Xcalibur

A small crystal of nominal growth composition $Na_{0.85}CoO_2$ was cleaved from the larger growth (dimensions $400 \times 400 \times 20$ μm) and screened on the Xcalibur x-ray diffractometer. It was found to be a single crystal principally in the disordered stripe phase as the $^1/_{13}{}^{th}$ peaks are very weak compared to the disordered stripe phase peaks indexed on a $^1/_5{}^{th}$ grid (as shown in Fig 4.6). An estimation of the relative concentrations was made by comparing the intensity of the (0.8, 0, 0) type peaks to the (1,0,0) peaks. Integrations across the entire peak were made using the 3D peak integration in CrysAlis^{Pro} (the software which comes bundled with Xcalibur) and averaged across all 6 of the symmetric peaks. This gave a relative ratio of intensities of $^1/_{74}$ compared to the calculated value of $^1/_{55}$ giving a disordered stripe phase concentration of 75%. After this measurement the sample was covered in a thin layer of silicone oil to prevent it reacting with the atmosphere.

4.2.2 Inelastic x-ray measurements on ID28

The sample measured on Xcalibur was then remounted on a 0.1mm diameter glass capillary and taken to the ESRF for an inelastic x-ray experiment on the beamline ID28. The beamline was aligned with the Si (9,9,9) reflection (incident energy 17.794 keV) on the backscattering monochromator (giving a nominal resolution of 3 meV). The toroidal focussing mirror was used to increase flux (slightly decreasing the $\vec{Q}$

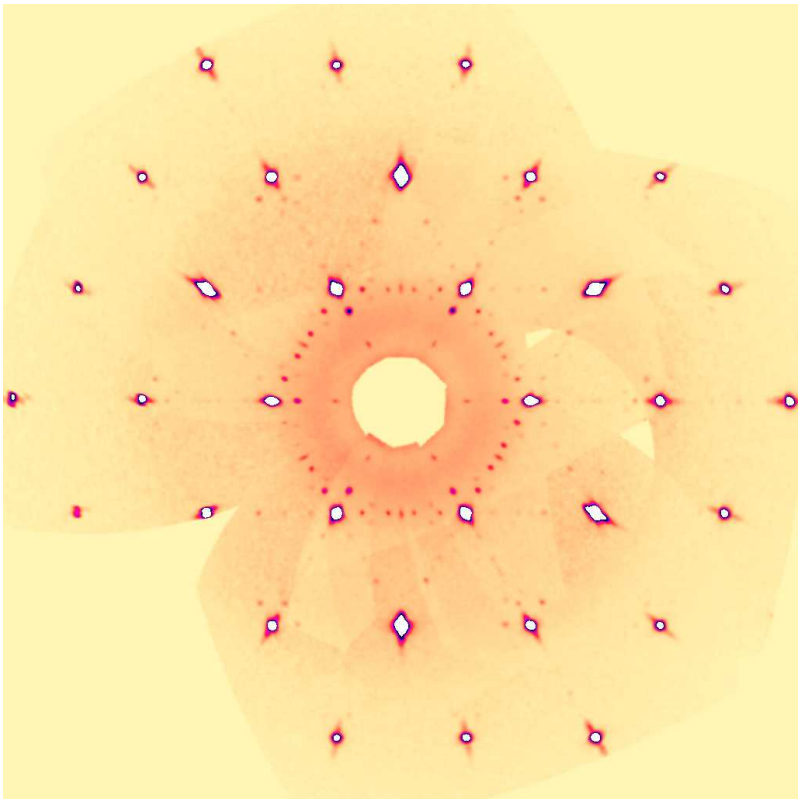

Figure 4.6: The (hk0) plane of the sample measured on ID28. $\vec{a^*}$ is horizontal and $-\vec{a^*}+2\vec{b^*}$ vertical. The secondary peaks which lie between the $(1,0,0)$ principal reflections (and form a 6-fold ring around them) are from the disordered stripe phase and the $^1/_{13}{}^{th}$ peaks lie just away from this direction forming a 12-fold ring around the principal reflections. However, their intensities are so small that they are barely visible on this scale.

resolution but given the poor mosaic of our crystal anyway this is comparatively unimportant). The sample was initially aligned in the $(h,0,l)$ orientation using the (1,0,0) and (0,0,4) and quickly cooled to 250 K before being more slowly cooled to 200 K using an Oxford Instruments cryostream. Energy scans from -20 to 90 meV in 0.68 meV steps were performed for fixed values of $\vec{Q}$ along the (1,0,0) direction starting at (1.07,0,0) and increasing in (0.1,0,0) steps until (1.47,0,0) (0.07 type positions were used to avoid possible contamination from stripe phase elastic superlattice reflections which lie along this direction). The sample was then re-

aligned with the (h, h, l) plane parallel to the horizontal scattering plane using the (1,1,0) and (0,0,4) reflections. Energy scans were again performed from -20 to 90 meV for selected values of $\vec{Q}$ from (1,1,1) to (1.5,1.5,1) and then the corresponding scans were made around the (1,1,2) allowing a large swathe of reciprocal space to be mapped out.

The sample was then warmed up and at 255 K a camera image of the diffraction was taken, shown in figure 4.7a. This shows that on cooling the sample went principally into the square phase rather than the stripe phase. The reason that the $^1/_{13}{}^{th}$ phase appears to be stronger here is that this camera does not take a cut through the $(h, k, 0)$ as it is a flat plate. Instead everywhere apart from the main (1,0,0) peaks is slightly off in l and this makes the $^1/_{13}{}^{th}$ rods appear stronger.

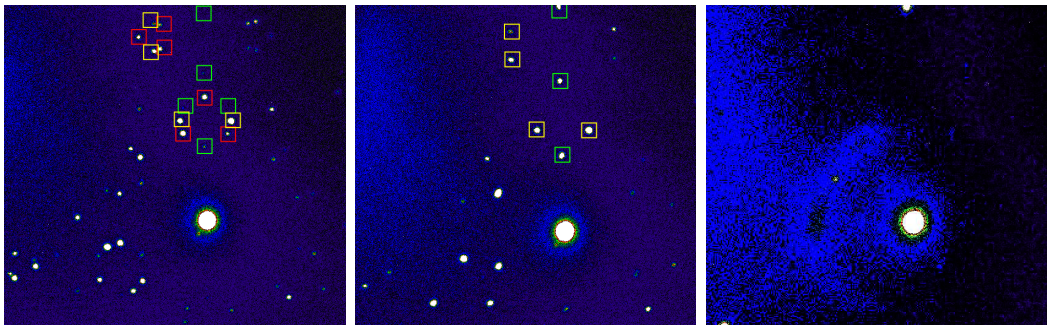

(a) (b) (c)

Figure 4.7: The three camera images obtained on ID28 at (a) 255 K, (b) 300 K and (c) 400 K. The peak positions have been marked with the coloured squares. At 255 K red shows the positions of the square phase, green the ordered stripe phase and yellow the $^1/_{13}{}^{th}$. At 300 K the green squares show the positions of the disordered stripe phase peaks. That they have disappeared on cooling shows that the sample has gone into the square phase. At the highest temperatures only a broad diffuse ring is visible.

At 300 K another camera image was taken showing the sample in the disordered stripe phase (shown in figure 4.7b). The sample was re-aligned and the scans around the (1,1,1) were repeated. Finally the sample was warmed to 400 K and another camera image was obtained showing diffuse scattering implying that it is in the

disordered multi-vacancy cluster phase with no long-range order. The measurements around the (1,1,1) were then repeated for a final time.

The datasets were initially extracted using the MATLAB script addIXS and then peak positions and widths were extracted by fitting the energy scans using the program fit28. Both addIXS and fit28 are available from ID28. The phonons were treated as Lorentzians which were then convolved with the instrumental resolution function measured for this set-up at the beginning of the cycle.

4.2.3 Inelastic Neutron Measurements on IN8

A large crystal ($35 \times 10 \times 3$ mm^3) with a mosaic spread of 3° (determined via a θ scan on IN8) which had been screened by Dr D.G. Porter on SXD at ISIS was placed in an aluminium can in an inert helium atmosphere and taken to IN8 at the ILL. Due to technical difficulties it was not possible to use the best resolution without collimation option of the Cu focussing monochromator/analyser and instead the pyrolytic graphite (0,0,2) monochromator and analysers were used with a high degree of collimation ($|k_f|$ was fixed at 2.662 $\AA$). This collimation was 30' between source and monochromator, 20' between monochromator and sample, 30' between sample and analyser and 30' between analyser and detector. This gave a FWHM of 0.77 meV for the elastic incoherent scattering from vanadium. A graphite filter was used to suppress higher order reflections.

Measurements were made on a strong, highly dispersive phonon mode at (1.01,1.01,1) which had been shown to have a width roughly in the middle of those measured on ID28. Energy scans from 20 to 4 meV in -0.2 meV steps (negative energy steps were used due to the backlash on IN8 associated with $2\theta_m$) were made at a number of temperatures (10, 50, 85, 120, 160, 200, 240 and 275 K) to determine the phonon lifetimes. The 10 K data was not used due to anomalous broadening as the temperature was lowered, possibly due to magnon contamination.

The collimation was then removed and the analyser/monochromators were changed to Si to improve the $\vec{Q}$ resolution (again $|k_f|$ =2.662 $\AA$). Energy scans were then made through the rattling mode position at (1.25,1.25,1). An unusual shaped background (identified as Al) was observed and thus the sample was rotated by 90° to suppress the rattling mode and obtain a measure of the background.

The peak fitting was performed using a Python script written by this author. The minimisation algorithms were supplied by Minuit from the Python wrapper PyMinuit [117]. The 50 K data was fitted by a Gaussian and this was used as the instrumental resolution. This resolution function was convolved with a Lorentzian and the width of this Lorentzian was used to calculate the phonon lifetimes. There is a small shoulder at higher energy which seemed to be temperature independent and, therefore, not phonon scattering from the sample.

4.2.4 Inelastic Measurements on MERLIN

Two different samples were measured on MERLIN. The first was a sample which had been observed to go into the stripe phase on cooling on SXD. The sample was aligned in (h, h, l) on the instrument ALF at ISIS. This was cooled to 200 K and the "sloppy" (by which it is meant that it has a relatively large acceptance angle) chopper placed into the beam. An incident energy of 50 meV was selected with a chopper frequency of 250 Hz giving a resolution of $\sim$ 3 meV at the elastic line. A 50° degree rotation of the sample (in 2° steps) was used to map out a large volume of reciprocal space.

The second sample consisted of two co-aligned (again on ALF) single crystals with a combined mass $\sim$ 4 times that of the previous. They went into the square phase on cooling and an identical region of reciprocal space to the original experiment was mapped out. In both experiments there was considerable scattering from Al which made up the cryostat. Due to the machining of the cryostat this was not

an isotropic powder and thus for the background subtractions several scans of the same length as the original were made over the same range but with a step size of 12°. The assumption that the background was the same over these arcs was made and the same scan was then used to represent the 2° steps originally measured. This measurement slightly overestimates the Al contribution as Co has a moderate neutron absorption cross section and removing the sample leads to an increased neutron flux on the sample holder and rear of the cryostat. The averaging procedure will also lead to errors in the intensity with angle. By looking at the Al line positions and comparing the magnitude of the remaining intensities with the unsubtracted intensities this overestimation can be seen to be around 5% as shown in figure 4.8.

4.2.5 Thermal Conductivity measurements with the PPMS

The thermal conductivity measurements were performed by Dr D.G. Porter on a sample cleaved from the same growth as the ID28 measurements. This sample measured $7 \times 2 \times 0.5$ mm with the short direction parallel to the crystallographic $\vec{c}$. Gold contacts were attached to the sample with silver epoxy resin and the in-plane thermal conductivity was measured from 2 to 300K.

4.3 Computational procedure

The calculations reported in this chapter have been performed by Professor K. Refson. For this reason there are no reports of convergence testing or discussions of why certain parameters have been used as this is the work of Professor Refson. Instead a brief summary of the computational details will be given to enable comparisons to the literature.

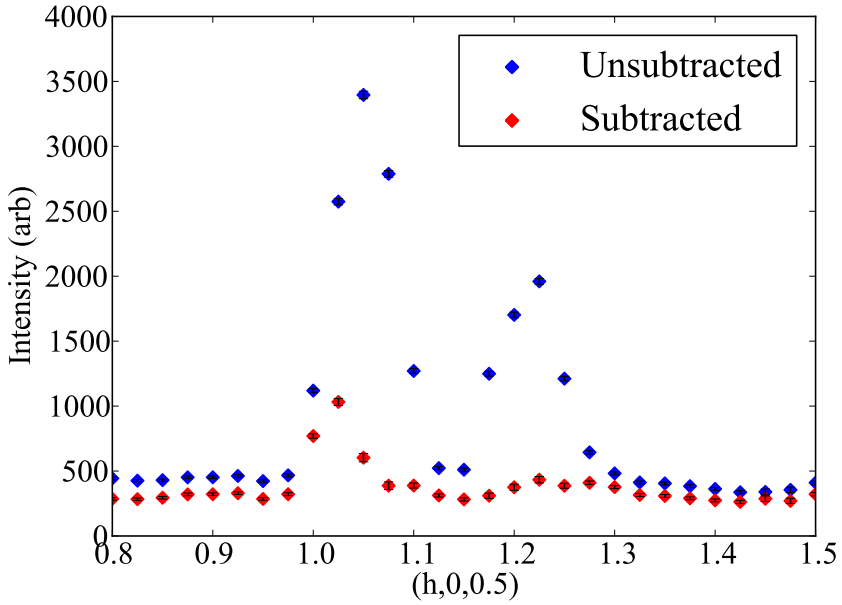

Figure 4.8: Data from MERLIN integrated from $0.45 \leq l \leq 0.55$ and $-0.05 \leq \eta \leq 0.05$ where η corresponds to $(-\eta/2, \eta, 0)$. The cut is in a $[h, 0, 0]$ direction with the axis labels in terms of the $\vec{a^*}$ of $Na_{0.8}CoO_2$. The two peaks in the unsubtracted data are the Al (1,1,1) and (2,0,0) respectively. The small peak that remains near the (1,1,1) in the subtracted data is probably a powder line corresponding to the (1,0,0) of sodium cobaltate. The background level of ~ 300 is due to the incoherent cross section of Co and Na (around 80 % Co). Looking at the remaining peak height of the (2,0,0), subtraction has removed around 95%.

4.3.1 The 8 Atom Cell

Calculations were initially performed on the 8 atom unit cell with symmetry $P6_3/mmc$. Custom pseudopotentials for sodium, cobalt and particularly oxygen were devised for this system while retaining a high degree of transferability between other transition metal oxides. These gave accurate agreement with all electron models at a plane-wave cut-off of 500 eV. The electronic Brillouin zone was found to be sampled adequately with a Monkhorst-Pack grid of $7 \times 7 \times 2$. $Na_{0.8}CoO_2$ was approximated by doping the 8 atom unit cell with an additional 0.4 holes. This drove the system metallic and a Gaussian smearing of electrons at the Fermi level was used with a

width of 0.1 eV to aid convergence. In both cases the density mixing technique was used with Pulay mixing. The fine grid scale was increased from 1.75 to 3.

For the phonon calculations the system was geometry optimised with fixed lattice parameters of $a = 2.85$ Åand $c = 10.811$ Å. This led to a total error in the forces of less than 0.002 eV Å^{-1}. The phonon calculations were performed using the finite displacement/supercell method with a supercell of $5 \times 5 \times 2$.

4.3.2 The square and stripe phases

The calculations for the square and striped phases were performed in a very similar manner. A k-point sampling grid of $4 \times 4 \times 4$ was used and, as both systems were metallic, Gaussian smearing with a width of 0.1 eV was used. For the phonon calculations the systems were geometry optimised such that the error in the forces was less than 0.0024 eV Å^{-1}. A single cell with parameters $a' = 10.276$ Åfor the square phase and $a' = 13.06$ Åfor the stripe phase was found to be sufficient for the supercell method.

4.4 Results

4.4.1 The Phonon Dispersion from ID28

200K

The scans made around (1,0,0) and (1,1,1) at 200 K allowed reciprocal space to be mapped out along both the high symmetry directions Γ-M and Γ-K-M. In addition the other detectors mapped out a significant volume of reciprocal space away from the high symmetry directions. The comparison between the measured positions, the 8 atom cell and square phase calculations are shown in figure 4.9 with the full dispersions shown in figure 4.10. It is clear from this that there is significant extra

intensity in the square phase calculation between 10 and 30 meV. This seems to be borne out experimentally with additional features observed in this region.

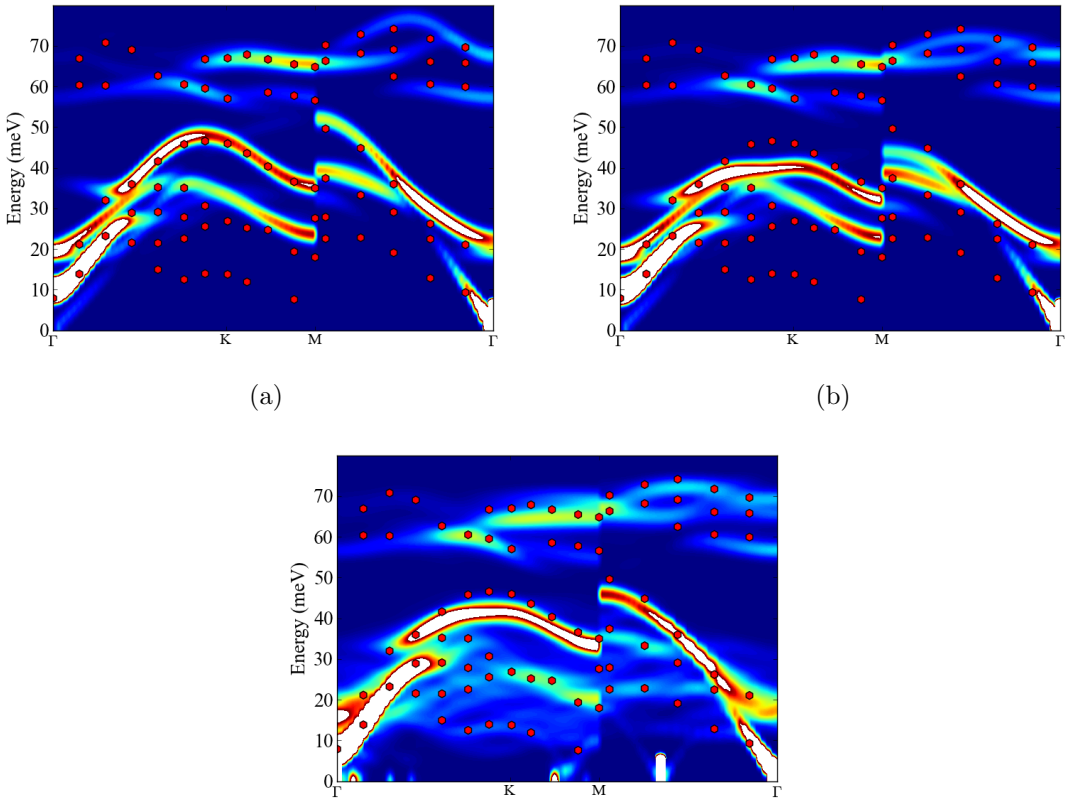

Figure 4.9: The computed phonon dispersions from (1,1,1) to (1.5,1.5,1) (Γ-K-M) and (1.5,0,0) to (1,0,0) (M-Γ) for the 8 atom cell (a), the 8 atom cell doped with 0.2 holes per formula unit (b) and square phase (c). The red hexagons indicate where it was possible to fit individual modes in the ID28 data.

For a more detailed comparison between the two models it is necessary to look at the individual energy scans. A representative sample of these from the high symmetry directions and off axis detectors is shown in figure 4.11. The agreement here between experiment and calculation is remarkable, indeed the only real disagreement is observed in the strong mode around 40 meV across the K point. This corresponds

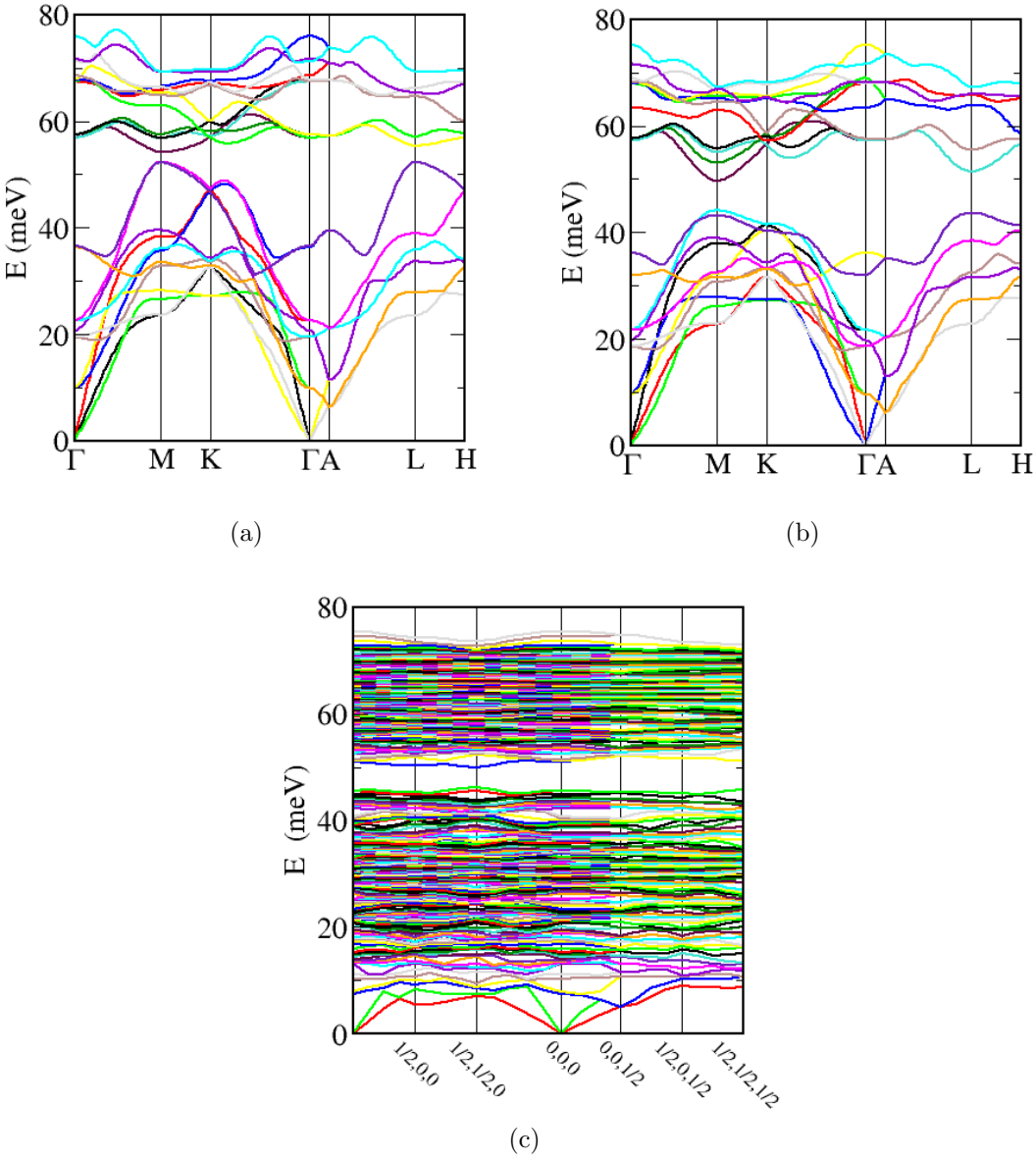

Figure 4.10: The computed phonon dispersions from around their respective irreducible wedges for the 8 atom cell (a), the 8 atom cell doped with 0.2 holes per formula unit (b) and square phase (c).

to a collective motion of the Co-O planes moving towards each other and any errors due to the localisation of charge on the Co sites is likely to be amplified in such a

mode. In all of these scans there is significant scattering below 30 meV which, apart from intense and highly dispersive modes near Γ are not predicted by the 8 atom cell calculations.

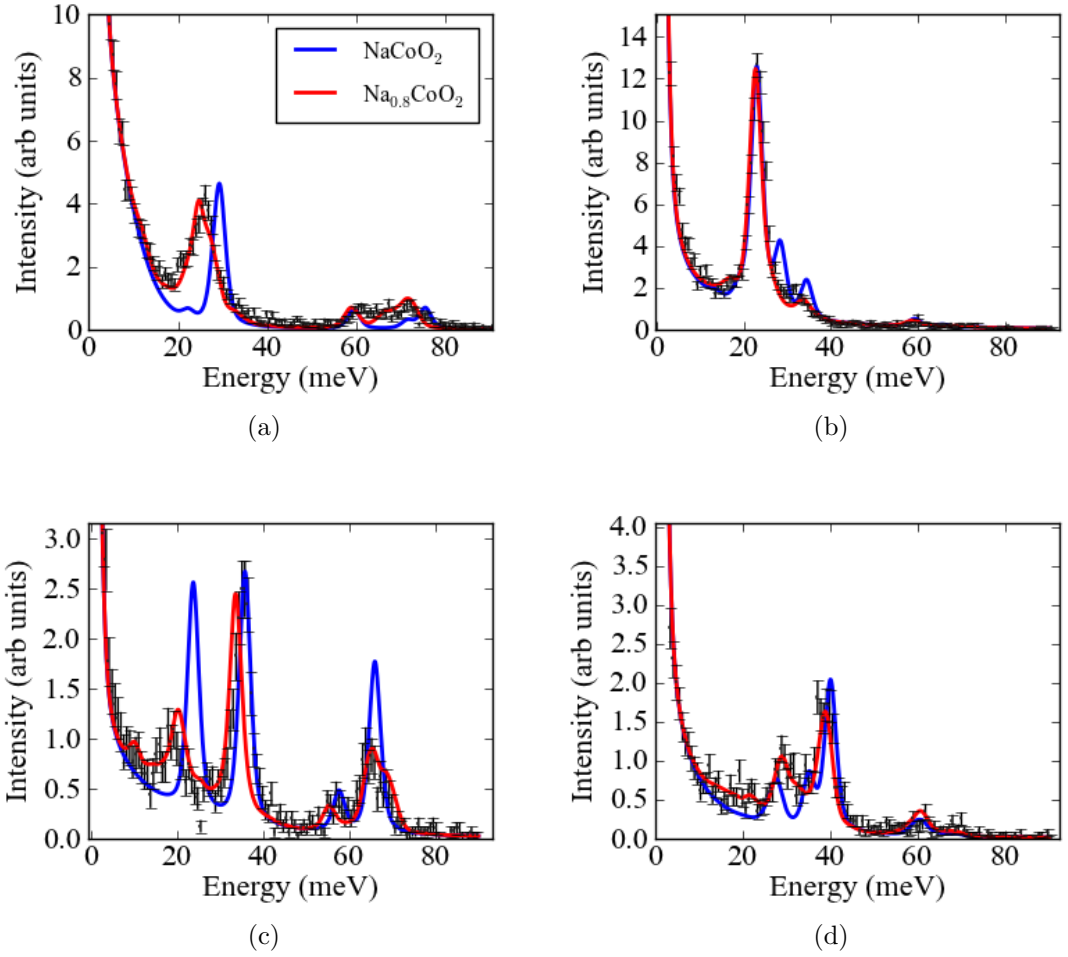

Figure 4.11: Selected energy scans from ID28. (a) (1.17,0,0), (b) (1.1,1.1,1), (c) (1.5,1.5,1) and (d) (1.17,1.17,1.08). The data are shown as the points with error bars while the two calculations are for the 8 atom cell and square phase with an arbitrary elastic line.

These low energy modes could simply be due to softening from the decrease in total number of electrons rather than an effect of the superstructure. For this reason the lattice dynamics for an 8 atom cell doped with an extra 0.2 holes per formula

unit were computed and the phonon DOS for the square phase and both 8 atom cells are shown in figure 4.12a. From this it is clear to see that at low energies both unit cell calculations are quantitatively the same. There are small shifts in the peak positions but the biggest differences occur in the region 40-80 meV. This is unsurprising as these modes involve motions of the whole Co-O layer or the higher energies correspond to O motions whose bonding would be expected to be most affected by a change in total electron density in the Co-O slabs.

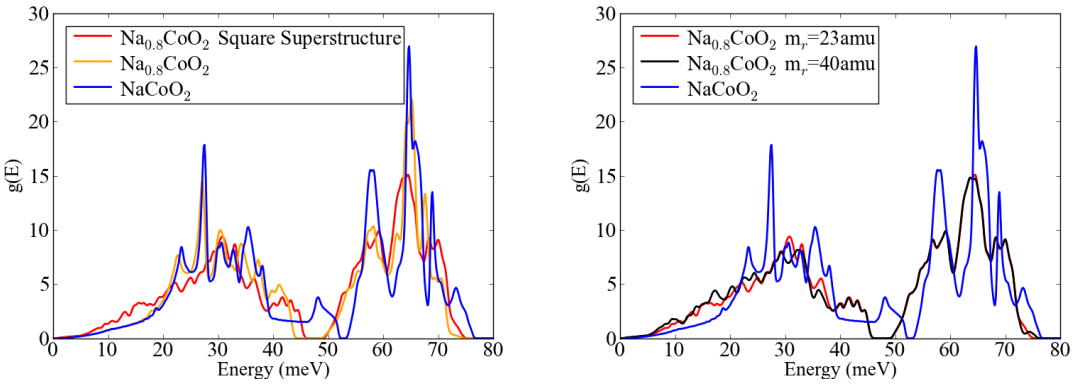

(a) (b)

Figure 4.12: The computed phonon densities of states for (a) the 8 atom cell, doped 8 atom cell and square phase and (b) the square superstructure with two different mass Na1 sites and 8 atom cell. There is only the marked shift to lower energies caused by the mixed occupancies of Na1 and Na2 sites.

Instead what is clear in this case is that there is a quite significant difference in the total weighting of the square phase at low energies. It is possible to show that these modes involve considerable coupling to the Na1 sites within the trivacancies by making a mass substitution onto these sites. In this case we retain our force constant matrix and shift the phonon frequencies from the trivacancy by an amount proportional to $\omega = \sqrt{k/m}$. This result is shown in figure 4.12b. From this it is clear that the additional scattering seen at low energies is coupled into trivacancies but that it has no real effect on modes above 40 meV.

If we return to the dispersion in figure 4.9 we can identify an approximately flat mode near K at 12 meV. Figure 4.13a shows this mode at $\vec{Q} = (1.25, 1.25, 1)$. This mode's atomic motion can be plotted in real space at the Γ point and this is shown in figure 4.13b. This mode consists mostly of motion within the trivacancy cluster with a smaller response in the walls of the cage and very little motion in the Co-O layer. Thus this mode has been identified as a "rattling" mode. As shown in the DOS there are many other modes which couple into the Na1 sites and a typical mode is shown in figure 4.13c. The rattler motion is asymmetric and thus it would be expected to be quite anharmonic. This was investigated by performing frozen phonon calculations. The results are shown in figure 4.14. The harmonic model clearly does not describe this well (the reason for a cubic fit rather than the more usual quartic is due to the asymmetry of the mode). It is challenging to go from a description of the anharmonicity to a quantitative description of phonon scattering and therefore this was investigated experimentally instead.

320 K and 400 K

The dispersion along $\Gamma - K - M$ was also measured and fitted at 320 and 400 K. There is very little change between each temperature which can be attributed to the continued existence of multivacancy clusters across the entire temperature range investigated. There was a small increase in phonon line width (as would be expected from increased phonon-phonon scattering) and some softening due to the expansion of the crystal lattice but very little in the way of clear changes.The energy scans show that the changes in the phonon dispersion are overall small with some possible changes in the range 10-30 meV. As it is not possible to perform first-principles calculations for these disordered phases no comparison to calculations is offered.

The strongest peaks whose positions are relatively easy to fit are observed to soften slightly as the system is heated indicating that they are not strongly an-

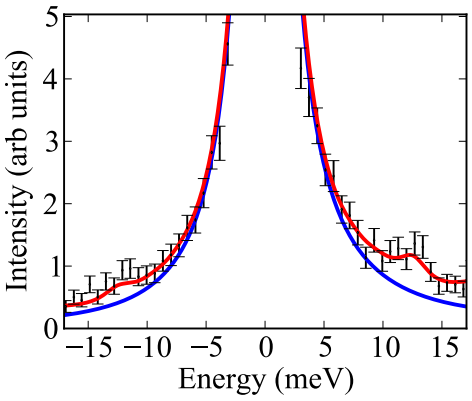

(a)

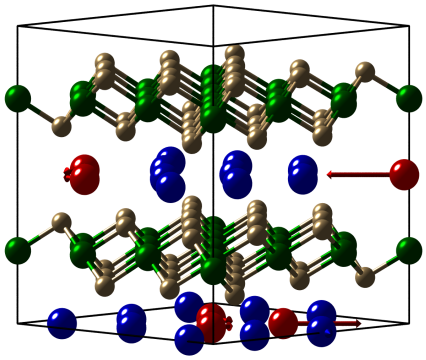

(b)

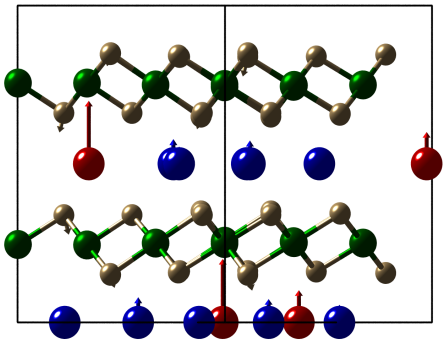

(c)

Figure 4.13: (a) The energy scan from ID28 at (1.25,1.25,1) showing the lowest energy rattling type mode as a peak at 12.5 meV (b) This rattling modes motion at the Γ point. (c) A typical optic phonon which is coupled into the Na1 sites. It is at an energy of 37.3 meV.

harmonic. Unfortunately owing to their weak intensity it has not been possible to perform the same analysis on the rattling type modes.

Phonon Lifetimes from IXS

An attempt to extract the phonon lifetimes from the data reported above has been made, however, it is extremely difficult to find a region where the overlap of phonons

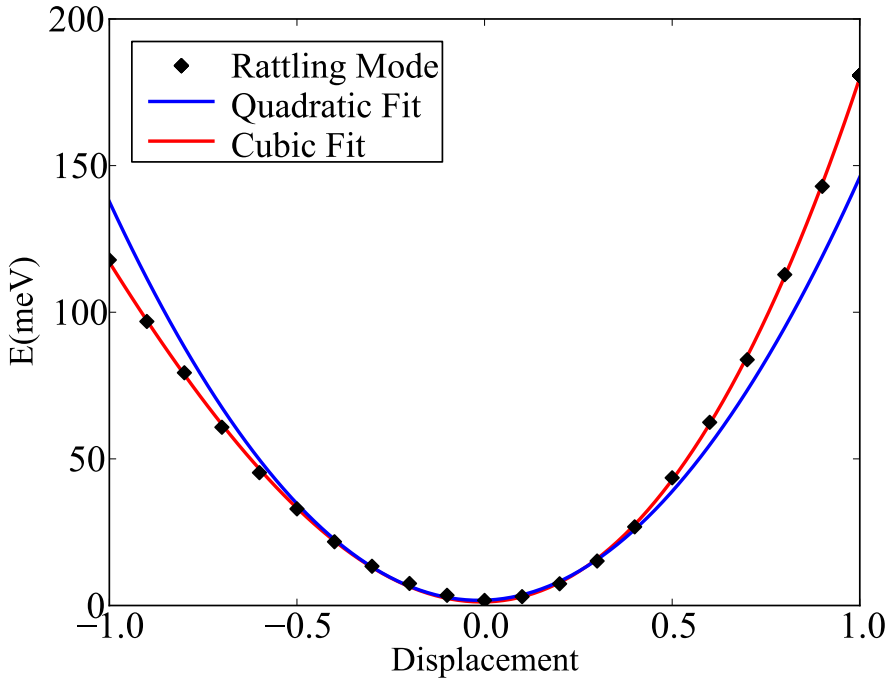

Figure 4.14: A frozen phonon calculation of the rattling mode shown in figure 4.13b. A displacement of 1 on this scale corresponds to a displacement on the Na1 site with the largest motion of 0.3 $\AA$.

does not allow for variances which are equal to the best fit of the parameter. In other words the phonon width at $x \pm x$ has not increased χ^2 by 1 (which is the definition of the variance of a parameter for the χ^2 distribution [118]). It may have been possible to overcome this by using asymmetric error analysis (where it is not assumed that one standard deviation is the same in both positive and negative directions of a parameter), however, the program fit28 does not support this.

The typical best fit values range between 0.1 and 0.4 meV however in almost all cases it is not possible to refine a physical error. In general the degree of overlap with a 3 meV resolution is too large for this process. At higher energies even the strongest modes weaken which causes problems due to the counting statistics. At low energies the intensity is much better, however, there is quite significant overlap with the elastic line.

Of the modes measured during this experiment one is particularly clean and returns a defined width for any set of fitting parameters. This mode sits at $\vec{Q} = (1.1, 1.1, 1)$. By this point an optic mode has dispersed to 20 meV where it is clear of the elastic line but still has enough intensity to give good counting statistics. The temperature dependence of this mode is plotted in figure 4.15 and the extracted values are shown in table 4.2. One other lifetime in which we can be relatively confident of the value (due to its large intensity) and which must be reported for comparison to the PGEC is that of the acoustic mode measured at (1.07,0,0). This has a width of 0.29(3) meV.

Temperature (K)	Position (meV)	Width (meV)
200	23.20 (4)	0.36 (3)
320	23.02 (5)	0.38 (3)
400	22.70 (5)	0.38 (4)

Table 4.2: The phonon lifetimes obtained from the Lorentzian half-width at half-maximum as extracted from the ID28 data for the strongest mode at $\vec{Q} = (1.1, 1.1, 1)$.

4.4.2 Phonon lifetimes from INS

No energy broadening was detectable below 120 K. The convolution of the instrumental resolution, sample mosaic and mode dispersion lead to a FWHM of 1.45 meV. The fitted lifetimes as calculated from the HWHM from the Lorentzian of the phonon are shown in Fig. 4.16 and in table 4.3. The energy scans at 50K and 275K are shown in figure 4.17.

To make sure that these widths were obtained in a system with rattling modes present a scan of the rattling mode position was made. The resolution at the elastic line of our sample in the much coarser set-up was 1.57 meV. The scans before and after background subtraction are shown in figure 4.18.

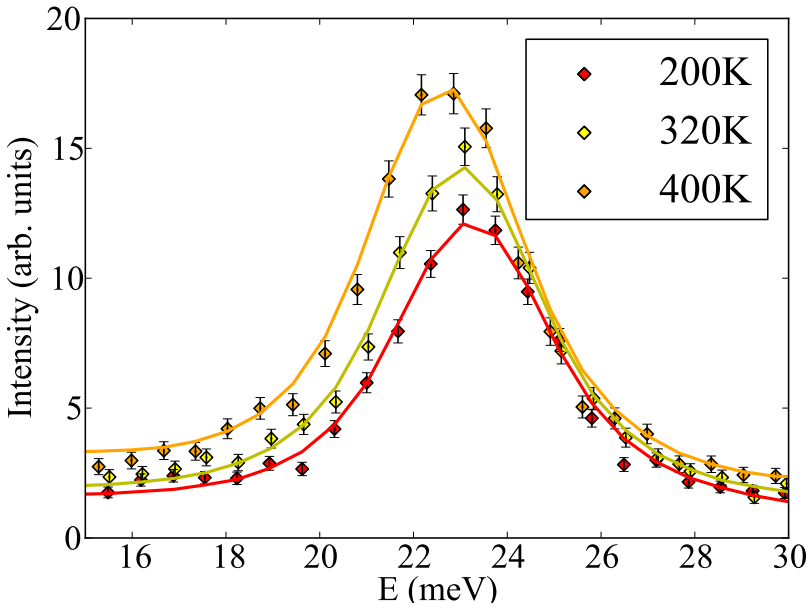

Figure 4.15: Energy scans taken at $\vec{Q} = (1.1, 1.1, 1)$. The lines are the fits to the data from the program fit28.

Temperature (K)	85	120	160	200	240	275
HWHM (meV)	0.01(5)	0.07(6)	0.16(9)	0.16(9)	0.26(7)	0.35(5)
Lifetime (ps)	60(300)	9(7)	4(1)	4(1)	2.5(3)	1.8(3)

Table 4.3: The phonon lifetimes calculated from the Lorentzian half-width at half-maximum as extracted from the IN8 data also expressed in picoseconds.

4.4.3 Impact on Thermal Conductivity

The thermal conductivity can be calculated by summing over all modes within the system at all points within the Brillouin zone (as discussed in the introduction). Realistically this means that much like a first principles calculation a sufficiently dense sampling of points will be able to describe the system adequately (especially compared to the error bars of our lifetime measurements). A $4\times4\times4$ grid of k-points was found to be sufficient for the square phase and $16 \times 16 \times 4$ for the 8 atom cell.

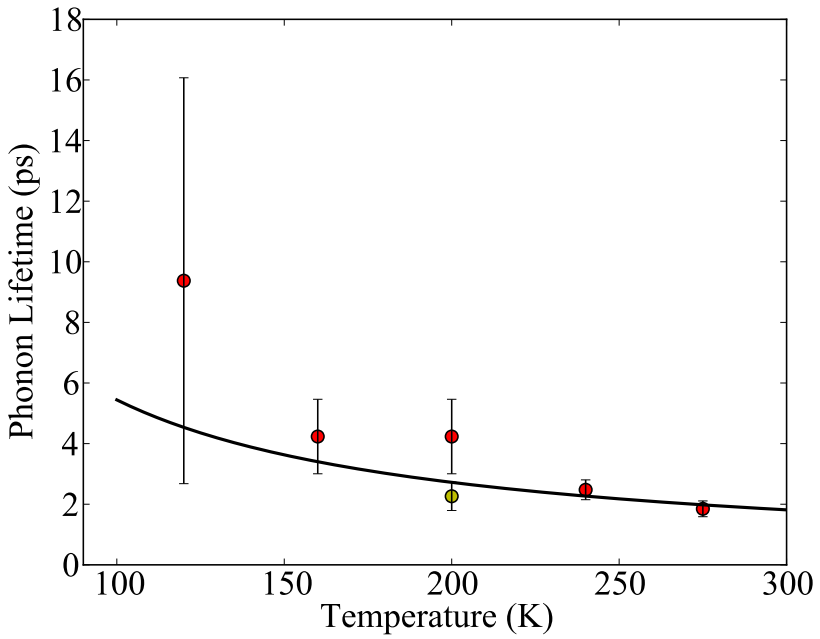

Figure 4.16: The phonon lifetimes extracted from the IN8 data and the 200 K ID28 peak for comparison.

The lifetimes measured on IN8 were assumed to apply to all phonon modes and the thermal conductivity was calculated at each temperature measured on IN8. For the 8 atom cell only the thermal conductivity at 200 K with the square phase lifetimes are shown. This is because we do not have actual lifetime (or thermal conductivity) data for the 8 atom cell and it is very much an artificial calculation.

As previously highlighted there is also a contribution to the total thermal conductivity from the electrons. This can be estimated using the Wiedemann-Franz law [65] which states that

$$\frac{\kappa}{\sigma T} = \frac{\pi^2}{3}\left(\frac{k_B}{e}\right)^2 = 2.45 \times 10^{-8}\mathrm{W\Omega K^{-2}}.$$

Using the electronic conductivity of Lee *et al.* the electronic contribution over this temperature range can be seen to be around $1/8^{th}$ of the value measured by Dr

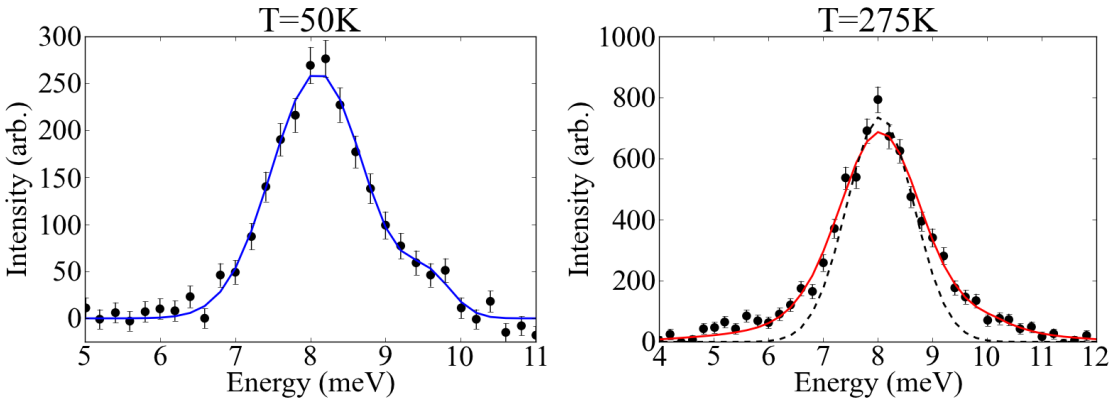

(a) (b)

Figure 4.17: Energy scans at $\vec{Q} = (1.01, 1.01, 1)$ where a single intense mode is expected from the square phase phonon calculations. (a) The scan at 50 K which is resolution limited. The feature at 9.5 meV is attributed to a spurion from higher order harmonics of the monochromator/analyser. (b) The scan at 275 K just under the transition to the disordered stripe phase. The resolution determined from the 50 K data is shown as the dashed line.

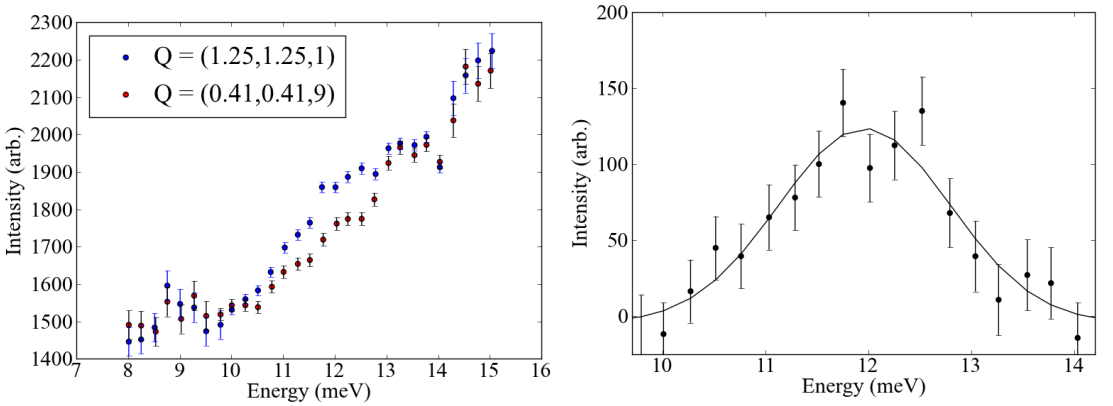

(a) (b)

Figure 4.18: Measurements of the rattling mode with IN8 in the highest flux Si-Si setup. (a) The unsubtracted data showing the very large aluminium background. (b) The rattling mode with the aluminium background subtracted. Peaked at around 12 meV and almost as narrow as the elastic line in this setup as expected for a flat mode.

D.G. Porter and thus it has been neglected. The calculated and measured thermal conductivities are shown in figure 4.19. The agreement between measurement and calculation is remarkable especially given the simplicity of the assumptions. There is a factor 6 decrease in the calculated thermal conductivity between the square and 8 atom cell calculations at 200 K. As the same lifetimes have been used this cannot be explained by some form of resonant phonon scattering phenomenon.

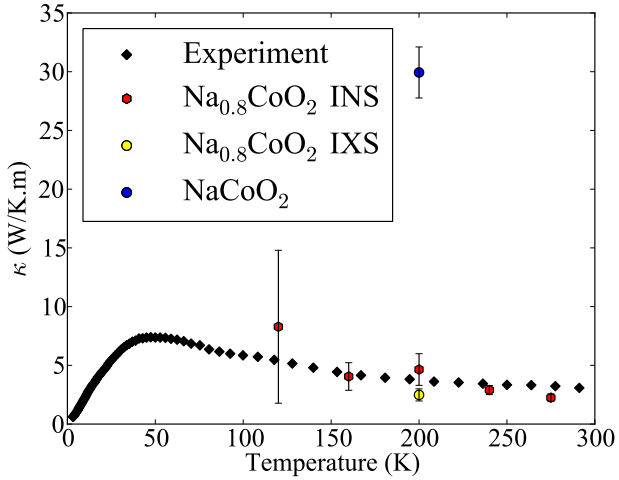

Figure 4.19: The thermal conductivity of $Na_{0.8}CoO_2$ both measured (by Dr D.G. Porter) and calculated from the CASTEP dispersions and lifetimes measured experimentally. The $Na_{0.8}CoO_2$ and $NaCoO_2$ points were calculated using the dispersions from those models respectively while the INS and IXS models refer to the origin of the lifetimes (the IXS used was the average of widths with an estimated error).

4.4.4 Comparison between Square and Stripe Phase

The measurements were performed on a single crystal. However, due to the relatively small sample sizes, it was not possible to extract usable inelastic data on the phonon dispersion due to the poor counting statistics. Figure 4.20 shows elastic data obtained by integrating the intensity from -2 to 2 meV, and the positions of the superlattice reflections enables the determination of the superstructures. In order to obtain better counting statistics, the inelastic data has been integrated over all

Q. The neutron-weighted DOS data obtained on MERLIN for the square and stripe phases are shown in Fig. 4.21. As the underlying measurements are single crystal this leads to a strong bias in the data for intensity with vibrations perpendicular to $\vec{a}$ like the rattling mode of figure 4.13b due to the (h,h,l) orientation.

The data obtained on MERLIN for the square and stripe phases respectively are shown in figure . These were single crystal (cuts integrated across the elastic line from -2 to 2 meV are shown in figure 4.20) measurements, however, due to the relatively small sample sizes it has not been possible to obtain usable data from small cuts through the data due to the poor counting statistics. For this reason the inelastic data has been integrated across all $\vec{Q}$. As the underlying

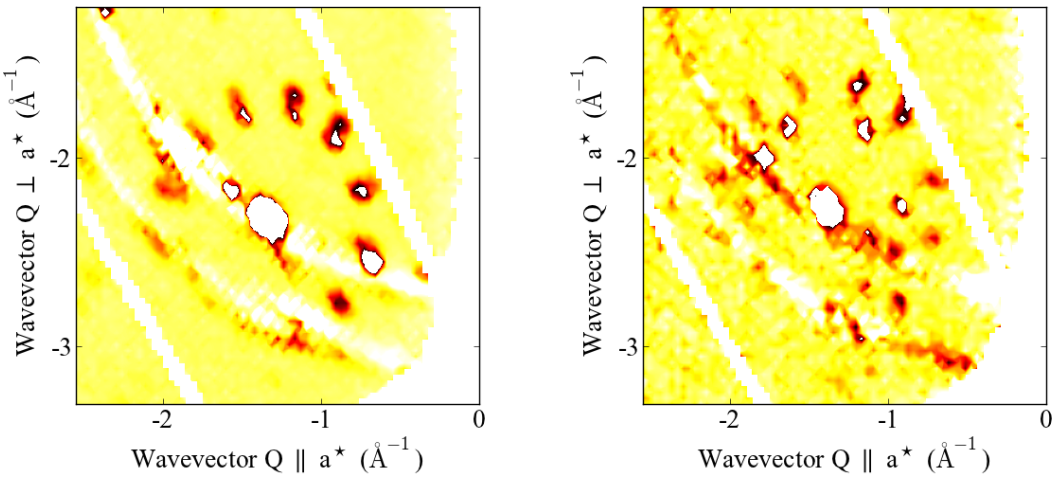

Figure 4.20: The diffraction patterns obtained on MERLIN around a (1,0,1) type reflection (integrated between ± 2 meV) for the (a) square phase and (b) stripe phase.

There are small differences in this dataset between the square and stripe phase in these data as would be expected from the calculated DOS. The calculation does not take account of the preferential orientation (this calculation is strictly only valid for

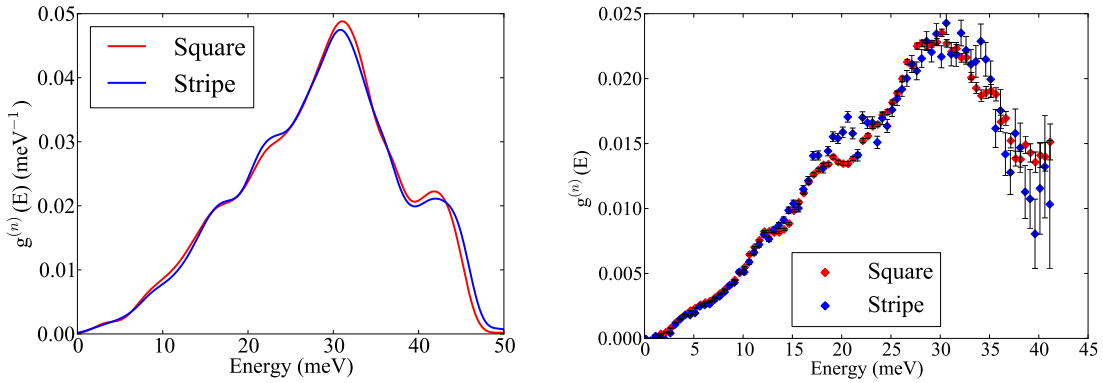

Figure 4.21: (a) The neutron weighted DOS below 50 meV showing very small changes between the square and stripe phases. (b) The data from MERLIN for both phases integrated over all values of $\vec{Q}$ measured. The data has been corrected for the Bose factor and had the elastic line subtracted, the centre of the elastic line has been used to redefine zero energy transfer.

comparison to a powder). Where differences are larger this may be attributed to the orientation of the crystal and it makes it challenging to draw specific conclusions. In both the experiment and the calculations there is no fundamental change of features, both have a shoulder at around 13 meV which can be attributed to a rattling type motion (as shown in the Na plane for both phases in figure 4.22). In the stripe phase this is slightly more washed out presumably indicating that the rattler in this system is more dispersive. Calculations of the thermal conductivity show that this subtle change in the phonon dispersion leads to a rather large 50% increase in kappa.

4.5 Discussion

The combination of momentum-resolved spectroscopy and first-principles lattice dynamics calculations show unambiguously, for the first time, that rattling modes exist in sodium cobaltate. It should however be noted that anomalous sodium vibrations

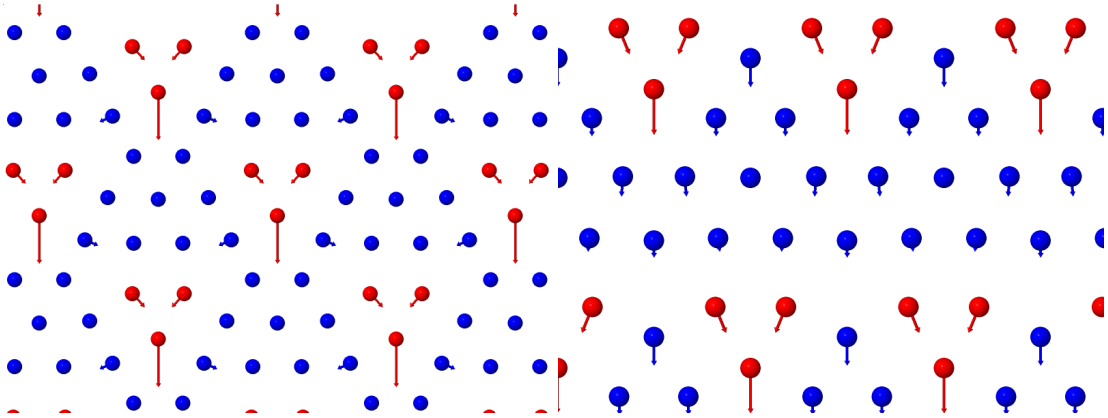

Figure 4.22: The rattling modes in (a) the square phase and (b) the stripe phase. They sit at 13 meV and 14.9 meV respectively.

has been observed in $Na_{0.75}CoO_2$ via NMR which had been suggested could be in part due to rattling type vibrations [119]. With the benefit of the calculations presented in the previous chapter it is tempting to say that the first actual observation of a phonon associated with rattling was in the original IXS measurements [120] whose data are reproduced in figure 4.23.

The IXS measurements of Rueff et al. [120] also contain scattering close to 12 meV, where none is predicted for the stoichiometric compound, see figure 4.23. It seems highly likely that this scattering is also connected to rattling modes. The nominal composition was $Na_{0.71}CoO_2$, but the stated c lattice parameter indicates some uncertainty in the precise composition, and the superstructure is unknown. The results of this chapter show how important knowledge of the superstructure is in understanding the low energy dynamics. That they see low energy dispersionless modes does imply that the rattling concept will continue to be important across a wide range of compositions. The measurements presented in this chapter of fundamentally similar dispersions as the system is heated indicate that rattlers will also continue to be important over a wide range of temperatures.

As with the skutterudites and the clathrates the observation of a rattling mode

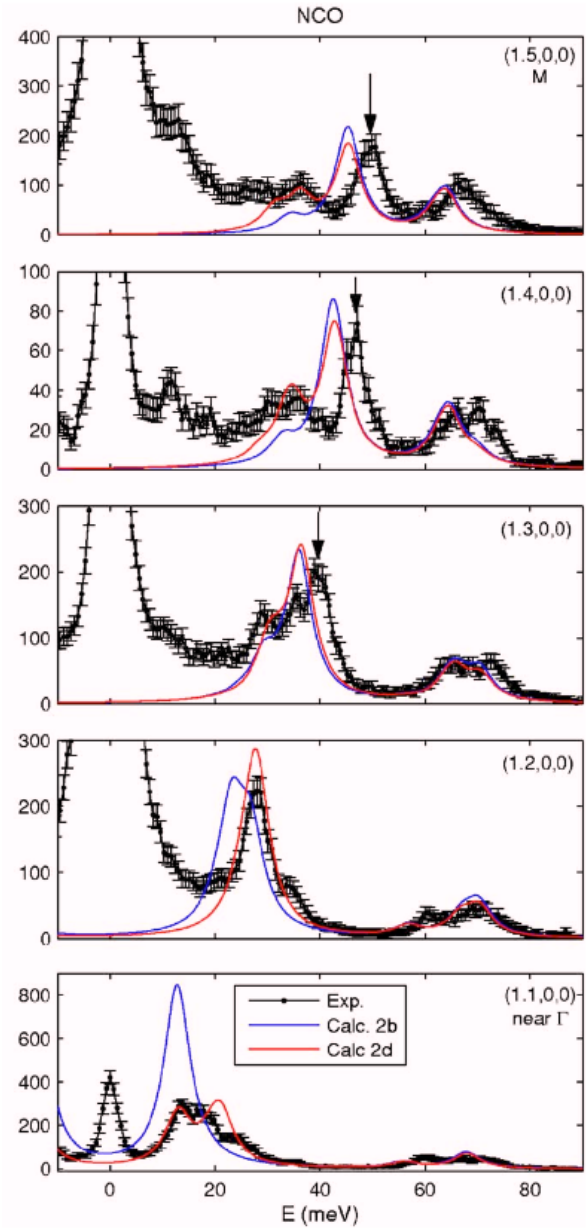

Figure 4.23: The IXS dataset obtained by Rueff *et. al.* on Na_xCoO_2. There is a noticeable amount of intensity at low energies where Na vibrations dominate. The solid lines show first-principles calculations for the 8 atom cell with Na sitting on the 2b and 2d sites respectively.

was not observed to be associated with strong phonon-phonon scattering [96, 121]. Indeed, it has even been suggested that in the filled skutterudites the lifetimes might increase rather than decrease [122] on the incorporation of rattling type atoms. For our measurements of the lifetimes to be consistent with the PGEC model the typical phonon mean free path would need to be comparable to the spacing of the rattling type sites. The typical speeds of the highly dispersive modes are around 3000 m/s. At 200 K these modes would have a mean free path of 120 $\mathring{A}$, over an order of magnitude larger than the distance between trivacancy clusters, which is utterly inconsistent with the idea of a phonon glass. While it is possible that the rattlers do increase phonon scattering it is highly improbable that scattering is the dominant suppressor of κ.

The mechanism for the suppression of κ is flattening of the phonon dispersion at low energies. The fact that the phonon mean free path is much greater than the distance between rattlers suggests that the introduction of disorder through, for example partial filling, may be used to further reduce κ. If instead in the skutterudites and clathrates it is a similar mode flattening mechanism then you would expect disorder to be able to further reduce κ. Indeed it implies that many systems with these rattling type sites might gain further improvements to ZT from being processed in nanoscale powders [80]. This is beginning to be seen in for example, in ball milled, nano-structured (with silver nanoparticles) $Ba_{0.3}Co_4Sb_{12}$ leading to a 30% gain in ZT [123].

The subtle differences between square and stripe phases opens up exciting possibilities for tuning the thermal conductivity by changing the nature of the rattlers. That there is a measurable difference in the phonon dispersions between the square and striped phases is promising given the change in trivacancy environments. The moderate change in thermal conductivity between the two phases was surprising but is consistent with the measurements of Lee *et. al.* who had a variation in κ of

approximately 60% across the composition range where trivacancies dominate [124].

4.6 Conclusions

A single crystal of $Na_{0.8}CoO_2$ was studied with inelastic x-ray scattering. At 200 K it was observed to be in the square phase superstructure and good agreement was obtained between the measurements and first principles calculations. A significant amount of additional intensity (compared to an Na_1CoO_2 system) was observed at low energies which can be attributed to the presence of rattling type vibrations on the Na2b sites [86]. Little difference was observed between the square, disordered stripe and disordered phases apart from a small amount of softening associated with the expansion of the lattice.

Detailed measurements of the phonon lifetimes found phonon scattering for temperatures at and greater than 120 K however they were found to be inconsistent with the PGEC picture which would require them to have been an order of magnitude shorter. The combination of these lifetimes and the validated first-principles calculations enabled the lattice thermal conductivity to be calculated and excellent agreement was obtained between the calculated value and experimentally determined thermal conductivity. There was a factor 6 increase in the calculation of the 8 atom cell thermal conductivity which could be attributed to the introduction of flat modes at low energies in the square phase.

Finally measurements on the ordered stripe phase showed that there were differences in the phonon dispersion for the two systems. Somewhat surprisingly this led to a 50% increase in the thermal conductivity which suggests that it may be possible to control the thermal conductivity in this compound through changing the environment of the rattlers.

Chapter 5

Rattling modes in divacancy Na_xCoO_2

5.1 Background

It is rare that a material is naturally perfect for its intended application. Often particular properties can be improved by doping with different elements. In the case of thermoelectrics doping can affect all three relevant properties in different ways. For example, doping a monovalent site with a divalent ion would change the carrier concentration, affecting both the electrical conductivity and Seebeck coefficient [11]. The electronic contribution to the thermal conductivity will also be affected, however, it is non-trivial to understand the effect of the dopant on the lattice thermal conductivity. In compounds with rattlers the thermal conductivity has been tuned by doping onto the rattler sites. An example of this is the clathrate $Ga_{16}Ge_{30}$ doped with Ba, Sr and Eu, in which each dopant changes the thermal conductivity, but also changes the functional form of the thermal conductivity [88].

5.1.1 Thermoelectric properties of the doped cobaltates

Several studies have looked at the role of doping on Na_xCoO_2. Initial work focussed on changing the Na concentration (which changes the hole doping within the CoO_2 slabs) and it was found that the Seebeck coefficient was improved as x was increased [124]. This showed that the Seebeck coefficient was controlled by the number of holes in the CoO_2 slab since the removal of $\delta = (1 - x)$ Na ions creates δ holes in the Co layers. There is, however, an upper limit $x = 0.85$ (which corresponds to $\delta_m = 0.15$), where phase separation with the $x = 1$ insulating phase occurs. The substitution of a divalent ion for Na decreases by one the number of holes in the Co layer. This offers the opportunity to decrease δ below δ_m and further enhance ZT.

It was observed in the thesis of M. Pandiyan that there is also a factor three decrease in the thermal conductivity of Na_xCoO_2 for large x values, attributed to the superstructure changing from divacancy clusters to trivacancy clusters ($x \geq 0.71$) [3] as shown in figure 5.1. Experimentally it is extremely challenging to obtain high quality single crystals of divacancy phases of Na_xCoO_2 anywhere apart from insulating $x = 0.5$ [1], which is of less interest for thermoelectric applications. It is, however, possible to obtain a divacancy structure which is manageable both experimentally and computationally when doping with Ca [125].

Ca doping at low Na concentrations (around $x = 0.55$) was probed shortly after the initial work on Na_xCoO_2 as a way of further reducing the hole doping within the CoO_2 slabs. It was shown that the Ca negatively impacted resistivity but positively impacted on the Seebeck co-efficient [126] leading to an overall increase in the power factor. Another study investigated three different dopants (Ca, Sr, K) around $x = 0.8 - y$. Here it was found that K reduced the power factor, Ca gave a moderate increase (for concentrations with less Ca than $Na_{0.55}Ca_{0.25}CoO_2$) and Sr gave the largest increase [4] as shown in figure 5.2. Neither of these studies

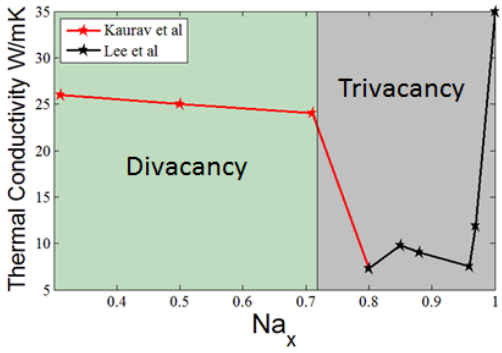

Figure 5.1: The thermal conductivity at 300 K as a function of sodium concentration compiled from the literature in the thesis of M. Pandiyan [3].

investigated the thermal properties.

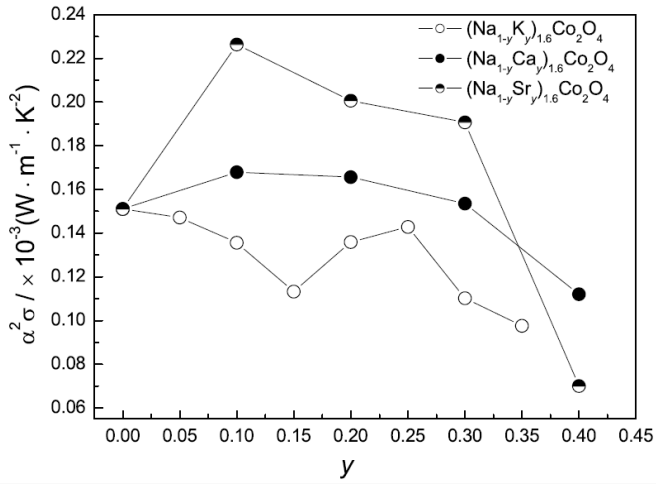

Figure 5.2: The power factor of several doped cobaltates reproduced from Ref. [4].

Some limited measurements of the thermal conductivity in doped compounds have been made. One investigated a large range of dopants (including monovalent, divalent and trivalent) at high temperatures and found that all the dopants investigated apart from Y suppressed the thermal conductivity by up to 40% [127], however, they did not investigate Ca doping. Another measurement which looked only at Ca doping in polycrystalline samples found that there was little difference

between the doped and undoped compounds with both having a thermal conductivity which increased with temperature [128], suggesting that disorder is the primary phonon scattering mechanism.

There has been a solitary Raman scattering measurement on the Ca doped system. This measurement investigated the system's suitability for battery applications and only observed a small hardening in the phonon frequencies which was attributed to the decreased lattice parameter [129].

5.1.2 Structure of $Na_xCa_yCoO_2$

As already mentioned, Ca doped $NaCoO_2$ adopts a divacancy superstructure. There are in fact, two different divacancy structures [125], the first at lower Ca concentrations corresponds to a nominal concentration of $Na_{0.57}Ca_{0.14}CoO_2$ and displays a superlattice indexed on a $1/7^{th}$ grid with propagation vectors

$$\vec{a'} = 2\vec{a} - \vec{b}$$

$$\vec{b'} = \vec{a} + 3\vec{b}.$$

There is a small contraction in a from 2.85 to 2.84 Åand in c from 10.8 to 10.75 Å. The Ca ion sits on the crystallographic 2b site with Na forming a ring around each Ca ion as shown in figure 5.3. While this structure has the same vacancy concentration as $Na_{0.71}CoO_2$ its structure is distinct as the pure Na phase has stripes of divacancy clusters with a complicated and as yet unresolved c dependence [3]. This makes the pure system impossible to treat properly with DFT at the present time.

There is a second superstructure observed when the system is prepared with a nominal Ca concentration greater than 0.14 per Co. This phase corresponds to a nominal concentration of $Na_{0.25}Ca_{0.25}CoO_2$ and for the purposes of this chapter will be treated as a contaminant phase as it has yet to be observed independently of the

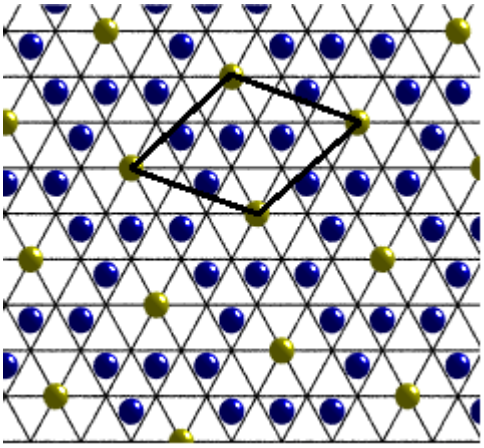

Figure 5.3: The in-plane superstructure of $Na_{0.57}Ca_{0.14}CoO_2$.

$^1/_7{}^{th}$ phase.

In this chapter we focus on a calcium doped sample of ideal composition for the superstructure in figure 5.3 in part because the concentration of Ca is close to the maximum of the power factor and also because it is possible to grow small single crystals of very high quality for this phase. Other de-intercalated Na_xCoO_2 compositions and Sr doped samples have promising thermoelectric properties but they have much more complicated supercells. The advantage of the relatively simple $Na_{0.55}Ca_{0.14}CoO_2$ system is that its smaller superstructure makes DFT calculations quite affordable.

5.2 Experimental procedure

5.2.1 X-ray measurements on Xcalibur

A small crystal ($400 \times 400 \times 10\mu$m) of nominal composition $Na_{0.57}Ca_{0.14}CoO_2$ was cleaved from the larger growth boule. It was found to be a single crystal with a superlattice indexed on a $^1/_7{}^{th}$ grid and no intensity at the $^1/_4$ positions implying that it is a single phase. The $(h, k, 0)$ plane is shown in figure 5.4.

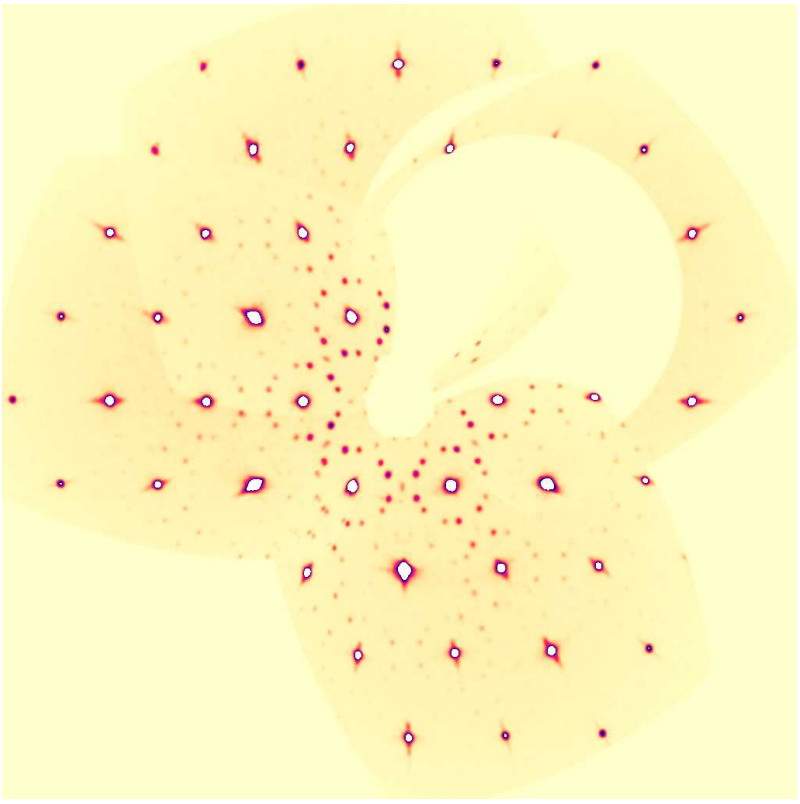

Figure 5.4: The $(h, k, 0)$ plane of the calcium doped sample measured on ID28. $\vec{a^*}$ is horizontal and $-\vec{a^*} + 2\vec{b^*}$ vertical. The ring of peaks around each principal Bragg reflection is from the $^1/_7{}^{th}$ divacancy phase.

5.2.2 Inelastic x-ray measurements on ID28

The crystal screened on Xcalibur was mounted on a 0.1 mm capillary and taken to ID28 at the ESRF. The beamline was initially aligned with the Si (9,9,9) reflection (incident energy 17.9 keV) giving a resolution of 3 meV at the elastic line. The toroidal focussing mirror was again used to improve flux. The sample was aligned in (h, h, l) and measurements along Γ-K-M were made around the (1,1,1) at 290 K from -20 to 90 meV in 0.68 meV steps. The sample was then cooled to 200 K and a scan at (1.25,1.25,1) was performed to ensure that there were no significant changes in the phonon dispersion on cooling. The sample was then re-aligned in the $(h, 0, l)$

orientation and scans were made along Γ-M from -20 to 90 meV in 0.68 meV steps around the (1,0,0). As with the previous experiment addIXS and fit28 were used for the data treatment.

Finally a temperature dependence was performed at (-1.17,0,0). The beamline was re-aligned on the Si (11,11,11) giving a FWHM of 1.5 meV and scans were made from -3 to 13 meV. Each scan was repeated a number of times to build up statistics. The counting time at a single position could not be simply increased indefinitely as the monochromator is not stable over long periods of time. The final scans were made by fitting to the elastic line and fixing it at zero before summing the data using addIXS. The temperatures measured at were 100, 200, 280 and 360 K.

5.3 Computational procedure

Lattice dynamics calculations were performed for the divacancy $^1/_7{}^{th}$ structure in figure 5.3 for the cases of Ca and then Na at the 2b site. These calculations enabled the assignment of modes and further analysis to be performed.

5.3.1 Exchange, correlation and pseudopotentials

The ultrasoft pseudopotentials designed by Prof K. Refson which were used in the previous chapter for Na, Co and O were used again here. The default ultrasoft pseudopotential from CASTEP 7.0 was used for Ca. The custom pseudopotential strings were

O 2|1.5|12.86|16.537|18.375|20UU:21UU(qc=6.25)[2p4.75],

Na 2|1.3|1.3|1|11.8|13.6|15.3|20U=-2.07:30U=-0.105:21U=-1.06U=0.25[],

Co 3|2.5|2.5|1.5|5.9|7.7|10|40UU:32UU:41UU4s1.95,4p0.05(qc=4)[].

Exchange and correlation were treated with the approach of Perdew, Burke, and Ernzerhof [62].

5.3.2 Plane wave convergence and Brillouin zone sampling

A plane-wave cut-off of 500 eV was found to be sufficient with a maximum error in the forces of 0.0045 eV/Å. A k-point grid with a density of $6 \times 6 \times 4$ was found to lead to a maximum error in the forces of 0.005 eV/Å.

5.3.3 Other parameters

As both the de-intercalated and doped compounds are metallic a Gaussian smearing width of 0.1 eV was used to improve convergence. It was found that a fine grid scale of $3 \times E_{\text{cut}}$ was required to converge the forces to the same level as that of the plane-wave cut-off and k-point grid. It was not found to be necessary to increase the standard grid above $1.75 \times E_{\text{cut}}$. The magnetic ground state was investigated and found to be an A-type antiferromagnet as is seen in the $Na_{0.8}CoO_2$ system [115] for both calcium-doped and pure systems.

5.3.4 Phonon calculations

Both systems were geometry optimised with the low memory BFGS method [130, 131] such that the largest residual force was 0.0022 eV/Å. The force constant matrix was computed with the finite-displacement supercell method [78, 79]. A cell of size 2×2 was used in these calculations with in-plane lattice parameters of length 15.04 Å.

5.4 Results

5.4.1 The phonon dispersion of $Na_{0.57}Ca_{0.14}CoO_2$

The measurements performed on ID28 showed that the changes between the square and $^1/_7{}^{th}$ phases were small. The fitted and calculated dispersion is shown in figure 5.5 with the full dispersions if figure 5.6. There are changes across the entire energy range. At low energy there are changes in position and intensity presumably due to the superstructure and at high energy changes in the O modes due to the change in hole doping.

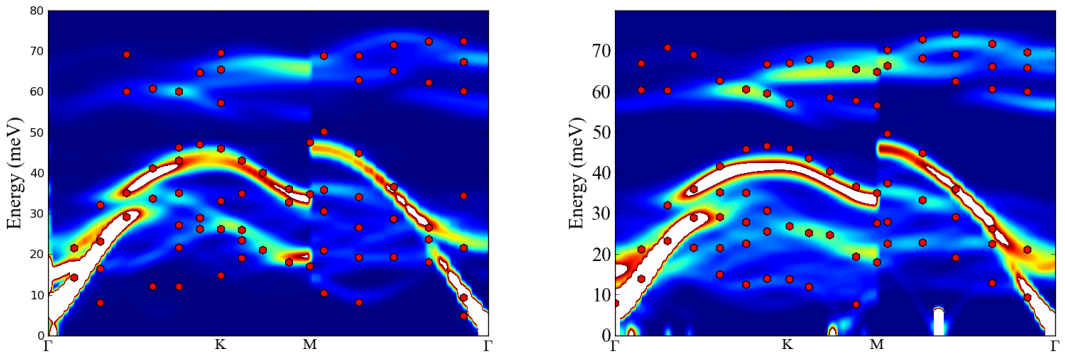

(a) (b)

Figure 5.5: The computed phonon dispersions from (1,1,1) to (1.5,1.5,1) (Γ-K-M) and (1.5,0,0) to (1,0,0) (M-Γ) for the Ca doped $^1/_7{}^{th}$ (a) and square phase (b). The red hexagons indicate where it was possible to fit individual modes in the ID28 data. In the $^1/_7{}^{th}$ phase data along (Γ-K-M) was taken at 290 K while (Γ-M) was at 200 K.

The agreement is very good along Γ-M however along Γ-K-M, while there are changes compared to the square phase, they agree less well with the calculation. In particular there are several peaks observed around 12 meV close to K which are very similar to the rattling mode peak of the square phase. It is possible that

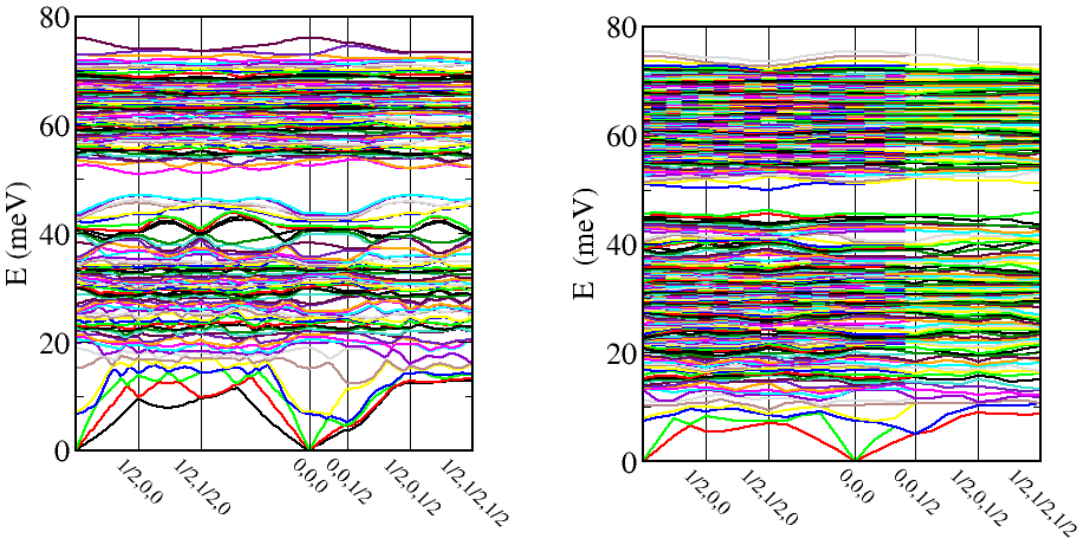

Figure 5.6: The computed phonon dispersions around the irreducible wedge for the Ca doped $^1/_7{}^{th}$ (a) and square phase (b).

there are isolated trivacancies within this sample and if so they may contribute only incoherent elastic scattering (explaining why they do not show up in diffraction) but their excitation spectrum should remain similar.

In Γ-M there is a clear flat mode at just below 20 meV which is well resolved in the energy scans from ID28 and is not present in the original square phase as shown in figure 5.7a. This mode when plotted at the Γ point resembles a Ca "rattler" however it is not the lowest lying rattling type mode shown in the calculations in this system. That mode is at an energy of 14.9 meV and is shown in figure 5.7b.

Attempts to extract the phonon lifetimes by fitting the higher resolution scans around (1.17,0,0) proved inconclusive. Only the acoustic phonon in detector 1 (at (1.055,0,0.06)) proved to have enough intensity for an attempt at fitting to be made. This was not found to have a sensible temperature dependence with a HWHM of 0.21(7) meV at 100 K and 0.17(4) meV at 300 K. This is attributed to the summing

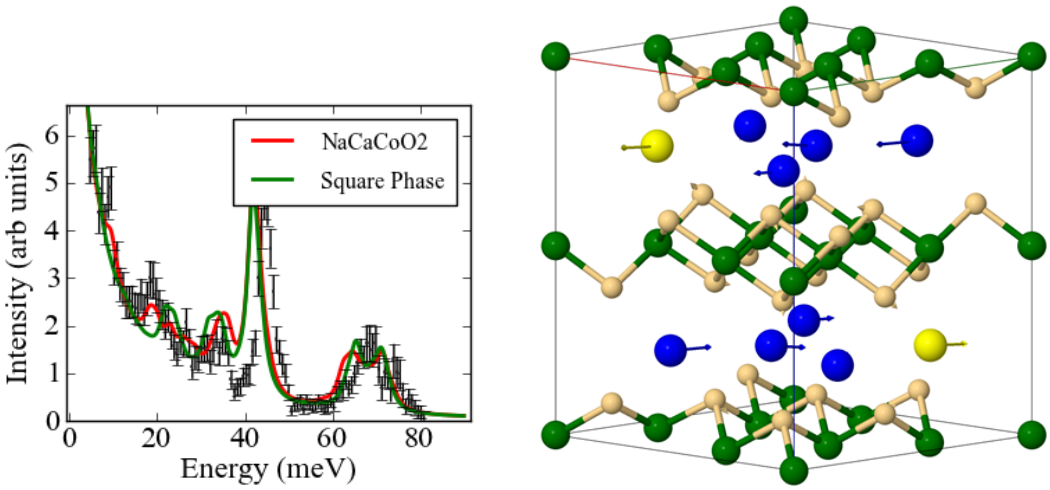

(a) (b)

Figure 5.7: An energy scan at (1.37,0,0) taken at 200 K with the calculations for the Ca doped $^1/_7$ and square phases showing clear differences below 30 meV. (b) The Ca rattling mode at 14.9 meV.

together of multiple scans to build up statistics. The number of scans used correlates with the width of the elastic line (which should have no temperature dependence). This suggests that the observed widths were mainly due to a drift in the temperature of the monochromator between scans and it was not possible to completely correct for this. In the lower resolution data it was not possible to extract any widths implying that if anything the phonon lifetimes may be longer than those of the square phase.

5.4.2 Comparison to $Na_{0.71}CoO_2$

To compare to the undoped compounds and their anomalous factor 3 increase in thermal conductivity upon adopting a divacancy structure a pure Na analogue of the $^1/_7{}^{th}$ phase was investigated. This system was, unsurprisingly, found to have very similar lattice dynamics to the Ca doped system. There was a small shift in the energy scale of the lowest lying "rattling mode" from 14.90 to 16.39 meV with small

shifts in the DOS as shown in figure 5.8. A small shift between the two compounds would be expected as, while there is approximately a factor two difference in rattler mass between the Na and Ca, there is also a doubling of the charge state. These two contributions would shift the rattler energy in opposite directions leading to a net cancellation. There are small changes in the high energy modes due to the change in hole concentration, however, they would not be significantly thermally populated in the temperature range investigated and should not impact the thermal conductivity.

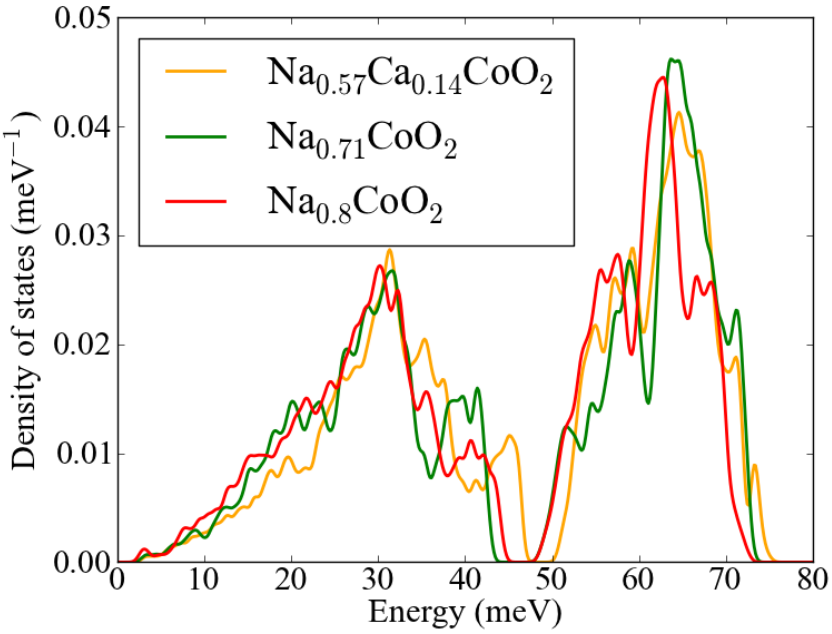

Figure 5.8: The computed phonon DOS for the divacancy phases, Ca doped, pure $^1/_7{}^{th}$ and square phase. Note the drop in spectral weight below 15 meV caused by the shift in rattling mode energy.

In both cases the rattler was found to be more strongly coupled into the walls of the cage. This would be expected to increase the dispersion of the rattling modes and thus have a smaller effect on the average mode velocity. Furthermore the shift to higher energies should further reduce this effect.

5.4.3 The Thermal Conductivity

As it was not possible to extract meaningful lifetimes from the measurements on the Ca doped system the lifetimes obtained on IN8 for the square phase have been used for a comparison. This is an unsatisfactory approximation as the lower resolution measurements suggest that if anything the lifetimes are longer but it has not been possible to place a bound on this.

The calculation of κ_l showed a factor two increase in the thermal conductivity moving between the square and $^1/_7{}^{th}$ phases. There is less than a 1% difference between the two divacancy calculations which is surprising. This suggests that the dominant factor in controlling the thermal conductivity is the nature of the rattling site rather than the rattling ion itself.

5.5 Discussion

The change in superstructure clearly has a noticeable impact on the lattice thermal conductivity. That there is no change between the pure and Ca doped systems is somewhat surprising and suggests that it is changes in the superstructure which are the most important in the control of thermal conductivity in the cobaltates not the rattling ion itself.

This may go some way to explaining the observed factor 3 increase between tri and divacancy compositions in the literature (as shown in figure 5.1). While the increase here is smaller than that observed experimentally the structure is not the same as that which is actually observed experimentally [3].

The in-plane superstructure of $Na_{0.71}CoO_2$ was originally proposed by Y. Hinuma *et. al.* [5] and is shown in figure 5.9. This structure is more reminiscent of the stripe phase than the square phase and perhaps the striped structure leads to another small increase in the thermal conductivity. This is supported by the previous chapter

where it was found that the arrangement of trivacancies into stripes led to an increase in κ of 50%.

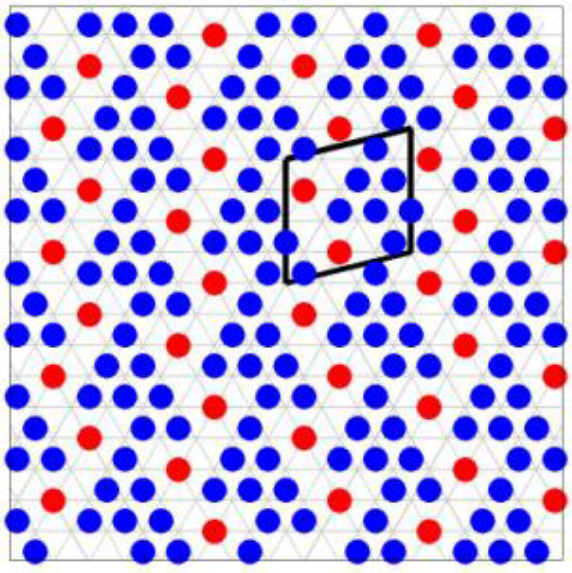

Figure 5.9: The in-plane structure of $Na_{0.71}CoO_2$ showing stripes of divacancy clusters. Figure produced by Dr. D.G. Porter from the work of Y. Hinuma *et. al.* [5].

It is disappointing not to be able to say anything more conclusive about the lifetimes when changing from tri to divacancy structures. Unfortunately crystals large enough for inelastic neutron scattering are not available and IXS is the only possible technique. In a future experiment an extraction of lifetimes may be possible if great care is taken in the preparation of a sample such that its thickness is optimised for maximum intensity reducing the overall counting time.

5.6 Conclusions

The change of superstructure to divacancy clusters has a noticeable impact on the phonon dispersion and correspondingly the overall thermal conductivity. The dispersion has been computed and validated with IXS measurements for $Na_{0.57}Ca_{0.14}CoO_2$ with particularly good agreement obtained along Γ-M around the (1,0,0).

The changed superstructure shifts the rattling modes to higher energies and the rattling ion is more strongly coupled into the cage walls. This increases the phonon velocities at low energies relative to the square phase and leads to an increase in the total thermal conductivity. Calculations performed for $Na_{0.71}CoO_2$ show that this increase is a property of the structure not the dopant. These two results can help to explain the large increase in thermal conductivity when moving from tri to divacancy structures previously observed. While this increase essentially rules out divacancy structures for thermoelectric applications it suggests that some effort should be made to identify new superstructures. An example of this could be the recently observed Sr doped superstructure [2] which is fundamentally different from the previously studied vacancy superstructures.

Chapter 6

Superlattices and Symmetry Breaking in the iron chalcogenide superconductors

6.1 Background

The discovery of superconductivity at 26 K in LaFeAsO when lightly doped with F^- ions [132] has caused a flurry of activity within the condensed matter community. There are now 6 different iron based structures which lead to superconductivity. They all have a common Fe-As or Fe-Se layer with the arsenic/selenium ion tetrahedrally coordinated around the iron sites. These 6 families are known as the 1111 (LaFeAsO), 122 (MFe_2As_2), 111 (MFeAs), 11 (FeSe), 21311 (Sr_2VO_3FeAs) and 245 ($M_{0.8}Fe_{1.6}Se_2$) where M is an ion for which there are several possibilities in each structure [20].

This chapter is concerned with the 245 class $M_{0.8}Fe_{1.6}Se_2$ where M=K,Cs,Rb. Superconductivity was first observed in the potassium doped system with an onset temperature of 30.1 K [133]. This was quickly followed by single crystal work which

raised the transition temperature to 33 K [134] and the observation of very similar properties in the caesium [135] and rubidium [136] compounds. Much excitement was caused by the observation of strong antiferromagnetism co-existing with the superconductivity (T_N=560 K and 3.2 μ_B moment) [137]. Several superstructures have been observed in these compounds [138], and a question arises as to the nature of the magnetism and superconductivity in each superstructure.

6.1.1 Structure

The unit cell structure of the materials is the same as the high temperature phase of $BaFe_2As_2$, $I4/mmm$ [139]. On cooling they are all observed to form a superlattice with a $\sqrt{5} \times \sqrt{5} \times 1$ cell and the space group $I4/m$ [140, 141]. The propagation vectors of this phase are

$$\vec{a'} = 2\vec{a} + \vec{b}$$

$$\vec{b'} = -\vec{a} + 2\vec{b}.$$

This superlattice based on iron vacancies has also been observed in the similar, but non-superconducting, system $TlFe_{1.6}Se_2$ [142]. This has been identified as being based around iron vacancies. The iron vacancy structure is shown in figure 6.1.

There have been reports of a number of additional vacancy superstructures. These include a rhombus phase ($AFe_{1.5}Se_2$) [143], a 2×2 supercell ($AFe_{1.75}Se_2$) [144] and a $\sqrt{2} \times \sqrt{2}$ phase [141]. There have been many different observations of the $\sqrt{2} \times \sqrt{2}$ phase but, no study has been able to explain all its observed features.

The original observation of the $\sqrt{2}\times\sqrt{2}$ phase with neutron scattering in $Rb_yFe_{1.6+x}Se_2$ suggested that it had half iron occupancy in the $Pmna$ space group. However, they also observed the superlattice peaks to be rod-like along $\vec{c}$, which could not be explained with this 3D structure [141]. Scanning probe measurements have suggested that this phase is stoichiometric AFe_2Se_2 with charge ordering giving rise to the

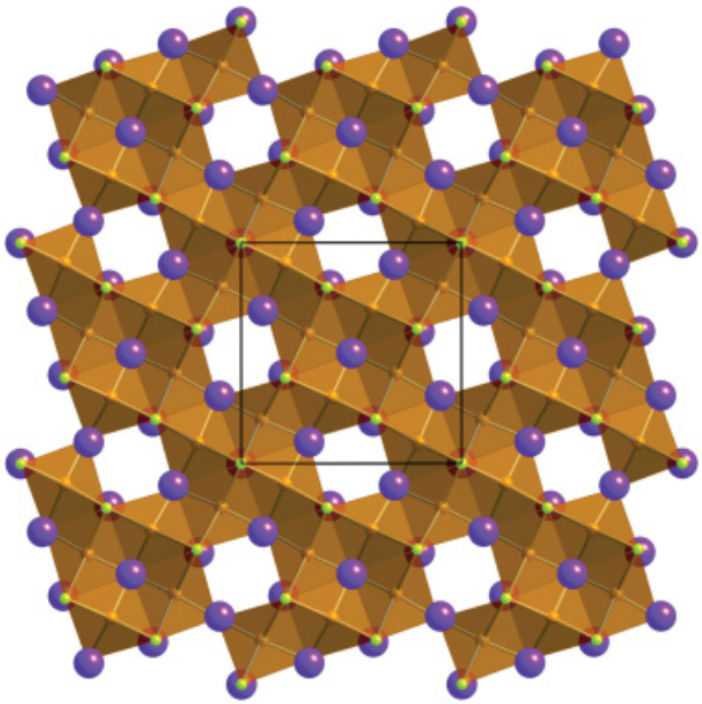

Figure 6.1: The $\sqrt{5} \times \sqrt{5}$ Fe vacancy superstructure from Ref. [140]. The alkaline metal ions are purple, Fe is brown and Se is green.

superlattice [138]. High resolution x-ray measurements have shown that this phase, as well as being disordered along $\vec{c}$, also has a small monoclinic distortion of 0.25° [145]. It was argued that the $\sqrt{2} \times \sqrt{2}$ phase remains I centred and, therefore the FeSe layer cannot be responsible for the disorder along $\vec{c}$ [145].

The presence of superstructures results in a splitting of the principal Bragg reflections. The first, which can be associated with the $\sqrt{5} \times \sqrt{5}$ phase, has $|a_{\sqrt{5}}| = 3.97\ \mathring{A}$ and $|c_{\sqrt{5}}| = 15.25\ \mathring{A}$, while a second component (associated with the $\sqrt{2} \times \sqrt{2}$) has $|a_{\sqrt{2}}| = 0.98|a_{\sqrt{5}}|$ and $|c_{\sqrt{2}}| = 1.02|c_{\sqrt{5}}|$ [145]. The two phases are spatially separated with domains the order of 0.1-1 μm, as shown in nano-focussing x-ray diffraction measurements [146].

6.1.2 Magnetism

It has now been determined that the room temperature phase of the $\sqrt{5} \times \sqrt{5}$ phase is antiferromagnetic [137]. Getting to this point has been somewhat challenging as the magnetic structure is commensurate with the underlying superstructure and there are two possible magnetic structures which would give scattering consistent with the initial powder measurements. Single-crystal measurements, however, were able to show that it is the so-called Block-AntiFerroMagnetic (BAFM) structure which is actually observed [141]. This magnetic structure is shown in figure 6.2. The authors of Ref. [141] also performed polarized neutron measurements on the $\sqrt{2} \times \sqrt{2}$ phase in the same study, but did not observe any scattering in the spin-flip channel, leading them to conclude that it was not magnetically ordered.

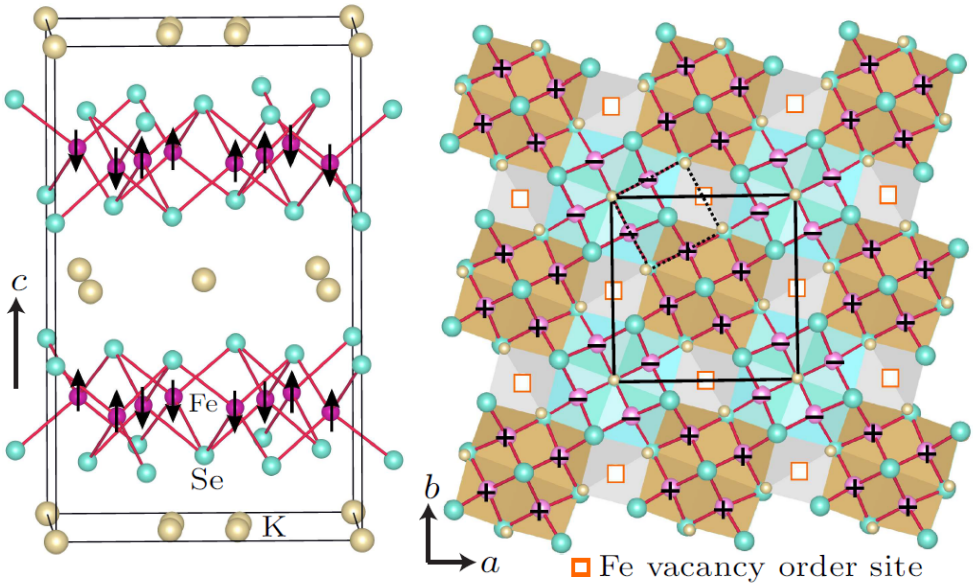

(a) (b)

Figure 6.2: The BAFM magnetic structure proposed in Ref. [137] and confirmed in Ref. [141] for the $\sqrt{5} \times \sqrt{5}$ structure. (a) The side view and (b) the top view. Positive and negative symbols denote the different spin up and down sites.

First-principles calculations for the $\sqrt{5} \times \sqrt{5}$ and a stoichiometric phase per-

formed within the LDA+U formalism (U=2eV) showed that, even for stoichiometric KFe_2Se_2, a BAFM type structure was energetically favourable [147]. This related BAFM structure (henceforth referred to as BAFM′) is shown in figure 6.3. The magnetic ordering and superstructure formation in the $\sqrt{5} \times \sqrt{5}$ phase occur within 20 K of each other [137] and given that the BAFM seems to be stable at several compositions this suggests that there may be strong coupling between the structural and magnetic properties. Reference [147] also performed variable cell geometry optimisations and found strong magneto-elastic coupling. Changes in the magnetic structure (with changes of less than 1% in the total moment) led to changes of the lattice parameters of around 2-3%. If a non-magnetic calculation was performed the lattice parameters collapsed by around 7% [147].

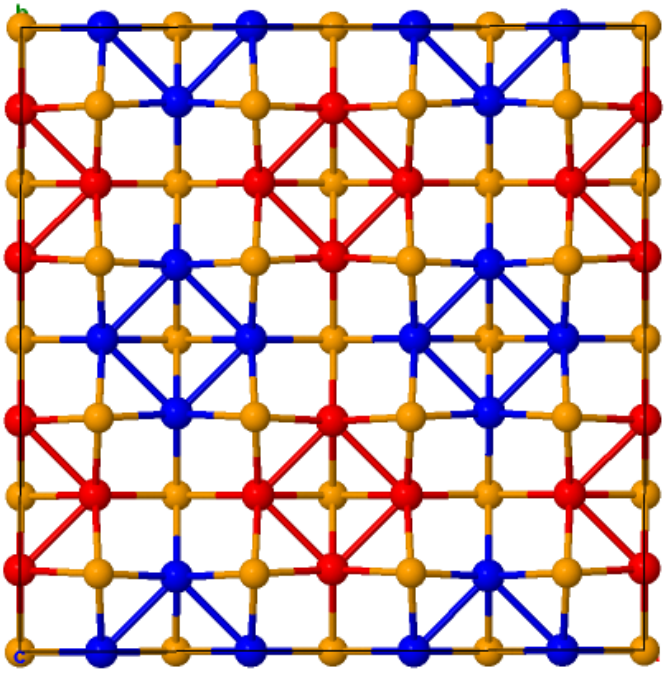

Figure 6.3: The BAFM′ structure proposed in reference [147] as the ground state to the 122 type systems. The Fe spin up and down sites are denoted by the red and blue atoms respectively while the Se atoms are shown in orange.

The magnetic excitations have been studied with INS in superconducting $Rb_{0.8}Fe_{1.6}Se_2$ [148], non-superconducting $Rb_{0.89}Fe_{1.58}Se_2$ [149] and superconducting $Cs_{0.8}Fe_{1.6}Se_2$ [150]. These studies found an acoustic and two higher-energy optic magnons, all of which can be attributed to the BAFM structure. In the superconducting samples a new magnetic excitation was observed to appear between 10 and 15 meV at a $\vec{Q}$ of $(0.25, 0.5, l)$ (l implying that it is not peaked along this direction). This "resonance" was observed to strengthen as the system became superconducting implying that it is in some way coupled to the superconductivity [150].

6.1.3 Lattice dynamics and symmetry breaking

Initial Raman scattering studies of the $K_{0.88}Fe_{1.63}Se_2$ system were able to identify 14 Raman active modes (as predicted by group theory analysis of the $\sqrt{5} \times \sqrt{5}$ cell) [151]. Other Raman and IR studies have, however, found a number of anomalies in the $\sqrt{5} \times \sqrt{5}$ phase on cooling. Measurements performed at 9 K on superconducting crystals of $K_{0.8}Fe_{1.6}Se_2$ found similar results to Ref [151] but with an additional 3 modes between 150 and 200 cm^{-1} [152]. These extra modes were attributed to a minority phase. However, this was not observed in powder x-ray diffraction measurements. Another Raman study of superconducting $K_{0.8}Fe_{1.6}Se_2$ observed only one extra mode, but as the system was cooled through the superconducting transition there were also anomalous shifts in both intensity and positions of the A_g modes associated with the FeSe layer [153].

The first IR measurements performed on $K_{0.83}Fe_{1.53}Se_2$ took place before consensus on the BAFM phase had been reached, and the authors were only able to conclude that their results were not consistent with a 122 type structure, but instead favoured the BAFM structure [154]. Other IR measurements did not focus on the lattice dynamics (although they did observe some at room temperature). Instead they probed the superconducting fraction [155] and found that the nature of the su-

perconductivity was fundamentally different from the other Fe superconductors (and even the bare FeSe system) which they attributed to the presence of the insulating BAFM phase [156].

A combined IR and Raman measurement did look purely at the lattice dynamics from a non-superconducting sample [157]. In this study a careful temperature dependence was performed which showed that at room temperature all modes could be attributed to the BAFM $I4/m$ structure. On cooling below 250 K several new modes appear which were argued to be associated with a symmetry-breaking phase transition from $I4/m$ to $I4$. The new modes were assigned to Se motion by comparison with first principles calculations performed with the BAFM structure. On this basis the authors concluded that the phase transition was a structural transition within the Se layers. They also observed a second transition at 150 K, which was not symmetry-breaking but instead corresponded to a change in the temperature dependence of the phonon intensities and gradients.

These two transitions are at very similar temperatures to those observed in a high pressure x-ray and resistivity measurement performed on superconducting and non-superconducting $K_yFe_{1.6+x}Se_2$ [158]. Their phase diagrams are shown in figure 6.4. It was found that the non-superconducting system underwent a transition from insulator to metal at between 200 and 250 K and then another from metal to insulator at just above 100 K. Unfortunately they did not take measurements at zero pressure, but it was found that the second transition was suppressed continuously until being destroyed when the $\sqrt{5} \times \sqrt{5}$ superstructure is also destroyed. In the superconducting sample the upper insulator to metal transition is seen at a reduced temperature with the lower temperature metal to insulator transition masked by the superconducting dome. The superconducting transition is also suppressed with increasing pressure, disappearing at the same pressure as the $\sqrt{5} \times \sqrt{5}$ phase. At higher pressures a second superconducting dome is observed to appear.

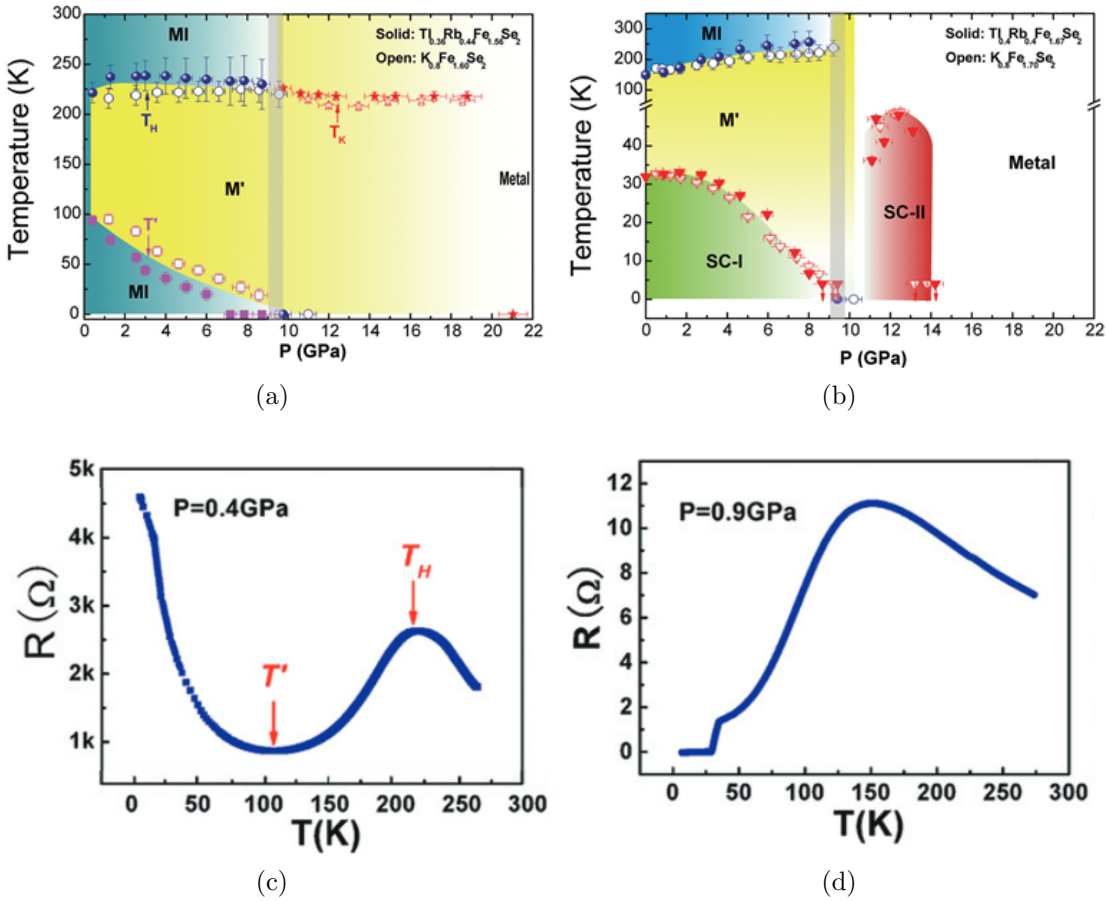

Figure 6.4: The high-pressure resistivity data for from Ref [158] with the plot rearranged for clarity. The vertical bar at 9 GPa shows the pressure at which the $\sqrt{5} \times \sqrt{5}$ phase was observed to be destroyed in their high pressure XRD measurements. (a) The bare $\sqrt{5} \times \sqrt{5}$ with the composition $K_{0.8}Fe_{1.6}Se_2$ and (b) containing a superconducting fraction with the total composition $K_{0.8}Fe_{1.7}Se_2$. The second compound shown is isostructural but with a mix of thallium and rubidium on the alkaline metal site. (c) A low pressure resistivity scan from the pure $\sqrt{5} \times \sqrt{5}$ sample showing the two transitions and (d) a similar scan on the superconducting system. Both (c) and (d) datasets are the mixed thallium and rubidium system.

The symmetry breaking has also been observed in powder inelastic neutron measurements [6]. These measurements were supported by first principles lattice dynamics calculations of the BAFM state, which gave reasonable agreement with the 300

K dataset. The authors were however unable to explain their low temperature data as anything other than the same Se distortions of Ref [157] despite considering calculations for non-magnetic $I4/m$ and a magnetic system which fell into the space group $Fmmm$.

There has been some discussion of electron-phonon coupling in the literature. Ref. [157] found Fano type lineshapes for some Fe modes while in Ref. [6] the phonon lineshapes were found to be extremely broad by comparison to equivalent measurements on the 122 $BaFe_2As_2$ system, and this was attributed to static disorder in the Fe layer.

6.2 Computational Procedure

Single-crystal diffraction data obtained by Dr D.G. Porter and Mr E. Cemal on a superconducting sample of nominal composition $Cs_{0.8}Fe_{1.6}Se_2$ found that both the $\sqrt{5} \times \sqrt{5}$ and $\sqrt{2} \times \sqrt{2}$ phase were present. By refining the two principal Bragg components individually they were able to show that the $\sqrt{5} \times \sqrt{5}$ phase has a composition approximately $CsFe_{1.6}Se_2$ and $\sqrt{2} \times \sqrt{2}$ phase $Cs_{0.5}Fe_2Se_2$. Using these refinements as a starting assumption for the composition of the two phases, calculations have been performed to investigate three results in the literature. These are the shift of lattice parameters between the two phases, the origin of the disorder along $\vec{c}$, and the symmetry-breaking in the $\sqrt{5} \times \sqrt{5}$ phase.

6.2.1 Exchange, correlation and pseudopotentials

The GGA was used for all calculations in this chapter, in particular the approach of Perdew, Burke, and Ernzerhof [62]. The default CASTEP 7.0 ultrasoft pseudopotentials have been used for all elements.

6.2.2 DFT+U in the $\sqrt{5} \times \sqrt{5}$ phase

Previous calculations within the GGA on the electronic properties of $K_yFe_2Se_2$ have found that for $y \neq 0.8$ the system is metallic [159]. As the physical properties measurements under pressure show that the lowest temperature state of the $\sqrt{5}\times\sqrt{5}$ phase is insulating [158] and the crystallographic refinements show $y = 1$ then within the GGA the system will emerge as metallic. For this reason a Hubbard-U was required to reproduce a band gap in the $\sqrt{5} \times \sqrt{5}$ phase.

To investigate the system within the insulating phase a Hubbard U was applied to the iron $3d$ states. It was found that a U of 2, 3 or 4 eV yielded identical results although the electronic convergence at 4 eV was somewhat challenging. For reasons of electronic convergence a U of 2 eV was used in the main calculations. This produces a band gap of approximately 250 meV compared to the experimental gap of 430 meV [160]. The band structures are shown in figure 6.5.

6.2.3 Plane-wave convergence

Initial convergence tests were performed on a unit cell of $CsFe_2Se_2$. The system was found to be converged with respect to energy to within 1 meV/atom by a plane-wave cut-off of 400 eV. When this cut-off was applied to the $\sqrt{5} \times \sqrt{5}$ phase the energy was found to change non-variationally with the Hubbard U applied (this was due to changes in the magnetic ground state). Variational behaviour was not regained until a cut-off of 550 eV which was found to give better energy convergence than was seen at 400 eV as well as forces which were converged to within 0.0015 eV/$\mathring{A}$. This cut-off was also found to be adequate for the $\sqrt{2} \times \sqrt{2}$ phase and was utilised for comparisons between the two. This cut-off was also found to be satisfactory for calculations on the potassium system.

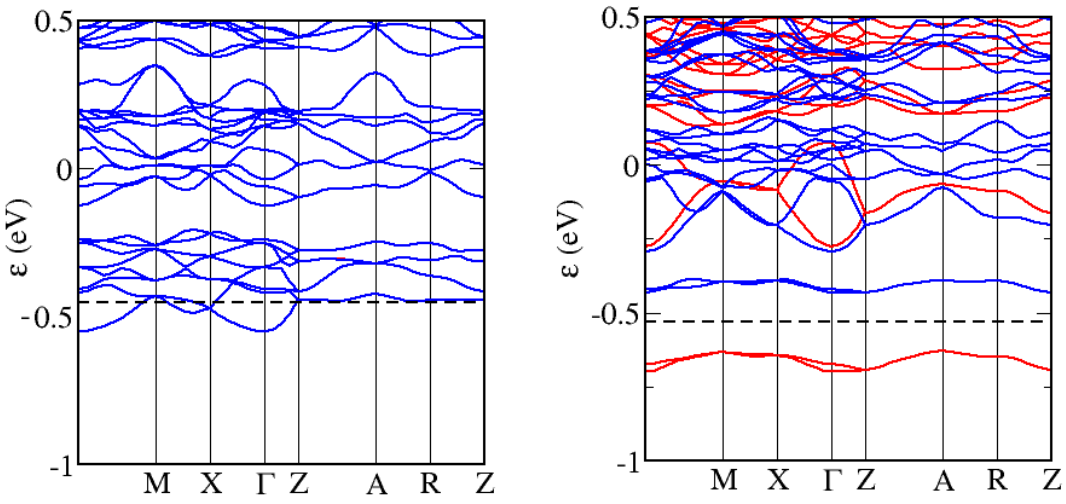

(a) (b)

Figure 6.5: The computed band structures of $KFe_{1.6}Se_2$ with $U = 0$ eV (a) and $U = 2$ eV (b). The Fermi level is denoted by the dashed line. Note the gap which is opened by the application of the Hubbard U and the difference between spin up and down electrons due to a change in magnetic structure.

6.2.4 Brillouin zone sampling

For the $\sqrt{2} \times \sqrt{2}$ phase very fine convergence of less than 0.1 meV/atom and 0.001 eV/$\mathring{A}$ was obtained for a k-point grid of $8 \times 8 \times 4$ in a supercell of parameters

$$\vec{a'} = 2\vec{a}$$

$$\vec{b'} = 2\vec{b}.$$

The larger cell was employed so that the magnetic ground state of BAFM could be used. It was confirmed as part of the testing for this system that the BAFM state was the lowest energy of those surveyed (a ferromagnetic, ferromagnetic-in-plane while antiferromagnetic between planes and an antiferromagnetic with respect to all neighbours system were all investigated).

In the case of the the $\sqrt{5}\times\sqrt{5}$ phase a grid of $6\times6\times4$ was found to converge the system to within an energy 0.2 meV/atom and force of 0.003 eV/$\mathring{A}$ on each atomic site.

6.2.5 Other parameters

In all the calculations a number of parameters have been converged to a similar level as above and used in all calculations. The smearing width for metallic calculations was 0.05 eV with Gaussian smearing. The standard grid was increased to $2.0\times E_{\text{cut}}$ while the fine grid was set to $4.0\times E_{\text{cut}}$.

6.2.6 Phonon calculations in the $\sqrt{5}\times\sqrt{5}$ phase

Lattice dynamics in the $\sqrt{5}\times\sqrt{5}$ phase were computed using the finite-displacement/supercell method [78, 79]. Initially the positions were geometry-optimised with the low memory BFGS (LBFGS) method [130, 131] such that the residual forces were less than 0.005 eV/Å. The supercell used was a 2x2 cell of the non-primitive I centred lattice with $|a| = 17.65$ Åfor the caesium system (using the experimentally determined lattice parameters at 30 K). Two calculations were performed with and without the Hubbard-U to investigate its effect on the lattice dynamics. These calculations were then repeated for the K system using the lattice parameters from Ref. [6].

6.2.7 Cell optimisations and ordering energetics

In order to compare the calculated lattice parameters to experiment, variable cell geometry optimizations were again performed using the LBFGS method. For the $\sqrt{5}\times\sqrt{5}$ phase calculations the cell was optimised with a Hubbard U applied and the CASTEP spin_fix keyword used to enforce the BAFM state. This was then released to investigate the effect of the changing magnetic state on the lattice parameters.

The $\sqrt{2} \times \sqrt{2}$ phase was optimised in the BAFM structure with no Hubbard U applied.

For the calculations of the ordering energetics 4 calculations were performed using the geometry optimised primitive lattices as a starting point. The first looked at the in-plane orderings by calculating the energy of an ideal structure with a tetragonal cell of base $\vec{a'} = 4\vec{a}$ and $\vec{c'} = \vec{c}$. The second displaced a single Cs ion into an unoccupied site. This is shown in figure 6.6a. To investigate interlayer ordering energies a double height cell (with 4 layers) was used. The two stacking structures were ABAB and ABCD with the sites shown in figure 6.6b.

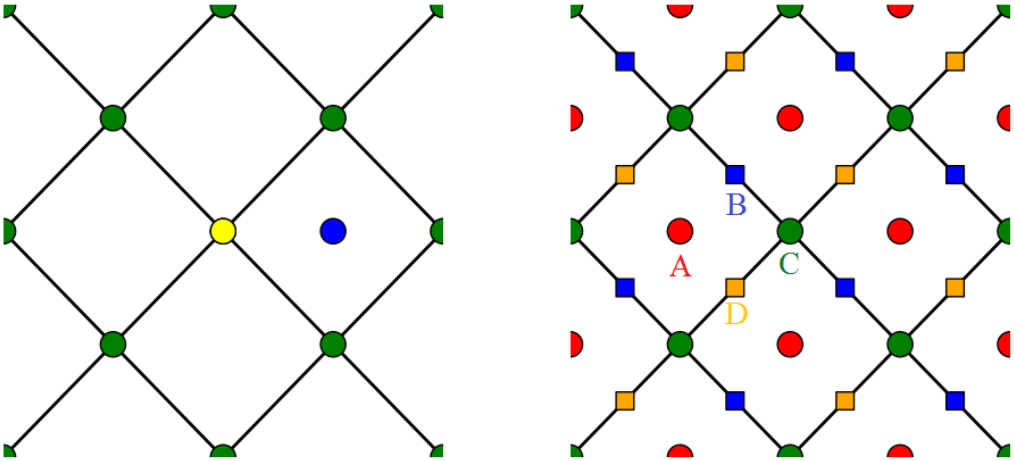

(a) (b)

Figure 6.6: (a) A single layer of Cs sites as proposed by D.G. Porter and E. Cemal. The yellow site ion is the Cs which was moved to the originally empty blue site when investigating the intralayer energetics. The black lines show the underlying $\sqrt{2} \times \sqrt{2}$ unit cell. (b) The different sites for each layer. The circles show the two different possibilities for the first layer and the squares the second layer.

6.3 Results

6.3.1 Symmetry breaking in the $\sqrt{5} \times \sqrt{5}$ phase

The standard GGA calculation of the BAFM phase yielded a system which was metallic as would be expected from a simple analysis of ionic charge states. A moment of 3.22 μ_B was obtained on each iron site for the Cs compound and 3.20 μ_B for K (from a Mulliken type analysis). The application of a 2 eV Hubbard U led to an increase in the average moment to 3.4 and 3.38 μ_B respectively. As well as this moderate increase in total moment (due to a slight increase in the net charge on the Fe sites) there was also a splitting of the moment between the spin up and spin down sites. This splitting corresponds exactly to one extra μ_B associated with either the up or down direction (we will use the convention that the extra spin is on the up sites) spread across a block of 4 Fe sites. This splitting leads to a ferrimagnetic ground state which also lowers the symmetry from $I4/m$ to $I4$. The two structures are shown in figure 6.7.

Geometry optimisation

Both the Cs and K systems were geometry-optimised in both the BAFM and ferrimagnetic states. The lattice parameters were fixed at their experimentally observed values and some key parameters are reported in table 6.1. The decrease in lattice parameters between the Cs and K systems is shared between both the in-block (e.g. $(\uparrow) - (\uparrow)$) and between-block ($(\uparrow) - (\downarrow)$) bond distances. The Fe blocks sit a little out of the 1/4 type positions leading to a structure which looks corrugated, with the amplitude of this corrugation being much more pronounced in the ferrimagnetic phase. It is perhaps this increased corrugation which allows for the net increase in the in-block bond lengths. There is a larger increase in the in-block bond lengths

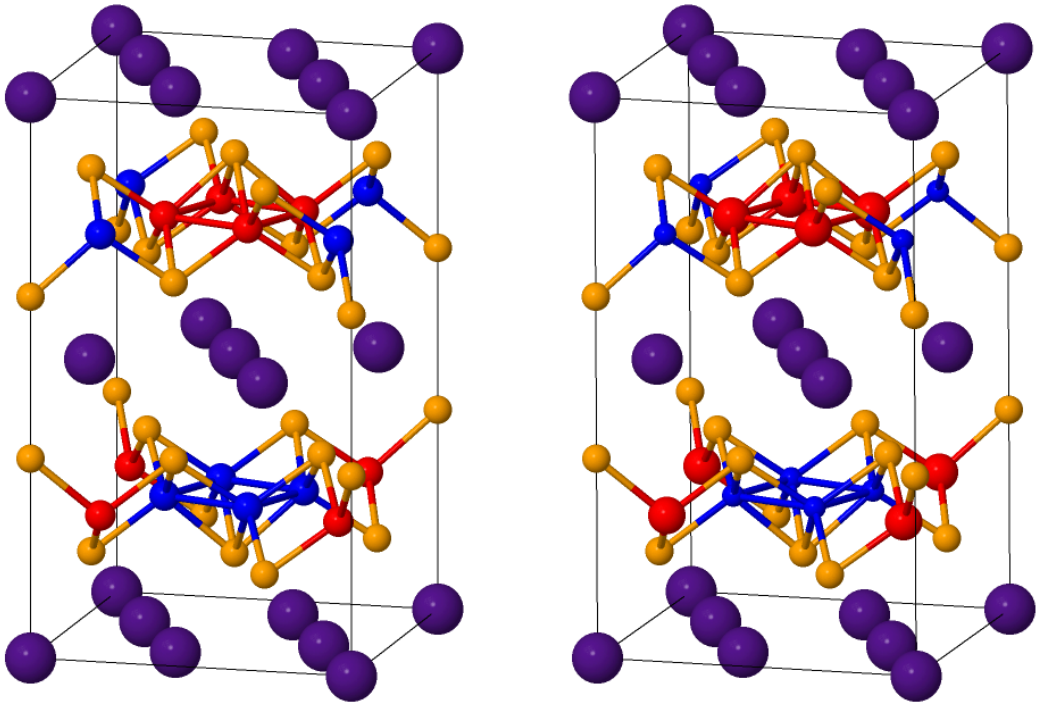

(a) (b)

Figure 6.7: The calculated magnetic structures for (a) the BAFM and (b) the ferrimagnetic structure. The alkaline metal is shown in purple, Se as orange and the two different spin states of Fe as red and blue respectively. The Fe ionic radius has been scaled to show where the extra moment sits although the changes have been exaggerated for clarity.

for the $\downarrow$ sites presumably due to the decrease in electrons increasing the Fe-Fe repulsion. The Se sites do not move relative to the origin of the cell and thus there is a net change in the Fe-Se1 bond lengths. These actually increase as the displacement along z is smaller than the increased in-block bond lengths. There is also a difference in the Fe-Se bond lengths between the $\uparrow$ and $\downarrow$ which would be expected to lead to a difference in the lattice dynamics between the sites.

	Cs BAFM	Cs Ferri	K BAFM	K Ferri
a'	8.8262 $\mathring{A}$	8.8262 $\mathring{A}$	8.7308 $\mathring{A}$	8.7308 $\mathring{A}$
c'	15.2401 $\mathring{A}$	15.2401 $\mathring{A}$	14.113 $\mathring{A}$	14.113 $\mathring{A}$
Fe ($\uparrow$) x	0.19170	0.19171	0.19173	0.19285
Fe ($\downarrow$) x	0.19170	0.19393	0.19173	0.19511
Fe ($\uparrow$) y	0.09295	0.09145	0.09271	0.09167
Fe ($\downarrow$) y	0.09295	0.09094	0.09271	0.09087
Fe ($\uparrow$) z	0.24904	0.24703	0.24959	0.24558
Fe ($\downarrow$) z	0.75096	0.75331	0.75041	0.75472
Se1 ($\uparrow$) z	0.35582	0.35746	0.36782	0.36717
Se1 ($\downarrow$) z	0.64418	0.64642	0.63218	0.63707
Fe ($\uparrow$)-Fe ($\uparrow$)	2.6593 $\mathring{A}$	2.6513 $\mathring{A}$	2.6187 $\mathring{A}$	2.6251 $\mathring{A}$
Fe ($\downarrow$)-Fe ($\downarrow$)	2.6593 $\mathring{A}$	2.6736 $\mathring{A}$	2.6187 $\mathring{A}$	2.6460 $\mathring{A}$
Fe ($\uparrow$)-Se1 ($\uparrow$)	2.4867 $\mathring{A}$	2.51927 $\mathring{A}$	2.4856 $\mathring{A}$	2.5200 $\mathring{A}$
Fe ($\downarrow$)-Se1 ($\downarrow$)	2.4867 $\mathring{A}$	2.4956 $\mathring{A}$	2.4856 $\mathring{A}$	2.4940 $\mathring{A}$
Fe ($\uparrow$)-Fe ($\downarrow$)	2.9573 $\mathring{A}$	2.9810 $\mathring{A}$	2.9177 $\mathring{A}$	2.9293 $\mathring{A}$

Table 6.1: The fixed-cell geometry-optimised parameters for each of the $\sqrt{5} \times \sqrt{5}$ systems. Differences between the BAFM and Ferrimagnetic systems are the result of the different magnetic moment rather than numerical noise which becomes apparent at the 6^{th} decimal place. The Wyckoff positions of each of the sites in $I4/m$ is Fe $16i$ (x, y, z) and Se1 $4e$ $(0, 0, z)$. Se1 sits at the centre of a block of 4 Fe with the same spin, and the arrows indicate if it is a spin up or down block.

Lattice dynamics

Calculations of the lattice dynamics were performed on both systems to see if this ferrimagnetism was consistent with the symmetry-breaking reported in the literature. The calculations on $KFe_{1.6}Se_2$ are directly comparable to those in the literature while those for Cs will be compared to future single crystal INS measurements of E. Cemal. The calculated partial DOS and combined neutron weighted DOS are shown in figure 6.8. In the K calculations there is a large shift in the K DOS which is not seen for the Cs compound. The main peak for K moves from 11.0 to 13.5 meV which, as the K is not directly bound to the Fe atoms is unexpected. However, this can be understood in three ways. First, the K motion here is principally along

$\vec{c}$ and the contraction of the lattice parameters causes a stronger coupling between K and the Fe-Se layer. Second, the lighter K ions have a larger amplitude motion than the Cs. Finally, these modes involve the Se atoms due to their large motion along $\vec{c}$. This is much less clear in the Se DOS as the Se ions are coupled into almost every mode in the system. Consequently these modes make up a small component of their DOS.

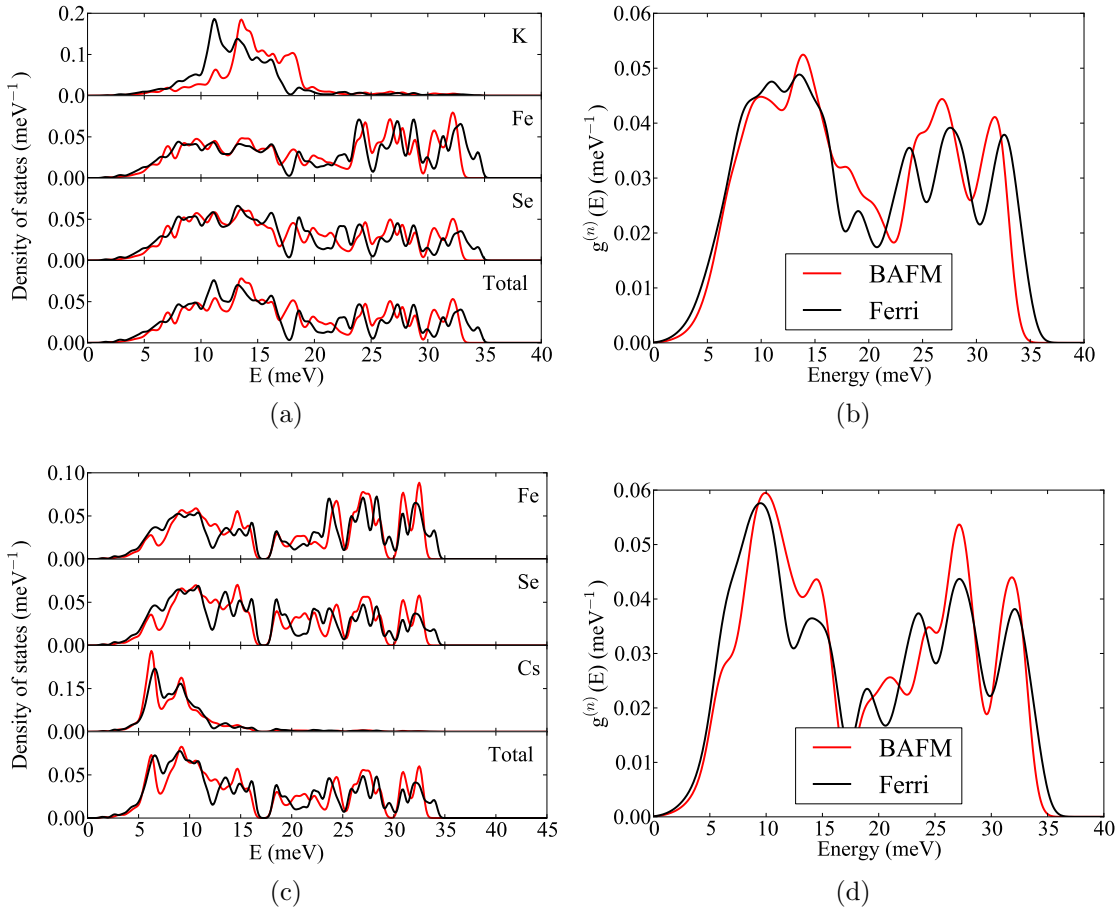

Figure 6.8: The calculated DOS and neutron-weighted DOS for the ferrimagnetic and BAFM state of $KFe_{1.6}Se_2$ and $CsFe_{1.6}Se_2$. (a) $KFe_{1.6}Se_2$ partial DOS, (b) $KFe_{1.6}Se_2$ neutron-weighted DOS, (c) $CsFe_{1.6}Se_2$ partial DOS and (d) $CsFe_{1.6}Se_2$ neutron-weighted DOS. The neutron-weighted DOS have been broadened by a Gaussian with FWHM of 2meV.

The ferrimagnetism induces moderate changes at all energies in the Fe and Se modes and produces large overall changes in the neutron-weighted DOS given the small change in moment between the two sites. Looking in more detail at the modes which could become Raman active between the two phases the most obvious candidates are those involving the Se. An example for the K system is shown in figure 6.9. In the BAFM the bond lengths are elongated and shortened by the same amount leading to no change in the overall polarization of the material. In the ferrimagnetic case there is a difference in the changes of the bond length which would change the overall polarization of the material and could be expected to be Raman active. A proper test of this would be to compute the Raman intensities, however, this would only be possible in the ferrimagnetic case as the BAFM is metallic and, as norm-conserving pseudopotentials would be required, it would be much more expensive.

6.3.2 Lattice parameters

The optimised lattice parameters are shown in table 6.2. There is very little difference between the BAFM and ferrimagnetic calculations, suggesting that the ferrimagnetism would not manifest itself in an observable change in the lattice parameters. The calculated shifts between the proposed Fe and Cs vacancy structures are in the correct direction, however, the magnitude is much larger than those observed experimentally. The agreement between experiment and calculation is within 4% for the $\sqrt{5} \times \sqrt{5}$ phase, however, the difference is greater at 7% for the $\sqrt{2} \times \sqrt{2}$ phase. Furthermore, the calculated change in the lattice parameters between the two phases is 10% and this is significantly greater than the 2% observed experimentally.

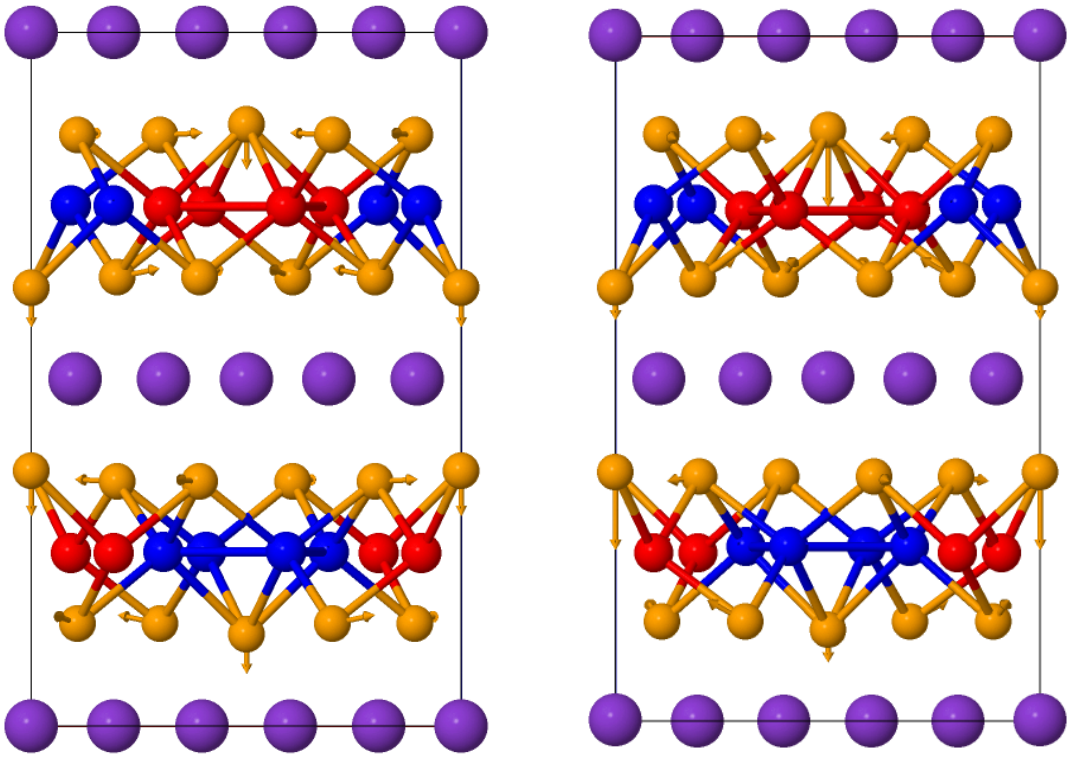

(a) (b)

Figure 6.9: (a) An A_g mode at 173 cm^{-1} in the BAFM state. (b) A similar A_g mode at 178 cm^{-1} in the ferrimagnetic state. A mode identified as belonging to the Se ions in Ref. [157] which becomes active across the transition is found at 165 cm^{-1}. In the BAFM calculations this mode would not be Raman active as there is no net change in bond lengths. In the ferrimagnetic case the Se coupled to the spin-up Fe sites has a much larger displacement which could cause this mode to become Raman active.

6.3.3 Ordering energetics

The two calculations performed for the vacancy energetics were to look at the in-plane and inter-plane ordering energies. The difference between the perfectly ordered structure and that with one Cs ion displaced was found to be 851 meV. Most of this large increase is attributable to simple Coulombic repulsion. In the ground state a

System	a (Å)	c (Å)	γ
$\sqrt{5}$ experimental	3.9472(2)	15.24009(3)	90°
$\sqrt{2}$ experimental	3.85535(1)	15.4931(5)	90°
$CsFe_{1.6}Se_2$ BAFM	4.0945	15.0138	90°
$CsFe_{1.6}Se_2$ Ferri	4.0979	15.0105	90°
$Cs_{0.5}Fe_2Se_2$	3.7901	16.5419	89.77°

Table 6.2: The experimental lattice parameters at 30 K for the two phases of $Cs_{0.8}Fe_{1.6}Se_2$ provided by Dr D.G. Porter and the variable cell geometry optimised lattice parameters of $Cs_{0.5}Fe_2Se_2$ and $CsFe_{1.6}Se_2$ in the BAFM and ferrimagnetic phases.

Cs ion has a nearest neighbour bond length of 5.36 $\mathring{A}$ while a displaced Cs has 3 nearest neighbours at a distance of 3.8 $\mathring{A}$. This leads to an increase in energy of 0.62 eV. The remaining changes are likely to be due to next nearest neighbours and subtle changes in the magnetism of the system. Hence this large stabilisation energy would be expected to result in Cs vacancy ordering within the plane.

In contrast the two different stacking sequences proved to be extremely close in energy, with only 1.5 meV separating them. This is very small (although larger than the convergence criteria of the calculation). It would be surprising if the heavy Cs ions were still mobile and able to order at this low temperature, it is more likely that by this point the interplanar disorder has frozen in, explaining the rods of scattering along l.

6.4 Discussion

The calculations of ordering energies and lattice parameters in the $\sqrt{2}\times\sqrt{2}$ phase are in qualitative agreement with experiment. The ordering energies show that alkaline metal vacancies order in-plane, but that these superstructures are not correlated between planes. This could be responsible for the disorder along $\vec{c}$ observed in

x-ray measurements [145]. Unfortunately the calculation of lattice parameter shift between this phase and the $\sqrt{5}\times\sqrt{5}$ phase is much larger than occurs experimentally. This may be due to the BAFM structure assumed in the calculation of the Cs vacancy structure. Previous studies have found a strong dependence on the magnetic state used [147] and polarized neutron measurements have failed to find any magnetic order associated with the $\sqrt{2}\times\sqrt{2}$ phase [141]. It is not easy to model a paramagnetic structure within DFT as this would require a very large number of atoms to capture the disordered nature. All that can really be said is that the lattice parameter shifts are in the correct direction, which is reassuring, although the absolute magnitude is not observed experimentally. The reproduction of a small monoclinic distortion is comparable to that seen in high resolution x-ray measurements [145] although further calculations would need to be performed to quantify the error bars on this parameter.

The ferrimagnetic calculations of the $\sqrt{5}\times\sqrt{5}$ phase are interesting in the context of the observed symmetry-breaking. As already discussed, the ferrimagnetic phase would allow for certain selenium A_g modes to become Raman active, and they sit relatively close to those which are observed in Ref. [157]. A comparison of the neutron-weighted DOS for K to that measured in Ref. [6] is offered in figure 6.10. The agreement is reasonable with most of the key features reproduced. The agreement could be artificially increased by attempting to take account of the shift in phonon frequencies from cell contraction as the system is cooled. This leads to a change of around 3% on average [157]. The two main peaks' total width is expanded in the ferrimagnetic calculation and the pronounced dip just below 20 meV is also present. The only missing feature in the calculation is the peak observed at 30 meV. The origin of this discrepancy is not presently understood. However, the overall agreement between experiment and calculation is encouraging.

The transition to the ferrimagnetic ground state could also explain the observed

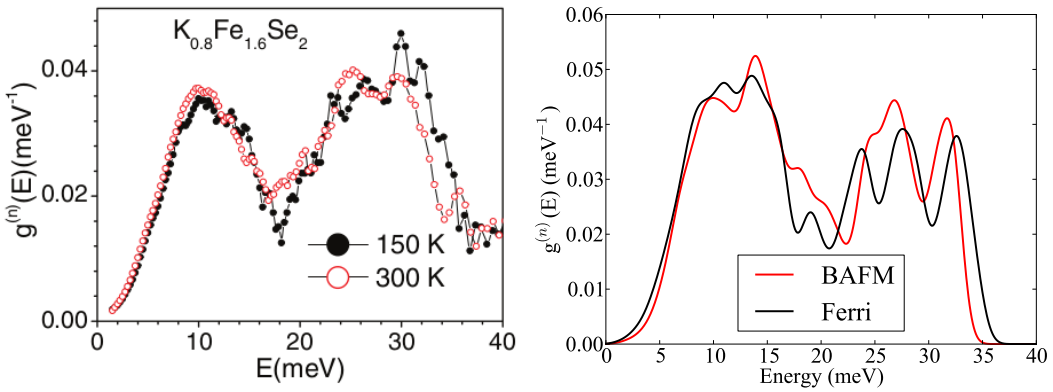

(a) (b)

Figure 6.10: (a) The neutron-weighted DOS measured in Ref. [6] at 300 and 150 K. (b) The neutron-weighted DOS calculated for $KFe_{1.6}Se_2$ in both the BAFM and ferrimagnetic state.

metal-insulator transition in high pressure data [158] as the BAFM state is metallic and the ferrimagnetic is insulating.

The idea of a magnetic transition in this compound is not entirely without precedent. The $\sqrt{5}\times\sqrt{5}$ structure is also observed in the non-superconducting compound $TlFe_{1.6}Se_2$ [142]. This has been observed to undergo a 2-stage magnetic phase transition [161]. The high-temperature phase is BAFM, at 140 K it develops a canted moment structure, and at at 100 K the authors suggest it returns to the BAFM structure but with a reduced total moment. The refinements also assumed that it maintained the $I4/m$ space group which, if it is related to the symmetry-breaking phase transition may not be correct. There was a noticeable change in the corrugation of the Fe layer. It was doubled at the 140 K transition before returning to its approximately original value at 100 K. At each transition the Se1 sites remained approximately constant (within the rather large error bars). Detection of a ferrimagnetic moment only along $\vec{c}$ would only be possible with an external magnetic field to drive the system single domain (as well as needing to refine the system within I4).

Scanning tunnelling microscope measurements have suggested that the mag-

netism and superconductivity are in some form of "symbiotic relationship" [138] while high pressure-measurements show that the metal insulator transition in the $\sqrt{5} \times \sqrt{5}$ phase is suppressed in a similar way to the superconductivity, with both being destroyed at the same pressure [158]. Furthermore the IR measurements show that superconductivity in the alkaline metal iron selenides is fundamentally different from that of all other iron superconductors [155]. It has previously been shown that cuprate superconductors can have their transition temperature increased by thin film growth in contact with the Ba doped ferroelectric $SrTiO_3$ [162]. Very recently FeSe grown on Nb doped $SrTi_3$ thin films has resulted in an order of magnitude increase in their transition temperature from 8 to 109 K (Nb doped $SrTi_3$ has a ferroelectric transition of 104 K) [163]. The ferrimagnetic phase would be expected to be weakly ferroelectric (and in Ref. [157] it is stated that the I4 phase is). It is perhaps the interaction between this and the superconducting fraction which leads to the change in its nature and the increase in the transition temperature from 8 K in FeSe to 30 K in the 245 class of superconductors.

6.5 Conclusions

The composition of the $\sqrt{2} \times \sqrt{2}$ phase in $Cs_{0.8}Fe_{1.6}Se_2$ has been suggested to be $Cs_{0.5}Fe_2Se_2$ on the basis of single crystal refinements. Using this as a starting point the ordering energetics have been investigated and have shown that a Cs vacancy structure is consistent with ordering in $a - b$ with disorder along c. Geometry optimisations of the lattice parameters for this phase, however, were promising although due to strong magnetoelastic interactions it was not possible to reproduce the exact experimental shifts. A small monoclinic distortion which agrees with that observed in high resolution x-ray diffraction [145] was reproduced.

The symmetry-breaking phase transition observed in the $\sqrt{5}\times\sqrt{5}$ phase has been

explained in terms of a ferrimagnetic phase transition. This ferrimagnetism is able to explain the appearance of several new Raman active modes, a metal-insulator phase transition and powder inelastic neutron scattering data. A knowledge of the structure and magnetic state for both the $\sqrt{2} \times \sqrt{2}$ and $\sqrt{5} \times \sqrt{5}$ phase is vital to understand the origin of the superconductivity in this class of superconductors and it is hoped that this work will enable a theoretical model to be developed in the future.

Chapter 7

Summary and future outlook

In this thesis two main areas have been covered. In the case of thermoelectrics it has been shown that rattling modes exist within the potential thermoelectric Na_xCoO_2 by combining first-principles lattice dynamics calculations with momentum resolved spectroscopy. This rattling mode was found at 13 meV but it was not accompanied by significant phonon-phonon scattering. Instead it was found that the flat nature of the rattling modes in reciprocal space suppressed the phonon group velocity and that this reduced the overall thermal conductivity by a factor of 6.

Measurements of the stripe arrangement of trivacancy clusters found a subtle change in the neutron weighted phonon DOS and a corresponding change in the lattice thermal conductivity. The divacancy Ca doped structure however led to a much larger increase in the thermal conductivity. While this means that $Na_{0.57}Ca_{0.14}CoO_2$ is not an ideal thermoelectric material it shows that changing the rattling mode environment can significantly change the lattice thermal conductivity.

This has implications for other rattler materials, namely the clathrates and skutterudites in that it may not be possible to design simple guidelines for doping. Instead more comprehensive computational studies of possible rattlers and their effect on the phonon velocities should be carried out to inform the design of future

materials, where necessary supported by momentum resolved spectroscopy.

This combined approach is applicable to other classes of thermoelectrics as well. For example, the compound Cu_2Se displays a liquid-like specific heat ($c_v = 2K_BT$) at temperatures above 800K, which it has been suggested is responsible for its observed low thermal conductivity [164]. A combination of lattice dynamics calculations, momentum resolved spectroscopy measurements and quasi-elastic neutron scattering [33] (a neutron technique where the self-correlation function of ions can be probed) would be able to measure the emergence of liquid-like behaviour if it exists and relate it back to the thermal conductivity.

The second area studied was that of the new iron chalcogenide superconductors. It was shown that alkaline metal vacancies were a possible origin for $\sqrt{2} \times \sqrt{2}$ phase by looking at their ordering energies. A symmetry breaking transition within the $\sqrt{5} \times \sqrt{5}$ phase was then explained in terms of a ferrimagnetic phase transition. This transition explained a number of results within the literature (metal-insulator phase transition, Raman and powder inelastic neutron scattering data) purely computationally. It is obviously a requirement that this be measured experimentally. This would involve two elements, the first a single-crystal phonon measurement to show that the transition also exists in $CsFe_{1.6}Se_2$ and a polarized neutron scattering measurement. A polarized elastic neutron measurement would allow (with the application of a small external field to drive the system single domain) a ferrimagnetic component to be detected unambiguously in the $(h, k, 0)$ plane. It would be interesting to perform these measurements for both insulating and superconducting samples, since the phase diagrams appear to be rather different.

This approach is, however not limited to the iron chalcogenides. The sensitivity of lattice dynamics to subtle changes in the electronic structure and the ability to use computational models to interpret the data makes them very powerful and versatile. This has already been successful in the cuprate superconductors to probe

charge density wave formation [165]. In the future, given the ability to reach high pressures with a diamond anvil cell, inelastic x-ray scattering studies could prove interesting in the emergence of complex electronic effects without the complication of doping.

Appendix A

Symmetry operators and notation

The symmetry operators mentioned in the experimental methods chapter and their notation is discussed here in more detail. The aim is not to replace the full discussion given in the international tables but instead to facilitate an understanding of the work presented without reference to them.

Mirror planes

An object has mirror (or reflection) symmetry if we can define a plane such that a point which lies on a vector normal to the plane has an equivalent point at the negative of this vector. This is simplest to see if we consider a two dimensional system. If we have a mirror perpendicular to x then any point at $+x$ must have an equivalent point at $-x$. In three dimensions we can define our plane as $ax + by + cz + d = 0$ where the normal to the plane is $\vec{n} = (a, b, c)$. If we define our initial point to be (x_0, y_0, z_0) and recalling that the distance from a plane to a point (D) is

$$D = \frac{ax_0 + by_0 + cz_0 + d}{\sqrt{a^2 + b^2 + c^2}}$$

then our reflected point (x_0', y_0', z_0') will be [166]

$$\begin{bmatrix} x_0' \\ y_0' \\ z_0' \end{bmatrix} = \begin{bmatrix} x_0 \\ y_0 \\ z_0 \end{bmatrix} - \frac{2(ax_0 + by_0 + cz_0 + d)}{\sqrt{a^2 + b^2 + c^2}} \begin{bmatrix} a \\ b \\ c \end{bmatrix}.$$

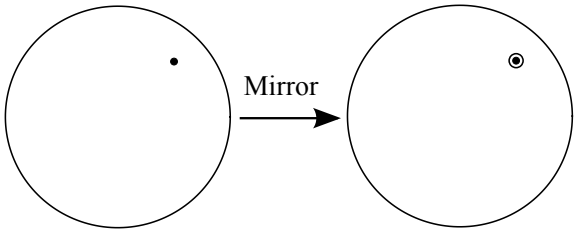

Figure A.1: A stereographic projection of a mirror operation acting on a single point. The mirror sits in the plane of the paper and thus only affects the z component which is represented here by the filled circle turning into an empty circle.

Rotation axes

Rotational symmetry is defined by a point coming into contact with an equivalent point after a rotation by $^{2\pi}/_{n}$. n is used to describe the rotation axis. For example a cube being rotated about the middle of one of its faces will come into coincidence with itself after a $^{\pi}/_{2}$ rotation ($n = 4$). This is known as a four-fold rotation axis. In standard crystallography only 2,3,4 and 6 fold rotations are allowed. The rotation of a vector $\vec{r}$ about a unit vector $\hat{n}$ is expressed as

$$\vec{r'} = \vec{r}\cos\phi + \hat{n}(\hat{n} \cdot \vec{r})(1 - \cos\phi) + (\vec{r} \times \hat{n})\sin\phi,$$

where ϕ is the angle of rotation (in a counter clockwise direction) and $\vec{r'}$ the rotated vector [167].

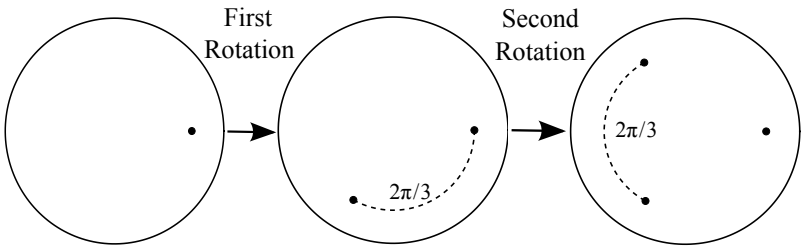

Figure A.2: A stereographic projection of a 3-fold rotation axis. Each point is mapped out by rotating the previous point by $^{2\pi}/_{3}$.

Inversion symmetry

A system has inversion symmetry (or a centre of inversion) if a point at (x, y, z) has an equivalent point at $(-x, -y, -z)$. A crystal with a centre of inversion is known as centrosymmetric and this is important for many properties such as ferroelectricity [39].

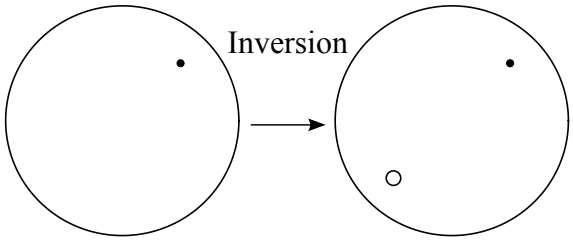

Figure A.3: A stereographic projection of an inversion operation. The point is moved from (x, y) to $(-x, -y)$ and the z inversion is represented by the change from filled to empty circle.

Rotoinversion axes

A rotoinversion is a composite symmetry operator consisting of a rotation and inversion. The first stage is one step of the n-fold rotation and then the inversion

operator is applied to obtain the actual point. A tetrahedron is an example of a system with such an axis (a 4-fold rotoinversion axis through the edges).

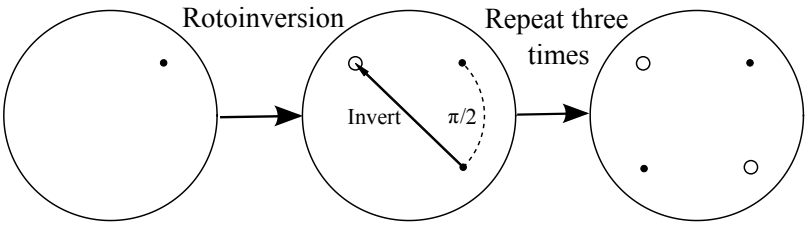

Figure A.4: A stereographic projection of the 4-fold rotoinversion axis of a tetrahedron. Our initial point undergoes a combined rotation by $\pi/2$ and then immediately an inversion.

Glide planes and screw axes

There exist two other type of symmetry operators which are useful in crystallography. The first is a glide plane, where there is a reflection followed by a translation in the plane of the mirror. The second is a screw axis, in this operator there is a combined rotation and translation with the translation occurring along the axis of rotation.

Notation

It is cumbersome to express a system which may (for example) have a rotation axis, several mirror planes and a screw or glide plane by writing them all out in longhand. The shorthand notation used throughout this thesis is described in table A.1 including combinations of operators (for example a combined rotation with a perpendicular mirror plane). There are several levels of detail into which we can go when describing the symmetries within a crystal. The most coarse is to classify it within one of the 7 crystal systems, outlined in table A.2. Within these 7 systems there are,

in total 14 Bravais lattices. Each system has a primitive lattice were an atom sits at (0,0,0) type position but there are also body-centred (orthorhombic, tetragonal and cubic with an additional atom at $(1/2, 1/2, 1/2)$), face-centred (orthorhombic and cubic with extra atoms in the middle of each face, for 3 extra in total) and c-centred (monoclinic and orthorhombic with an atom in the middle of the face defined by a and b.).

There are then 32 different possible combinations of the symmetry operators (rotations, mirror planes, inversion and rotoinversions) which can act upon the Bravais lattices to give the point group of a crystal. The inclusion of glide planes and screw axes gives the space group of which there are 230 in total. As only two principal systems are studied in this thesis, these are not all listed and explained here, however the interested reader is once again referred to the international tables [33]. It should be mentioned that sometimes the trigonal group is misclassified as rhombohedral. The rhombohedral group is in fact a subset of the trigonal group where the 3-fold axis lies along the body diagonal of the cell.

In this notation the two systems considered in this thesis have the following labels. A unit cell of $NaCoO_2$ is $P6_3/mmc$ implying that is has a 6-fold axis of rotation with a perpendicular mirror plane and a 1/2 translation screw axis. It also has one additional mirror plane and a 1/2 translation glide plane along $\vec{c}$. The unit cell of $CsFe_2Se_2$ is $I4/mmm$. I stands for body centred (i.e. every atom has an equivalent point at a translation of the cell $(\frac{1}{2}, \frac{1}{2}, \frac{1}{2})$). $4/m$ shows that there is a 4-fold rotation with a perpendicular mirror plane and mm two further orthogonal mirror planes (that there are 3 mirror planes in total forces them all to be orthogonal).

Operator	Notation	Example	Explanation
Rotation	n	3	A threefold axis of rotation
Mirror	m	m	The system has a mirror plane
Rotation with a perpendicular mirror plane	n/m	$4/m$	There exists a 4-fold axis of rotation with a mirror plane perpendicular to it (this example would generate 8 points)
Inversion (only)	$\bar{1}$	N/A	The system is centrosymmetric with no other symmetry
Rotoinversion	$\bar{n}$	$\bar{4}$	This notation is for the 4-fold rotoinversion axis of the tetrahedron shown in Fig A.4.
Screw Axes	n_x	6_3	n here is the same as for the axes of rotation however the subscript x relates to the translation distance. This distance is given by x/n multiplied by the lattice parameter that the screw axes lies along. In the example 6_3 this would be a $\pi/3$ rotation followed by a $1/2$ lattice parameter translation.
Glide Plane	a, b, c, d, e, n	N/A	a, b or c corresponds to a glide along $1/2$ of this lattice vector. d is a glide along $1/4$ of a face of the unit cell. e is two glides with the translation along two different $1/2$ lattice parameters. Finally n is a glide along $1/2$ of a unit cell face.

Table A.1: The crystallographic notation used throughout this thesis.

Symmetry notation in lattice dynamics

Phonons will break particular symmetries (the specifics depend on the nature of the mode) and the notation used in this thesis is that of the iuPAC. Here the notation L_{mn} where L is the symbol A or B which denotes if any rotational symmetry is lost

System	Lattice Parameters
Triclinic	$a \neq b \neq c$, $\alpha \neq \beta \neq \gamma \neq \pi/2$
Monoclinic	$a \neq b \neq c$, $\alpha = \beta = \pi/2 \neq \gamma$
Orthorhombic	$a \neq b \neq c$, $\alpha = \beta = \gamma = \pi/2$
Trigonal	$a = b = c$, $\alpha = \beta = \gamma \neq \pi/2$
Tetragonal	$a = b \neq c$, $\alpha = \beta = \gamma = \pi/2$
Hexagonal	$a = b \neq c$, $\alpha = \beta = \pi/2$, $\gamma = 2\pi/3$
Cubic	$a = b = c$, $\alpha = \beta = \gamma = \pi/2$

Table A.2: The seven crystal systems and their lattice parameters.

(A means it is not, B means it is), m is a number denoting similar combinations of operators and n will be either g or u for if the centre of symmetry is preserved or not. For example an A_{1g} mode preserves all symmetry while an A_{1u} mode preserves rotational but breaks inversion symmetry.

Author's relevant publications

[1] D. J. Voneshen, K. Refson, E. Borissenko, M. Krisch, A. Bosak, A. Piovano, E. Cemal, M. Enderle, M. J. Gutmann, M. Hoesch, et al., Nat Mater **12**, 1028 (2013), m3: Letter, URL http://dx.doi.org/10.1038/nmat3739.

[2] D. G. Porter, E. Cemal, D. J. Voneshen, K. Refson, M. J. Gutmann, A. Bombardi, A. T. Boothroyd, A. Krzton-Maziopa, E. Pomjakushina, K. Conder, et al., Phys.Rev.B **91**, 144114 (2015), URL http://link.aps.org/doi/10.1103/PhysRevB.91.144114.

Bibliography

[1] M. L. Foo, Y. Wang, S. Watauchi, H. W. Zandbergen, T. He, R. J. Cava, and N. P. Ong, Phys.Rev.Lett. **92**, 247001 (2004), URL http://link.aps.org/doi/10.1103/PhysRevLett.92.247001.

[2] D. Porter, *Control of electrons through patterning of superstructures in sodium cobaltate* (2012,).

[3] M. Pandiyan, *Phase diagram and control of thermoelectric properties of sodium cobaltate* (2014,).

[4] M. J. Ying LI, Guiying XU, Journal of Materials Sciences and Technology **22**, 526 (2006), URL http://www.jmst.org/EN/abstract/article_7902.shtml.

[5] Y. Hinuma, Y. S. Meng, and G. Ceder, Phys.Rev.B **77**, 224111 (2008), URL http://link.aps.org/doi/10.1103/PhysRevB.77.224111.

[6] R. Mittal, M. K. Gupta, S. L. Chaplot, M. Zbiri, S. Rols, H. Schober, Y. Su, T. Brueckel, and T. Wolf, Phys.Rev.B **87**, 184502 (2013), URL http://link.aps.org/doi/10.1103/PhysRevB.87.184502.

[7] World Bank, *Electric power transmission and distribution losses.*, http://data.worldbank.org/indicator/EG.ELC.LOSS.ZS, accessed: 4-4-2015.

[8] R. Hyde and P. Stevenson, The potential for recovering and using surplus heat from industry, Department of Energy and Climate Change, UK Gov. (2014).

[9] T. M. Tritt, Annual Review of Materials Research **41**, 433 (2011), http://dx.doi.org/10.1146/annurev-matsci-062910-100453, URL `http://dx.doi.org/10.1146/annurev-matsci-062910-100453`.

[10] H. J. Wu, L. D. Zhao, F. S. Zheng, D. Wu, Y. L. Pei, X. Tong, M. G. Kanatzidis, and J. Q. He, Nat Commun **5** (2014), URL `http://dx.doi.org/10.1038/ncomms5515`.

[11] G. J. Snyder and E. S. Toberer, Nat Mater **7**, 105 (2008), m3: 10.1038/nmat2090; 10.1038/nmat2090, URL `http://dx.doi.org/10.1038/nmat2090`.

[12] S. Stackhouse and L. Stixrude, Reviews in Mineralogy and Geochemistry **71**, 253 (2010).

[13] J. F. Annett, *Superconductivity, Superfluids and Condensates* (Oxford University Press, Oxford, 2010).

[14] J. Bardeen, L. N. Cooper, and J. R. Schrieffer, Phys.Rev. **106**, 162 (1957), URL `http://link.aps.org/doi/10.1103/PhysRev.106.162`.

[15] J. Nagamatsu, N. Nakagawa, T. Muranaka, Y. Zenitani, and J. Akimitsu, Nature **410**, 63 (2001), m3: 10.1038/35065039; 10.1038/35065039, URL `http://dx.doi.org/10.1038/35065039`.

[16] M. R. Norman, Science **332**, 196 (2011).

[17] G. R. Stewart, Rev.Mod.Phys. **56**, 755 (1984), URL `http://link.aps.org/doi/10.1103/RevModPhys.56.755`.

[18] M. K. Wu, J. R. Ashburn, C. J. Torng, P. H. Hor, R. L. Meng, L. Gao, Z. J. Huang, Y. Q. Wang, and C. W. Chu, Phys.Rev.Lett. **58**, 908 (1987), URL `http://link.aps.org/doi/10.1103/PhysRevLett.58.908`.

[19] M. Azzouz, Physica C: Superconductivity and its Applications **508**, 36 (2015).

[20] G. R. Stewart, Rev.Mod.Phys. **83**, 1589 (2011), URL `http://link.aps.org/doi/10.1103/RevModPhys.83.1589`.

[21] F. Wang and D.-H. Lee, Science **332**, 200 (2011), http://www.sciencemag.org/content/332/6026/200.full.pdf, URL `http://www.sciencemag.org/content/332/6026/200.abstract`.

[22] N. A. Garcia-Martinez, B. Valenzuela, S. Ciuchi, E. Cappelluti, M. J. Calderon, and E. Bascones, Phys.Rev.B **88**, 165106 (2013), URL `http://link.aps.org/doi/10.1103/PhysRevB.88.165106`.

[23] K. Takada, H. Sakurai, E. Takayama-Muromachi, F. Izumi, R. A. Dilanian, and T. Sasaki, Nature **422**, 53 (2003), m3: 10.1038/nature01450; 10.1038/nature01450, URL `http://dx.doi.org/10.1038/nature01450`.

[24] Y. J. Yan, M. Zhang, A. F. Wang, J. J. Ying, Z. Y. Li, W. Qin, X. G. Luo, J. Q. Li, J. Hu, and X. H. Chen, Sci.Rep. **2** (2012), m3: 10.1038/srep00212; 10.1038/srep00212, URL `http://dx.doi.org/10.1038/srep00212`.

[25] M. Roger, D. J. P. Morris, D. A. Tennant, M. J. Gutmann, J. P. Goff, J. U. Hoffmann, R. Feyerherm, E. Dudzik, D. Prabhakaran, A. T. Boothroyd, et al., Nature **445**, 631 (2007), m3: 10.1038/nature05531; 10.1038/nature05531, URL `http://dx.doi.org/10.1038/nature05531`.

[26] J. M. Tranquada, B. J. Sternlieb, J. D. Axe, Y. Nakamura, and S. Uchida,

Nature **375**, 561 (1995), m3: 10.1038/375561a0; 10.1038/375561a0, URL `http://dx.doi.org/10.1038/375561a0`.

[27] R. Pohl, A. Antognini, F. Nez, F. D. Amaro, F. Biraben, J. M. R. Cardoso, D. S. Covita, A. Dax, S. Dhawan, L. M. P. Fernandes, et al., Nature **466**, 213 (2010), m3: 10.1038/nature09250; 10.1038/nature09250, URL `http://dx.doi.org/10.1038/nature09250`.

[28] H. Arnold, M. I. Aroyo, E. F. Bertaut, Y. Billiet, B. M.J., H. Burzlaff, J. D. H. Donnay, W. Fischer, D. S. Fokkema, B. Gruber, et al., *International Tables for Crystallography, Volume A* (Springer, AA Dordrecht, The Netherlands, 2005), 5th ed.

[29] M. I. Aroyo, Y. Billiet, F. Gahler, V. Gramlich, A. Kirov, P. B. Konstantinov, E. B. Kroumova, U. Muller, G. Nebe, and H. Wondratschek, *International Tables for Crystallography, Vol A1, Symmetry Relations Between Space Groups* (Kluwer Academic Publishers, AA Dordrecht, The Netherlands, 2004).

[30] G. Sala, M. J. Gutmann, D. Prabhakaran, D. Pomaranski, C. Mitchelitis, J. B. Kycia, D. G. Porter, C. Castelnovo, and J. P. Goff, Nat Mater **13**, 488 (2014), m3: Article, URL `http://dx.doi.org/10.1038/nmat3924`.

[31] J. R. Stewart, K. H. Andersen, and R. Cywinski, Phys.Rev.B **78**, 014428 (2008).

[32] G. L. Squires, *Introduction to the theory of thermal neutron scattering* (Cambridge University Press, Cambridge, 1978).

[33] R. Hempelmann, *Quasielastic Neutron Scattering and Solid State Diffusion* (Oxford University Press, Oxford, 2000).

[34] J. Chadwick, Nature **192**, 312 (1932).

[35] A. Thompson, D. Attwood, E. Gullikson, M. Howells, K. J. Kim, J. Kirz, J. Kortright, I. Lindau, Y. Liu, P. Pianetta, et al., *X-Ray Data Booklet* (Lawrence Berkeley National Laboratory, Lawrence Berkeley National Laboratory, United States, 2009), 3rd ed.

[36] R. Resnick and R. Eisberg, *Quantum Physics of Atoms, Molecules, Solids, Nuclei and Particles* (John Wiley & Sons, USA, 1985), 2nd ed.

[37] C. J. C. B. Willis, *Experimental Neutron Scattering* (Oxford University Press, Great Britain, 2009).

[38] G. Caglioti, A. Paoletti, and F. P. Ricci, Nuclear Instruments **3**, 223 (1958).

[39] M. T. Dove, *Structure and Dynamics, An atomic view of materials.* (Oxford University Press, 2011).

[40] M. T. Dove, *Introduction to Lattice Dynamics* (Cambridge University Press, 2005).

[41] Nobel Media AB, *The nobel prize in physics 1994*, `http://www.nobelprize.org/nobel_prizes/physics/laureates/1994/shull-facts.html`, accessed: 3-3-2015.

[42] P. Willendrup, E. Farhi, and K. Lefmann, Physica B: Condensed Matter **350**, E735 (2004).

[43] R. I. Bewley, J. W. Taylor, and S. M. Bennington., Nuclear Instruments and Methods in Physics Research Section A: Accelerators, Spectrometers, Detectors and Associated Equipment **637**, 128 (2011).

[44] R. I. Bewley, R. S. Eccleston, K. A. McEwen, S. M. Hayden, M. T. Dove, S. M. Bennington, J. R. Treadgold, and R. L. S. Coleman, Physica B: Condensed Matter **385-386, Part 2**, 1029 (2006).

[45] L. van Eijck, L. Gerard, B. Frick, T. Seydel, and H. Schober, Nuclear Instruments and Methods in Physics Research Section A: Accelerators, Spectrometers, Detectors and Associated Equipment **672**, 64 (2012).

[46] ESRF, *High head-load premonochromator*, `http://www.esrf.eu/UsersAndScience/Experiments/DynExtrCond/ID28/BeamlineLayout/OH2/Premonochromator`, accessed: 4-3-2015.

[47] M. Krisch, F. Sette, M. Cardona, and R. Merlin, Topics in Applied Physics **108**, 317 (2007).

[48] S. M. Koohpayeh, D. Fort, and J. S. Abell, Progress in Crystal Growth and Characterization of Materials **54**, 121 (2008).

[49] Quantum Design, *Quantum design thermal transport option*, `http://www.qdusa.com/sitedocs/productBrochures/tto_rev7-06.pdf`, accessed: 3-3-2015.

[50] J. Kohanoff, *Electronic Structure Calculations for solids and Molecules* (Cambridge University Press, University Press, Cambridge, 2006).

[51] L. H. Thomas, Mathematical Proceedings of the Cambridge Philosophical Society **23**, 542 (1927), URL `http://journals.cambridge.org/article_S0305004100011683`.

[52] E. Fermi, Zeitschrift fr Physik **48**, 73 (1928), URL `http://dx.doi.org/10.1007/BF01351576`.

[53] P. Hohenberg and W. Kohn, Phys.Rev. **136**, B864 (1964), URL `http://link.aps.org/doi/10.1103/PhysRev.136.B864`.

[54] R. G. Parr and W. Yang, *Density-Functional Theory of Atoms and Molecules* (Oxford University Press, Oxford, 1994).

[55] W. Kohn and L. J. Sham, Phys.Rev. **140**, A1133 (1965), URL http://link.aps.org/doi/10.1103/PhysRev.140.A1133.

[56] J. P. Perdew and K. Schmidt, AIP Conference Proceedings **577**, 1 (2001), URL http://scitation.aip.org/content/aip/proceeding/aipcp/10.1063/1.1390175.

[57] D. M. Ceperley and B. J. Alder, Phys.Rev.Lett. **45**, 566 (1980), URL http://link.aps.org/doi/10.1103/PhysRevLett.45.566.

[58] R. O. Jones and O. Gunnarsson, Rev.Mod.Phys. **61**, 689 (1989), URL http://link.aps.org/doi/10.1103/RevModPhys.61.689.

[59] P. S. Svendsen and U. von Barth, Phys.Rev.B **54**, 17402 (1996), URL http://link.aps.org/doi/10.1103/PhysRevB.54.17402.

[60] A. E. Mattsson, P. A. Schultz, M. P. Desjarlais, T. R. Mattsson, and K. Leung, Modelling and Simulation in Materials Science and Engineering **13**, R1 (2005), URL http://stacks.iop.org/0965-0393/13/i=1/a=R01.

[61] J. P. Perdew, J. A. Chevary, S. H. Vosko, K. A. Jackson, M. R. Pederson, D. J. Singh, and C. Fiolhais, Phys.Rev.B **46**, 6671 (1992), URL http://link.aps.org/doi/10.1103/PhysRevB.46.6671.

[62] J. P. Perdew, K. Burke, and M. Ernzerhof, Phys.Rev.Lett. **77**, 3865 (1996), URL http://link.aps.org/doi/10.1103/PhysRevLett.77.3865.

[63] A. D. Becke, Phys.Rev.A **38**, 3098 (1988), URL http://link.aps.org/doi/10.1103/PhysRevA.38.3098.

[64] S. J. Clark, M. D. Segall, C. J. Pickard, P. J. Hasnip, M. I. J. Probert, K. Refson, and M. C. Payne, Zeitschrift fr Kristallographie **220**, 567 (2005; 2005),

doi: 10.1524/zkri.220.5.567.65075; M3: doi: 10.1524/zkri.220.5.567.65075, URL http://dx.doi.org/10.1524/zkri.220.5.567.65075.

[65] J. R. Hook and H. E. Hall, *Solid State Physics (Second Edition)* (Wiley, 2008), ISBN 978-0471-92805-8.

[66] H. J. Monkhorst and J. D. Pack, Phys.Rev.B **13**, 5188 (1976), URL http://link.aps.org/doi/10.1103/PhysRevB.13.5188.

[67] F. Giustino, *Materials Modelling using Density Functional Theory* (Oxford University Press, Oxford, 2014).

[68] J. C. Slater, Phys.Rev. **51**, 846 (1937), URL http://link.aps.org/doi/10.1103/PhysRev.51.846.

[69] J. C. Phillips and L. Kleinman, Phys.Rev. **116**, 287 (1959), URL http://link.aps.org/doi/10.1103/PhysRev.116.287.

[70] J. A. Appelbaum and D. R. Hamann, Phys.Rev.B **8**, 1777 (1973), URL http://link.aps.org/doi/10.1103/PhysRevB.8.1777.

[71] D. Vanderbilt, Phys.Rev.B **41**, 7892 (1990), URL http://link.aps.org/doi/10.1103/PhysRevB.41.7892.

[72] N. Marzari, D. Vanderbilt, and M. C. Payne, Phys.Rev.Lett. **79**, 1337 (1997), URL http://link.aps.org/doi/10.1103/PhysRevLett.79.1337.

[73] B. Himmetoglu, A. Floris, S. de Gironcoli, and M. Cococcioni, International Journal of Quantum Chemistry **114**, 14 (2014), URL http://dx.doi.org/10.1002/qua.24521.

[74] M. Cococcioni and S. de Gironcoli, Phys.Rev.B **71**, 035105 (2005), URL http://link.aps.org/doi/10.1103/PhysRevB.71.035105.

[75] H. Hellmann, Zeitschrift fr Physik **85**, 180 (1933), URL http://dx.doi.org/10.1007/BF01342053.

[76] R. P. Feynman, Phys.Rev. **56**, 340 (1939), URL http://link.aps.org/doi/10.1103/PhysRev.56.340.

[77] B. G. Pfrommer, M. Cote, S. G. Louie, and M. L. Cohen, J.Comput.Phys. **131**, 233 (1997).

[78] C. E. W. Frank and M. Fähnle, Phys. Rev. Lett. **74**, 1791 (1995).

[79] Z. Q. L. Krzysztof Parlinski and Y. Kawazoe, Phys. Rev. Lett. **78**, 4063 (1997).

[80] B. Poudel, Q. Hao, Y. Ma, Y. Lan, A. Minnich, B. Yu, X. Yan, D. Wang, A. Muto, D. Vashaee, et al., Science **320**, 634 (2008), http://www.sciencemag.org/content/320/5876/634.full.pdf, URL http://www.sciencemag.org/content/320/5876/634.abstract.

[81] E. D. Specht, J. Ma, O. Delaire, J. D. Budai, A. F. May, and E. A. Karapetrova, Journal of Electronic Materials pp. 1–4 (2014), URL http://dx.doi.org/10.1007/s11664-014-3447-0.

[82] MaJ., DelaireO., M. F., C. E., M. A., V. H., A. L., EhlersG., T. Hong, HuqA., et al., Nat Nano **8**, 445 (2013), m3: Article, URL http://dx.doi.org/10.1038/nnano.2013.95.

[83] O. Delaire, J. Ma, K. Marty, A. F. May, M. A. McGuire, M.-H. Du, D. J. Singh, A. Podlesnyak, G. Ehlers, M. D. Lumsden, et al., Nat Mater **10**, 614 (2011), m3: 10.1038/nmat3035; 10.1038/nmat3035, URL http://dx.doi.org/10.1038/nmat3035.

[84] G. A. Slack and V. G. Tsoukala, Journal of Applied Physics **76**, 1665 (1994), URL http://scitation.aip.org/content/aip/journal/jap/76/3/10.1063/1.357750.

[85] G. A. Slack, *CRC Handbook of Thermoelectrics* (CRC, 1995), pp. 407–440.

[86] E. S. Toberer, L. L. Baranowski, and C. Dames, Annual Review of Materials Research **42**, 179 (2012), http://dx.doi.org/10.1146/annurev-matsci-070511-155040, URL http://dx.doi.org/10.1146/annurev-matsci-070511-155040.

[87] G. S. Nolas, J. L. Cohn, and G. A. Slack, Phys.Rev.B **58**, 164 (1998), URL http://link.aps.org/doi/10.1103/PhysRevB.58.164.

[88] J. L. Cohn, G. S. Nolas, V. Fessatidis, T. H. Metcalf, and G. A. Slack, Phys.Rev.Lett. **82**, 779 (1999), URL http://link.aps.org/doi/10.1103/PhysRevLett.82.779.

[89] K. E. Goodson, Science **315**, 342 (2007), http://www.sciencemag.org/content/315/5810/342.full.pdf, URL http://www.sciencemag.org/content/315/5810/342.short.

[90] J. Dong, O. F. Sankey, and C. W. Myles, Phys.Rev.Lett. **86**, 2361 (2001), URL http://link.aps.org/doi/10.1103/PhysRevLett.86.2361.

[91] J. S. Tse, D. D. Klug, J. Y. Zhao, W. Sturhahn, E. E. Alp, J. Baumert, C. Gutt, M. R. Johnson, and W. Press, Nat Mater **4**, 917 (2005), m3: 10.1038/nmat1525; 10.1038/nmat1525, URL http://dx.doi.org/10.1038/nmat1525.

[92] G. J. Long, R. P. Hermann, F. Grandjean, E. E. Alp, W. Sturhahn, C. E.

Johnson, D. E. Brown, O. Leupold, and R. Ruffer, Phys.Rev.B **71**, 140302 (2005), URL http://link.aps.org/doi/10.1103/PhysRevB.71.140302.

[93] A. M. chel, I. Sergueev, N. Nguyen, G. J. Long, F. Grandjean, D. C. Johnson, and R. P. Hermann, Phys.Rev.B **84**, 064302 (2011), URL http://link.aps.org/doi/10.1103/PhysRevB.84.064302.

[94] J. L. Feldman, D. J. Singh, I. I. Mazin, D. Mandrus, and B. C. Sales, Phys.Rev.B **61**, R9209 (2000), URL http://link.aps.org/doi/10.1103/PhysRevB.61.R9209.

[95] C. H. Lee, I. Hase, H. Sugawara, H. Yoshizawa, and H. Sato, Journal of the Physical Society of Japan **75**, 123602 (2006), http://dx.doi.org/10.1143/JPSJ.75.123602, URL http://dx.doi.org/10.1143/JPSJ.75.123602.

[96] M. Christensen, A. B. Abrahamsen, N. B. Christensen, F. Juranyi, N. H. Andersen, K. Lefmann, J. Andreasson, C. R. H. Bahl, and B. B. Iversen, Nat Mater **7**, 811 (2008), m3: 10.1038/nmat2273; 10.1038/nmat2273, URL http://dx.doi.org/10.1038/nmat2273.

[97] C.-H. Lee, H. Yoshizawa, M. A. Avila, I. Hase, K. Kihou, and T. Takabatake, Journal of the Physical Society of Japan **77**, 260 (2008), http://dx.doi.org/10.1143/JPSJS.77SA.260, URL http://dx.doi.org/10.1143/JPSJS.77SA.260.

[98] M. Zebarjadi, J. Yang, K. Lukas, B. Kozinsky, B. Yu, M. S. Dresselhaus, C. Opeil, Z. Ren, and G. Chen, Journal of Applied Physics **112**, (2012), URL http://scitation.aip.org/content/aip/journal/jap/112/4/10.1063/1.4747911.

[99] I. Terasaki, Y. Sasago, and K. Uchinokura, Phys.Rev.B **56**, R12685 (1997), URL http://link.aps.org/doi/10.1103/PhysRevB.56.R12685.

[100] Z. Li, J. Yang, J. G. Hou, and Q. Zhu, Phys.Rev.B **70**, 144518 (2004), URL http://link.aps.org/doi/10.1103/PhysRevB.70.144518.

[101] Y. Wang, N. S. Rogado, R. J. Cava, and N. P. Ong, Nature **423**, 425 (2003), m3: 10.1038/nature01639; 10.1038/nature01639, URL http://dx.doi.org/10.1038/nature01639.

[102] H. J. Xiang and D. J. Singh, Phys.Rev.B **76**, 195111 (2007), URL http://link.aps.org/doi/10.1103/PhysRevB.76.195111.

[103] L. Viciu, J. W. G. Bos, H. W. Zandbergen, Q. Huang, M. L. Foo, S. Ishiwata, A. P. Ramirez, M. Lee, N. P. Ong, and R. J. Cava, Phys.Rev.B **73**, 174104 (2006), URL http://link.aps.org/doi/10.1103/PhysRevB.73.174104.

[104] Q. H. *et al.*, Journal of Physics: Condensed Matter **16**, 5803 (2004), URL http://stacks.iop.org/0953-8984/16/i=32/a=016.

[105] D. J. P. Morris, M. Roger, M. J. Gutmann, J. P. Goff, D. A. Tennant, D. Prabhakaran, A. T. Boothroyd, E. Dudzik, R. Feyerherm, J. U. Hoffmann, et al., Phys.Rev.B **79**, 100103 (2009).

[106] H. Alloul, I. R. Mukhamedshin, T. A. Platova, and A. V. Dooglav, EPL (Europhysics Letters) **85**, 47006 (2009), URL http://stacks.iop.org/0295-5075/85/i=4/a=47006.

[107] R. Berthelot, D. Carlier, and C. Delmas, Nat Mater **10**, 74 (2011), m3: 10.1038/nmat2920; 10.1038/nmat2920, URL http://dx.doi.org/10.1038/nmat2920.

[108] F. C. Chou, M. W. Chu, G. J. Shu, F. T. Huang, W. W. Pai, H. S. Sheu, and P. A. Lee, Phys.Rev.Lett. **101**, 127404 (2008), URL `http://link.aps.org/doi/10.1103/PhysRevLett.101.127404`.

[109] Y. G. Shi, Y. L. Liu, H. X. Yang, C. J. Nie, R. Jin, and J. Q. Li, Phys.Rev.B **70**, 052502 (2004), URL `http://link.aps.org/doi/10.1103/PhysRevB.70.052502`.

[110] M. N. Iliev, A. P. Litvinchuk, R. L. Meng, Y. Y. Sun, J. Cmaidalka, and C. W. Chu, Physica C: Superconductivity **402**, 239 (2004).

[111] P. Lemmens, P. Scheib, Y. Krockenberger, L. Alff, F. C. Chou, C. T. Lin, H. U. Habermeier, and B. Keimer, Phys.Rev.B **75**, 106501 (2007), URL `http://link.aps.org/doi/10.1103/PhysRevB.75.106501`.

[112] J. W. Lynn, Q. Huang, C. M. Brown, V. L. Miller, M. L. Foo, R. E. Schaak, C. Y. Jones, E. A. Mackey, and R. J. Cava, Phys.Rev.B **68**, 214516 (2003), URL `http://link.aps.org/doi/10.1103/PhysRevB.68.214516`.

[113] P. K. Jha, A. Troper, I. C. da Cunha Lima, M. Talati, and S. P. Sanyal, Physica B: Condensed Matter **366**, 153 (2005).

[114] P. Lemmens, V. Gnezdilov, N. N. Kovaleva, K. Y. Choi, H. Sakurai, E. Takayama-Muromachi, K. Takada, T. Sasaki, F. C. Chou, D. P. Chen, et al., Journal of Physics: Condensed Matter **16**, S857 (2004), URL `http://stacks.iop.org/0953-8984/16/i=11/a=041`.

[115] A. T. Boothroyd, R. Coldea, D. A. Tennant, D. Prabhakaran, L. M. Helme, and C. D. Frost, Phys.Rev.Lett. **92**, 197201 (2004), URL `http://link.aps.org/doi/10.1103/PhysRevLett.92.197201`.

[116] J. P. Rueff, M. Calandra, M. d'Astuto, P. Leininger, A. Shukla, A. Bosak, M. Krisch, H. Ishii, Y. Cai, P. Badica, et al., Phys.Rev.B **74**, 020504 (2006), URL http://link.aps.org/doi/10.1103/PhysRevB.74.020504.

[117] *Pyminuit*, https://github.com/jpivarski/pyminuit, accessed: 28-2-2015.

[118] G. Cowan, *Statistical Data Analysis* (Oxford University Press, 1998), ISBN 0 19 850155 2.

[119] M. H. Julien, C. de Vaulx, H. Mayaffre, C. Berthier, H. M., V. Simonet, J. Wooldridge, G. Balakrishnan, M. R. Lees, D. P. Chen, et al., Phys.Rev.Lett. **100**, 096405 (2008), URL http://link.aps.org/doi/10.1103/PhysRevLett.100.096405.

[120] Y. Krockenberger, I. Fritsch, G. Christiani, H. U. Habermeier, L. Yu, C. Bernhard, B. Keimer, and L. Alff, Applied Physics Letters **88**, (2006), URL http://scitation.aip.org/content/aip/journal/apl/88/16/10.1063/1.2196061.

[121] M. M. Koza, M. R. Johnson, R. Viennois, H. Mutka, L. Girard, and D. Ravot, Nat Mater **7**, 805 (2008), m3: 10.1038/nmat2260; 10.1038/nmat2260, URL http://dx.doi.org/10.1038/nmat2260.

[122] B. Huang and M. Kaviany, Acta Materialia **58**, 4516 (2010).

[123] X. Zhou, G. Wang, L. Zhang, H. Chi, X. Su, J. Sakamoto, and C. Uher, J.Mater.Chem. **22**, 2958 (2012), URL http://dx.doi.org/10.1039/C2JM15010G.

[124] M. Lee, L. Viciu, L. Li, Y. Wang, M. L. Foo, S. Watauchi, R. A. P. Jr, R. J. Cava, and N. P. Ong, Nat Mater **5**, 537 (2006), m3: 10.1038/nmat1669; 10.1038/nmat1669, URL http://dx.doi.org/10.1038/nmat1669.

[125] D. G. Porter, M. Roger, M. J. Gutmann, S. Uthayakumar, D. Prabhakaran, A. T. Boothroyd, M. S. Pandiyan, and J. P. Goff, Phys.Rev.B **90**, 054101 (2014), URL `http://link.aps.org/doi/10.1103/PhysRevB.90.054101`.

[126] T. Kawata, Y. Iguchi, T. Itoh, K. Takahata, and I. Terasaki, Phys.Rev.B **60**, 10584 (1999), URL `http://link.aps.org/doi/10.1103/PhysRevB.60.10584`.

[127] T. Nagira, M. Ito, S. Katsuyama, K. Majima, and H. Nagai, Journal of Alloys and Compounds **348**, 263 (2003).

[128] K. Takahata, Y. Iguchi, D. Tanaka, T. Itoh, and I. Terasaki, Phys.Rev.B **61**, 12551 (2000), URL `http://link.aps.org/doi/10.1103/PhysRevB.61.12551`.

[129] S. C. Han, H. Lim, J. Jeong, D. Ahn, W. B. Park, K.-S. Sohn, and M. Pyo, Journal of Power Sources **277**, 9 (2015).

[130] B. G. Pfrommer, M. Cote, S. G. Louie, and M. L. Cohen, J. Comput. Phys. **131**, 233 (1997).

[131] R. H. Byrd, J. Nocedal, and R. B. Schnabel, Math. Prog. **63**, 129 (1994).

[132] Y. Kamihara, T. Watanabe, M. Hirano, and H. Hosono, Journal of the American Chemical Society **130**, 3296 (2008), pMID: 18293989; http://dx.doi.org/10.1021/ja800073m, URL `http://dx.doi.org/10.1021/ja800073m`.

[133] J. Guo, S. Jin, G. Wang, S. Wang, K. Zhu, T. Zhou, M. He, and X. Chen, Phys.Rev.B **82**, 180520 (2010), URL `http://link.aps.org/doi/10.1103/PhysRevB.82.180520`.

[134] Y. Mizuguchi, H. Takeya, Y. Kawasaki, T. Ozaki, S. Tsuda, T. Yamaguchi, and Y. Takano, Applied Physics Letters **98**, (2011), URL http://scitation.aip.org/content/aip/journal/apl/98/4/10.1063/1.3549702.

[135] A. Krzton-Maziopa, Z. Shermadini, E. Pomjakushina, V. Pomjakushin, M. Bendele, A. Amato, R. Khasanov, H. Luetkens, and K. Conder, Journal of Physics: Condensed Matter **23**, 052203 (2011), URL http://stacks.iop.org/0953-8984/23/i=5/a=052203.

[136] A. F. Wang, J. J. Ying, Y. J. Yan, R. H. Liu, X. G. Luo, Z. Y. Li, X. F. Wang, M. Zhang, G. J. Ye, P. Cheng, et al., Phys.Rev.B **83**, 060512 (2011), URL http://link.aps.org/doi/10.1103/PhysRevB.83.060512.

[137] B. Wei**, H. Qing-Zhen, C. Gen-Fu, M. A. Green, W. Du-Ming, H. Jun-Bao, and Q. Yi-Ming, Chinese Physics Letters **28**, 86104 (2011), URL http://cpl.iphy.ac.cn/EN/abstract/article_44566.shtml.

[138] W. Li, H. Ding, Z. Li, P. Deng, K. Chang, K. He, S. Ji, L. Wang, X. Ma, J.-P. Hu, et al., Phys.Rev.Lett. **109**, 057003 (2012), URL http://link.aps.org/doi/10.1103/PhysRevLett.109.057003.

[139] S. D. Wilson, Z. Yamani, C. R. Rotundu, B. Freelon, E. Bourret-Courchesne, and R. J. Birgeneau, Phys.Rev.B **79**, 184519 (2009), URL http://link.aps.org/doi/10.1103/PhysRevB.79.184519.

[140] P. Zavalij, W. Bao, X. F. Wang, J. J. Ying, X. H. Chen, D. M. Wang, J. B. He, X. Q. Wang, G. F. Chen, P. Y. Hsieh, et al., Phys.Rev.B **83**, 132509 (2011), URL http://link.aps.org/doi/10.1103/PhysRevB.83.132509.

[141] M. Wang, M. Wang, G. N. Li, Q. Huang, C. H. Li, G. T. Tan, C. L. Zhang, H. Cao, W. Tian, Y. Zhao, et al., Phys.Rev.B **84**, 094504 (2011), URL http://link.aps.org/doi/10.1103/PhysRevB.84.094504.

[142] L. Hggstrm, H. R. Verma, S. Bjarman, R. Wppling, and R. Berger, Journal of Solid State Chemistry **63**, 401 (1986).

[143] J. Zhao, H. Cao, E. Bourret-Courchesne, D. H. Lee, and R. J. Birgeneau, Phys.Rev.Lett. **109**, 267003 (2012), URL http://link.aps.org/doi/10.1103/PhysRevLett.109.267003.

[144] Z. Wang, Y. J. Song, H. L. Shi, Z. W. Wang, Z. Chen, H. F. Tian, G. F. Chen, J. G. Guo, H. X. Yang, and J. Q. Li, Phys.Rev.B **83**, 140505 (2011), URL http://link.aps.org/doi/10.1103/PhysRevB.83.140505.

[145] A. Bosak, V. Svitlyk, A. Krzton-Maziopa, E. Pomjakushina, K. Conder, V. Pomjakushin, A. Popov, D. de Sanctis, and D. Chernyshov, Phys.Rev.B **86**, 174107 (2012), URL http://link.aps.org/doi/10.1103/PhysRevB.86.174107.

[146] A. Ricci, N. Poccia, G. Campi, B. Joseph, G. Arrighetti, L. Barba, M. Reynolds, M. Burghammer, H. Takeya, Y. Mizuguchi, et al., Phys.Rev.B **84**, 060511 (2011), URL http://link.aps.org/doi/10.1103/PhysRevB.84.060511.

[147] W. Li, S. Dong, C. Fang, and J. Hu, Phys.Rev.B **85**, 100407 (2012), URL http://link.aps.org/doi/10.1103/PhysRevB.85.100407.

[148] J. T. Park, G. Friemel, Y. Li, J. H. Kim, V. Tsurkan, J. Deisenhofer, H. A. K. von Nidda, A. Loidl, A. Ivanov, B. Keimer, et al., Phys.Rev.Lett. **107**, 177005 (2011), URL http://link.aps.org/doi/10.1103/PhysRevLett.107.177005.

[149] M. Wang, C. Fang, D.-X. Yao, G. Tan, L. W. Harriger, Y. Song, T. Netherton, C. Zhang, M. Wang, M. B. Stone, et al., Nat Commun **2**, 580 (2011), m3:

10.1038/ncomms1573; 10.1038/ncomms1573, URL http://dx.doi.org/10.1038/ncomms1573.

[150] A. E. Taylor, R. A. Ewings, T. G. Perring, J. S. White, P. Babkevich, A. Krzton-Maziopa, E. Pomjakushina, K. Conder, and A. T. Boothroyd, Phys.Rev.B **86**, 094528 (2012), URL http://link.aps.org/doi/10.1103/PhysRevB.86.094528.

[151] L. N., H. Lei, C. Petrovic, and P. Z. V., Phys.Rev.B **84**, 214305 (2011), URL http://link.aps.org/doi/10.1103/PhysRevB.84.214305.

[152] A. M. Zhang, K. Liu, J. B. He, D. M. Wang, G. F. Chen, B. Normand, and Q. M. Zhang, Phys.Rev.B **86**, 134502 (2012), URL http://link.aps.org/doi/10.1103/PhysRevB.86.134502.

[153] A. M. Zhang, K. Liu, J. H. Xiao, J. B. He, D. M. Wang, G. F. Chen, B. Normand, and Q. M. Zhang, Phys.Rev.B **85**, 024518 (2012), URL http://link.aps.org/doi/10.1103/PhysRevB.85.024518.

[154] Z. G. Chen, R. H. Yuan, T. Dong, G. Xu, Y. G. Shi, P. Zheng, J. L. Luo, J. G. Guo, X. L. Chen, and N. L. Wang, Phys.Rev.B **83**, 220507 (2011), URL http://link.aps.org/doi/10.1103/PhysRevB.83.220507.

[155] C. C. Homes, Z. J. Xu, J. S. Wen, and G. D. Gu, Phys.Rev.B **85**, 180510 (2012), URL http://link.aps.org/doi/10.1103/PhysRevB.85.180510.

[156] R. H. Yuan, T. Dong, Y. J. Song, P. Zheng, G. F. Chen, J. P. Hu, J. Q. Li, and N. L. Wang, Sci.Rep. **2** (2012), m3: 10.1038/srep00221; 10.1038/srep00221, URL http://dx.doi.org/10.1038/srep00221.

[157] A. Ignatov, A. Kumar, P. Lubik, R. H. Yuan, W. T. Guo, N. L. Wang, K. Rabe,

and G. Blumberg, Phys.Rev.B **86**, 134107 (2012), URL http://link.aps.org/doi/10.1103/PhysRevB.86.134107.

[158] P. Gao, R. Yu, L. Sun, H. Wang, Z. Wang, Q. Wu, M. Fang, G. Chen, J. Guo, C. Zhang, et al., Phys.Rev.B **89**, 094514 (2014), URL http://link.aps.org/doi/10.1103/PhysRevB.89.094514.

[159] X.-W. Yan, M. Gao, Z.-Y. Lu, and T. Xiang, Phys.Rev.B **83**, 233205 (2011), URL http://link.aps.org/doi/10.1103/PhysRevB.83.233205.

[160] W. Li, H. Ding, P. Deng, K. Chang, C. Song, K. He, L. Wang, X. Ma, J.-P. Hu, X. Chen, et al., Nat Phys **8**, 126 (2012), m3: 10.1038/nphys2155; 10.1038/nphys2155, URL http://dx.doi.org/10.1038/nphys2155.

[161] A. F. May, M. A. McGuire, H. Cao, I. Sergueev, C. Cantoni, B. C. Chakoumakos, D. S. Parker, and B. C. Sales, Phys.Rev.Lett. **109**, 077003 (2012), URL http://link.aps.org/doi/10.1103/PhysRevLett.109.077003.

[162] C. H. Ahn, J. M. Triscone, and J. Mannhart, Nature **424**, 1015 (2003), m3: 10.1038/nature01878; 10.1038/nature01878, URL http://dx.doi.org/10.1038/nature01878.

[163] J.-F. Ge, Z.-L. Liu, C. Liu, C.-L. Gao, D. Qian, Q.-K. Xue, Y. Liu, and J.-F. Jia, Nat Mater **14**, 285 (2015), m3: Letter, URL http://dx.doi.org/10.1038/nmat4153.

[164] H. Liu, X. Shi, F. Xu, L. Zhang, W. Zhang, L. Chen, Q. Li, C. Uher, T. Day, and G. J. Snyder, Nat Mater **11**, 422 (2012), m3: 10.1038/nmat3273; 10.1038/nmat3273, URL http://dx.doi.org/10.1038/nmat3273.

[165] M. L. Tacon, A. Bosak, S. M. Souliou, G. Dellea, T. Loew, R. Heid, K.-P.

Bohnen, G. Ghiringhelli, M. Krisch, and B. Keimer, Nat Phys **10**, 52 (2014), m3: Article, URL `http://dx.doi.org/10.1038/nphys2805`.

[166] E. W. Weisstein, *"reflection." from mathworld–a wolfram web resource*, `http://mathworld.wolfram.com/Reflection.html`, accessed: 1-7-2015.

[167] E. W. Weisstein, *"rotation formula." from mathworld–a wolfram web resource*, `http://mathworld.wolfram.com/RotationFormula.html`, accessed: 1-7-2015.